Advances in Microscopic, Time-Correlated Neutron Noise Techniques

by

Michael Yeungjun Hua

A dissertation submitted in partial fulfillment
of the requirements for the degree of
Doctor of Philosophy
(Nuclear Engineering and Radiological Sciences)
in The University of Michigan
2021

Doctoral Committee:

Professor Sara A. Pozzi, Chair
Doctor Shaun Clarke
Mr. Jesson Hutchinson, Los Alamos National Laboratory
Associate Professor Brian Kiedrowski
Professor Michael Liemohn
Doctor George McKenzie, Los Alamos National Laboratory

Michael Y. Hua
mikwa@umich.edu
ORCID ID: 0000-0003-2581-3537

And Forever Go Blue

ACKNOWLEDGEMENTS

I would like to acknowledge the following funding organizations for supporting my research. I was predominantly supported by my National Science Foundation Graduate Research Fellowship under Grant No. DGE-1256260. Measurement activities were supported by the Consortium for Verification Technology under Department of Energy National Nuclear Security Administration award number DE-NA0002534, and the Department of Energy Nuclear Criticality Safety Program, funded and managed by the National Nuclear Security Administration. The measurements were performed at the National Criticality Experiments Research Center within the Device Assembly Facility at the Nevada National Security Site, and I am thankful for the individuals that aided in the execution of and access to experiments. Additional analysis efforts were supported by the Consortium for Monitoring, Technology, and Verification under Department of Energy National Nuclear Security Administration award number DE-NA0003920. Any opinion, finding, conclusion, or recommendations expressed in this material are those of myself and coauthors, and do not necessarily reflect the views of any funding organization.

I would like to acknowledge the following individuals. First, I thank my advisor and committee chair Professor Sara Pozzi for taking me as a student in the summer of 2016 and Professor Angela Di Fulvio and Dr. Tony Shin for favorably considering my application and interview. I also want to thank Prof. Pozzi for giving me the opportunity to learn about and help write grant proposals, affording me a great deal of independence, and supporting measurements at NCERC. The most important lesson I learned from Prof. Pozzi and Dr. Shaun Clarke is that any problems/issues/discrepancies should not be looked at negatively,

rather as an opportunity to exploit a physical phenomenon as a signature: *it's a feature*. I thank both Prof. Pozzi and Shaun for giving the opportunity to teach and mentor students in addition to my own research responsibilities. I also thank Shaun for often being one of the first authors to read and comment drafts – certain grammar rules echo in my mind in Shaun's voice.

My most formative mentor for the foundations of radiation detection and measurements and associated research is Tony. Tony was my official mentor from 2016-2018, taught me to connect technical material to the motivation/application space, and held both of us to the high standard I still hold myself to today. Tony helped me secure the internship with Los Alamos National Laboratory that defined the direction of my dissertation work.

Mr. Jesson Hutchinson is my primary mentor from Los Alamos National Laboratory, proposed many of the problems solved by this dissertation, and has been ridiculously available for my many questions and requests; I sent a first draft of this dissertation to him at 3:56 PM on a Friday and he had comments back to me at 4:04 PM the next day. Jesson has been a champion for me since day one, kind, welcoming, and I have overwhelming gratitude for the patience and energy he has shown throughout. He and Dr. Geordie McKenzie helped me gain access to many measurements at NCERC, which have been essential to the validation work in this thesis. Both expanded my interests from nonproliferation and safeguards to include criticality safety, contextualized theory in practical measurements, and helped me plan (and game plan) experiments.

Professor Brian Kiedrowski is one of the best instructors I have had the opportunity to take a course from and teach one with. Brian was extremely helpful with the simulation work of this dissertation. More importantly and iconically, Brian would be roaming the halls of Cooley and eventually my office where I'd hear a "Mr. Hua..." on a weekday evening. We would proceed to talk, discuss technical material, and dissect hypotheticals far too late.

I thank Travis Grove for DC-ing most of my content, including this thesis.

I thank the Detection for Nuclear Nonproliferation Group students that I overlapped

with as well as John Rodriquez. I thank Caiser Bravo, Flynn Darby, Abbas Jinia, Elinor Mullin, Nathan Giha, Christopher Meert, Noah Kleedtke, Leah Clark, and Juliann Lamproe for reading and commenting on early iterations of this dissertation. I thank the students I had the opportunity to mentor: Juliann, Noah, Leah, Flynn, Philip Bauwens, Tessa Maurer, Caiser, Joseph Lorenzetti, Prashant Shankar, Rowan Marchie, Emma Cho, Subhasri Pothuraju, Ricardo Lopez, Thomas Plummer, John-Tyler Iacovetta, Aaron MacDonald, and Aunic Goodin. Stefano Marin (we've never met – this is a random volunteer from the crowd) helped make the group so much more fun, which I value greatly... K♡.

I thank fun friends – Aye Cho Mem! Also the undergraduate NERS class of 2018 + Kyle Beyer + Nathan Giha for being awesome. Nathan, Kyle, Devin Mussel, Lauren Green, and Flynn have be particularly awesome after graduation between Los Alamos, flag football, and other nontechnical activities (beer) with nuclear engineers.

I thank the Redoutey family (including the extended Guzzardo and Redoutey families) for welcoming me and becoming part of what I consider my family.

I thank Aunt Sharon for her love, support, and for stressing the importance and value of being able to communicate technical material to nontechnical audiences since I was in middle school.

I am thankful to my siblings, Megan and Matthew. We share a strong bond that grows as we each become more of our own individuals. I also thank my friends; there are too many to construct a comprehensive list, but I do want to specifically thank David, Lauren and Sanskar. They have made life outside the NERS department fun and now I own too many board games.

I thank my parents and grandparents for their love, support, and sacrifice. The fiscal support enabled me to focus on opportunity and academics, whereas I would have had to otherwise share energy and time with a job. More importantly, I am appreciative of the sacrifice that I have been able to better recognize once distanced and as I have matured. My grandparents prioritized the success of their children and me, and my parents prioritized

my success. Both sides immigrated to the US, all took me on trips, supported summer enrichment camps, and have best supported me by showing me that my success makes them happy. I often think about Ahmah and Ye-Ye having to sell Ahmah's engagement ring to support their family, both traveling to a foreign land with their children, becoming US citizens, finding work and creating their own business, and them and my Dad having to learn English. I often think about Grandma fighting through health adversities with the steadfast attitude of success, her stories of physics class, the passion and pride she has in her ideas, Grandpa earning three engineering degrees, him serving his country, both of them working hard and smart to save for the life they get to live now, and the uncompromising partnership to one another. My parents taught me too many values to list, have been adaptable, taught me math and writing when I was young, value versatility, and are objective-oriented with efficiency. The greatest honor of earning my Ph.D. is the pride that my grandparents and parents have for me.

I thank my kitten Goose "The Pork Chop" Redoutey-Hua for being a huge source of joy as I finish my degree. She has also recommended edits to my papers and thesis by directly typing them into my document, been a harsher critic than reviewer two by deleting files, and should probably be a coauthor since there is surely a word in here that she has typed that I have not yet found.

I thank Maria Redoutey. I have tried to write this acknowledgments section several times, but don't know how to write this final paragraph... the dissertation review office informed me that it was in poor form for me to write an acknowledgments section longer than the numbered pages themselves... and so went the last draft. I have always worked hard for an abstract future and being with Maria helped me decide that the future is now, therein helping me develop work-life balance and changing the figure of merit that drives my life from abstract "success" to happiness... and I am happy. Maria has helped learn more than I have from my Ph.D. studies and grow into an individual that I like. She is a great partner and I cannot imagine completing the Ph.D. the way I did without her. Maria's love and constancy

is grounding and therein the pressures I experience (and there were many in the course of this Ph.D.) dissipate since they represent only small perturbations to the ever-growing amount of happiness I have from living my life with her. Maria, you are my best friend, my accomplice, my equilibrium, and my partner. Whereas without you I would suppress every emotion as a distraction, I am overwhelmed with gratitude, with appreciation, with happiness, and with love. Thank you.

TABLE OF CONTENTS

LIST OF FIGURES

Figure

LIST OF TABLES

Table

LIST OF APPENDICES

Appendix

ABSTRACT

Estimating k_{eff}, a parameter that characterizes neutron-multiplying assemblies, is of broad interest and paramount importance in the nuclear community including in applications like nuclear criticality safety, nonproliferation and safeguards, and stockpile stewardship. A k_{eff} equal to one represents a self-sustaining and stable chain reaction, and is often desirable in energy-producing reactors. An uncontrolled/accidental k_{eff} greater than one can result in criticality accidents, operator death, and catastrophic damage. Therefore, it is desirable to be able to control and monitor the k_{eff} of an assembly; the value of k_{eff} can be modulated and tailored by using reflector material. A challenge is that k_{eff} cannot be directly measured; however, it can be inferred from the prompt neutron decay constant, α, and its negative reciprocal, the prompt neutron period. Microscopic, time-correlated, neutron noise techniques are used to measure α and the two most popular methods are the Rossi-alpha and Feynman-alpha approaches. This dissertation advances the two methods by addressing shortcomings in detectors, models, and uncertainty quantification.

In general, current measurements are performed with state-of-the-art ^{3}He detectors that are insensitive to fast assemblies (with prompt periods shorter than a microsecond). Fast assemblies are pertinent to criticality safety applications and modern fast reactor designs, for example. The measurements of this dissertation use and validate the new organic scintillator array (OSCAR) system, which measured up to 15 kg of weapons-grade plutonium, 22 kg of highly enriched uranium, and 6 kg of neptunium ($0.45 < k_{\text{eff}} < 0.95$). The data analysis demonstrates that OSCAR exhibits capabilities beyond ^{3}He systems. For instance, OSCAR is sensitive to prompt neutron periods as fast as 8 ns, whereas ^{3}He detectors are limited to $\approx$1 μs. Furthermore, the OSCAR exhibits much less noise and can achieve desired precisions

faster than competing ^{3}He systems by factors as great as 10^2.

The Rossi- and Feynman-alpha techniques were originally developed for bare cores of fissionable material and the traditional one-region point kinetics model (a one-exponential probability density function) is inadequate for reflected assemblies that requires a two-region model. Since reflectors are of interest in the application space, new theory is required. New theory is also required for uncertainty propagation and quantification from a single measurement; currently, methods are either incorrect or rely on long, repeated measurements. This dissertation extends traditional point kinetics from one-region to two-region and rigorously derives uncertainty methods for both the Rossi- and Feynman-alpha methods. The new theory is validated with the OSCAR and ^{3}He measurements of reflected assemblies. The results demonstrate that the new theory increases the accuracy of α estimates by over 10% for highly-reflected cases and generalizes the existing models: the two-region approach will reduce to the one-region model when greater generality is not needed. The two-region model introduces new variables and it is shown that the parameters can potentially be exploited as signatures of reflection. The two neutron noise techniques are compared and it is found that the Feynman-alpha method is more precise than the Rossi-alpha method by one-to-two orders of magnitude in relative uncertainty. In terms of accuracy, the Feynman-alpha approach outperforms the Rossi-alpha approach for $k_{\text{eff}} < 0.92$, whereas the opposite is true for $k_{\text{eff}} > 0.92$. The uncertainty methods based on a single measurement are validated and can reduce measurement times by a factor of 20 or more, therein reducing procedural and operational costs associated with measurements.

Taken together, this dissertation advances microscopic, time-correlated neutron noise techniques by introducing and demonstrating the use of a fast organic scintillator detection system that has capabilities beyond the current state-of-the-art ^{3}He systems, developing and validating new measurement theory to account for experiments on reflected assemblies, and developing and validating rigorous quantification of measurement uncertainty.

CHAPTER I

Introduction

1.1 Motivation for Neutron Noise Measurements of the Prompt Neutron Period

1.1.1 History, High-Level Motivation, Broad Challenge Statement

The study and application of nuclear fission and subsequent self-sustaining fission chains that multiply neutron populations is simultaneously young and significant, defining modern state postures and supplying approximately 20% of the civilian energy in the United States [7, 8, 9]. James Chadwick discovered the neutron in 1932 [10] and Enrico Fermi performed the first fission experiment with uranium shortly thereafter by using neutrons to induce the fission [11]. At the time, Fermi thought that they had created a larger radioactive nucleus – a so-called element 93. Ida Noddack would refute Fermi's interpretation in late 1934, suggesting that the possibility of the uranium splitting into smaller fragments was not considered [12]. The refute lacked theoretical foundation and thus there was no follow-up to the work until Hahn and Stassman found the first fission products in 1938 [13, 14], which would enable Lise Meitner to explain our modern understanding of fission based on the theory of the nucleus [15]. Otto Frisch is named as Meitner's second author in the discovery of fission and the first group leader of the critical experiments group at Los Alamos National Laboratory – the group I belong to – during the Manhattan Project.

After the discovery of fission, it was predicted that assemblies of fissionable material could sustain energy-producing fission chains: a neutron could induce fission in a fissionable nucleus, the fission would produce multiplets of neutrons, and these neutrons could continue to cause further fissions and propagate the chain reaction. Enrico Fermi demonstrated the first of such self-sustaining chain reactions with the Chicago Pile, a uranium-graphite pile in a squash court underneath Stagg Stadium in 1942 [16]. Engineering efforts then commercialized the physical phenomenon, producing and using the first nuclear weapons in 1945 and producing the first electricity from nuclear energy in 1951. The discoveries and engineering were not without criticality accidents (uncontrolled, rapidly growing fission chains) [17], with the most famous being Louis Slotin's experiment with the Demon Core that ended in Slotin's 1946 death. The General Assembly of the United Nations met for the first time in January of 1946; the first topic was nuclear disarmament and the second was the official language for meetings, therein highlighting the international recognition of the impact of nuclear fission chains. The main focus of the first resolution adopted by the General Assembly was the proliferation of peaceful fission chain applications and the nonproliferation of nuclear weapons (that are predicated on the uncontrollable energy release in rapidly growing fission chains). Later, the United Nations would adopt resolutions that prohibited various nuclear weapons activities including the Comprehensive Nuclear-Test-Ban Treaty. **Taken together, major challenges in modern nuclear engineering include monitoring the stockpile without detonation-based testing, nondestructive detection for nonproliferation and safeguards, monitoring of electricity-producing nuclear reactors, and ensuring the safety of fission chain operations (criticality safety).**

1.1.2 Microscopic, Time-Correlated Neutron Noise Measurements

The application space, a subset of nondestructive assay, of the challenge is restrictive in that (1) fissile assemblies must be measured with minimal external influence (e.g., scraping off a sample is insufficient, disallowed, and changes assembly behavior) and (2) unique

properties of the assemblies must be utilized (e.g., weighing a sample to estimate mass is insufficient since fissile material may be replaced and spoofed with other materials). **Time-correlated neutrons** are often used as a unique feature for characterization for a variety of reasons, including their scarcity in the background radiation profile. **Microscopic** measurements are based on the statistical fluctuations of the neutron population in time and are differentiated from macroscopic measurements, which are based on aggregate behavior (e.g., temperature) [18, 19]. Experiments and measurements are typically performed to characterize the propensity for a fissile assembly to sustain fission chains, which is summarized by a parameter called the effective multiplication factor, k_{eff}. Non-multiplying neutron sources such as PuBe, and AmLi emit neutrons randomly in time. Fission chains introduce fluctuations and modulate the time-distribution of neutron detections relative to the start of the chain (i.e., fission chains introduce **noise**). Therefore, microscopic, time-correlated neutron noise measurements (henceforth called neutron noise techniques) are used to characterize multiplying fission chain assemblies and represent one solution to the challenge presented in the preceding subsection. An additional challenge is that k_{eff} cannot be directly measured; however, it can be inferred from the prompt neutron decay constant, α, or its negative reciprocal the prompt neutron period. Thus, the Rossi-alpha method based on a suggestion from Bruno Rossi [20, 21] and the Feynman-alpha method derived by Richard Feynman [22, 23, 24] were developed between 1940-1970 to estimate α. In 1970 Robert Uhrig stated: "the early theoretical work in this field was carried out by Feynman, Fermi, and de Hoffman, at Los Alamos in about 1947 and led to the Rossi-alpha experiments on fast critical assemblies later described by Orndoff" [18]. From 1950-1970, the theory evolved based on advancements in instrumentation (leading to the ability to actually measure neutrons in short time gates) and availability of material to measure (to validate theory).

Work from 1970 to the early 2000s had three main focuses: (1), applying the Rossi-alpha and Feynman-alpha neutron noise techniques to the application space; (2), development of similar techniques and utilization of various detectors; and (3), advancement in electronics

(leading to the availability of list mode data) [18, 19, 25, 26, 27]. The Rossi-alpha and Feynman-alpha methods remained robust and prevailed among the most-commonly used neutron noise techniques. In the span of 2000-2017, limits on the original derivation of the two methods were identified: the Rossi- and Feynman-alpha methods were developed for bare assemblies of fissile material, which are differentiated from *reflected* assemblies where fissile material is surrounded by some material that can scatter otherwise lost neutrons back into the assembly to continue fission chains (therein increasing k_{eff}) [28, 29, 30, 31]. *The original and current theory is insufficient to account for the additional time correlations and noise introduced by a reflector* and follow-up theory by Avery and Cohn was not fully propagated to the fit models used in the measurement techniques [32, 33]. For various reasons, fissionable assemblies use a reflector: it reduces the necessary critical mass, provides a mechanism to modulate and control k_{eff}, and may be necessary for engineering reasons such as providing physical support. Certain applications interested in nuclear data (such as cross section data) for a given materials may use the material as a reflector in multiple configurations and the change in k_{eff} or other neutron noise measured parameters to improve the nuclear data. Nuclear data is broadly used by practically the entire nuclear community and beyond, most notably in predictive simulation codes, and is closely related to nuclear criticality safety. Improvements to nuclear data and neutron noise techniques require accurate quantification and propagation of measurement uncertainty. *Shortcomings in the quantification of measurement uncertainty were identified* such as the reliance on many repeated measurements or the absence of propagation, and preliminary treatment began [34, 35]. **Thus, advances in the Rossi- and Feynman-alpha neutron noise techniques are required for reflected assemblies of fissile material and for adequate uncertainty quantification.**

1.2 Thesis Overview and Contributions

In this dissertation, I begin by developing two-region point kinetics Rossi-alpha theory to account for reflectors. Similarly, I develop rigorous quantification and propagation of mea-

surement uncertainty for Rossi-alpha experiments. A current shortcoming of uncertainty quantification is the reliance on long/repeated measurements to estimate uncertainty by taking sample standard deviations. Therefore, as part of the uncertainty theory, an analytic approach based on a single measurement is developed. All of the theory is validated with measurements of weapons-grade plutonium and highly enriched uranium with various reflection. Furthermore, pulse-shape-discrimination-capable organic scintillation detectors are used and validated, and it is shown that organic scintillators augment the capabilities of the current state-of-the-art ^{3}He detectors. The Rossi-alpha technique is for near- and delayed-critical assemblies of fissile material, whereas the Feynman-alpha technique is preferred for more deeply subcritical assemblies. Thus, I derive the two-region Feynman-alpha theory from the two-region Rossi-alpha theory, validate the new equations, and derive the rigorous measurement uncertainty quantification/propagation. The two methods are preliminarily compared on the basis of accuracy as a function of criticality (k_{eff}). Taken together, **I generalize and validate the theory for the Rossi-alpha and Feynman-alpha neutron noise techniques, develop novel and rigorous quantification and propagation of measurement uncertainty, and augment current capabilities by using novel organic scintillation detectors**.

This dissertation is organized as follows; a brief summary of each chapter is given.

Chapter II describes nuclear fission and the proclivity of fissile material to sustain neutron-multiplying chains. I then present some typical quantities and the transport equation that describe multiplying assemblies, and present the derivation of the point kinetics model. Lastly, I discuss the simulations used to obtain point kinetic parameters that are often paired with measured quantities.

Chapter III describes the measurement systems – traditional detectors based on ^{3}He-gas proportional counters and novel detectors based on *trans*-stilbene organic scintillators – used in this dissertation. The detectors are generally treated as off-the-shelf tools used to obtain list mode data, a list of neutron detection times, which is required

for the neutron noise analyses.

Chapter IV presents the existing theory of Rossi-alpha measurements for bare assemblies of fissile material and the newly developed theory for reflected assemblies. Additionally, I present the new measurement uncertainty quantification and propagation theory.

Chapter V validates the new theory of Chapter IV with measurements of weapons-grade plutonium and highly enriched uranium.

Chapter VI parallels the works of Chapters IV-V and apply the theory and validation to Feynman-alpha methods. The chapter includes a preliminary comparison between the two methods.

Chapter VII summarizes the work presented in this dissertation, draw conclusions from each chapter, and propose avenues for future work.

CHAPTER II

Nuclear Fission, Multiplication, and Point Kinetics

This chapter introduces nuclear fission and the propensity of some nuclear material to sustain fission chains. The flux of neutrons within a neutron-multiplying assembly is described by the seven-variable, integro-differential transport equation. Comprehensively solving the full equation is often unnecessary and infeasible, thus it is condensed into an approximation called the point kinetics equations. The condensation is also presented in this chapter since point kinetics is the theoretical foundation of the neutron noise measurements performed to characterize multiplying assemblies. Lastly, the simulations that complement the experiments and theory are discussed.

2.1 Nuclear Fission (Chains)

Nuclear fission is a violent reaction where a large nucleus splits into unstable, energetic fragments [36]. The fission fragments initially approach stability by dissipating excitation energy and angular momentum [36, 37] by emitting multiplets of neutrons then photons. This emission is virtually instantaneous in the context of the observation tools used in this work with neutrons and photons being emitted on the femtosecond and picosecond scales, respectively. These instantaneous *prompt neutrons* are differentiated from the *delayed neutrons* emitted in further radioactive decays of the fission fragments on the larger-than-microsecond scale; such fission fragments are called delayed neutron precursors and are sometimes grouped

on the basis of time. Whereas some isotopes like ^{240}Pu undergo fission spontaneously, other isotopes like ^{235}U and ^{239}Pu do not at an appreciable rate and require that fission be induced by, for example, a neutron. The fission fragments emit charged particles in addition to the neutral photons and neutrons; however, they are generally neglected since they do not penetrate to detectors and rarely induce fission as compared to neutrons.

Assemblies of fissionable isotopes may sustain neutron-multiplying fission chains and at least facilitate chains that last for more than one generation: an initial neutron induces fission, the fission results in the emission of neutron multiplets (ranging from zero to many, with means between two and four for some common isotopes), and the resultant neutrons may continue to induce further fissions. Such multiplying assemblies are characterized by a parameter called the k_{eff} multiplication factor, defined (more rigorously in the following sections and colloquially) as the average number of neutrons from one fission that cause another fission. Assemblies that have a $k_{\text{eff}} = 1$ are called critical and assemblies that have k_{eff} less/greater than one are called subcritical/supercritical. It is common to reparametrize k_{eff} about zero in terms of reactivity ρ:

$$\rho = 1 - \frac{1}{k_{\text{eff}}}. \tag{2.1}$$

2.2 The Neutron Transport Equation

The neutron transport equation describes the balance of neutrons in space (tridimensional $\vec{x}$), direction (bidimensional Ω), energy (monodimensional E), and time (monodimensional t). The equation is a linearized form of the more-general Boltzmann equation, requiring the following assumptions.

1. Material properties in the assembly are independent of time.

2. Materials are isotropic (e.g., cross sections do not depend on incident neutron direction).

3. Quantum mechanical detail is neglected (e.g., momentum does not include nuclear spin).

4. Particle energy is sufficiently high such that particles can be treated as classical point-like objects with wave-like behavior neglected. The quantum mechanical aspects of the transport are therefore exclusively in the collision dynamics, which occur at points and are modeled using cross sections and probabilities. The effect of this assumption is to decouple the transport of the particles from the collision physics. See Ref. [38] for a full wuantum mechanical treatment.

5. Particles are only acted on by short-range forces and not by gravity or the Coulombic force (which is sufficient for the treatment of neutrons).

6. The neutron density is sufficiently low relative to other materials such that neutron-neutron interactions may be neglected, yet sufficiently high such that stochastic fluctuations are negligible.

7. Collisions are instantaneous for prompt neutrons; delayed neutrons are separately handled.

The balance is between production and loss. Production may be due to an external source $Q(\vec{x}, \vec{\Omega}, E, t)$, in-scattering from another region of phase space, or neutron-producing events such as fission. Loss may be due to leakage, out-scattering to a different region of phase space, or parasitic neutron reactions such as radiative capture, (n, γ). While many radioactive balance equations (e.g., the Bateman equations for radioactive decay) describe the balance of neutron density, N, the transport equation describes the balance of angular flux, which is equal to product of density and neutron speed, $v(E)$:

$$\Psi = \Psi(\vec{x}, \vec{\Omega}, E, t) = v(E) \times N(\vec{x}, \vec{\Omega}, E, t) = vN. \tag{2.2}$$

Angular flux has units of number of neutrons per area, per solid angle, per energy, per time. The time-dependent, seven-variate, integro-differential transport equation is given by:

$$\frac{1}{v}\frac{\partial \Psi}{\partial t} + \mathbf{L}\Psi = \mathbf{M}\Psi + \frac{1}{4\pi}\sum_i \chi_i(E)\lambda_i C_i(\vec{x},t) + Q(\vec{x},\vec{\Omega},E,t) \tag{2.3a}$$

$$\Psi^b = \Psi(\vec{x} \in \partial V, \vec{\Omega}\vec{n} < 0, E) = 0. \tag{2.3b}$$

Note that Eqn. (2.3b) defines the boundary condition (position on the boundary, $\vec{x} \in \partial V$) for incoming particles ($\vec{\Omega}\vec{n} < 0$, where $\vec{n}$ is normal to the boundary surface). In the equation,

$\chi_i(E)$ is the energy distribution for delayed neutron precursor group i,

λ_i is the decay constant for delayed neutron precursor group i,

$C_i(\vec{x},t)$ is the spatial distribution for delayed neutron precursor group i,

$\mathbf{L}$ is the net loss operator, and

$\mathbf{M}$ is the prompt fission operator.

The loss operator includes migration and is given by

$$\mathbf{L} = \vec{\Omega}\cdot\nabla + \Sigma_t(\vec{x},E) - \int\int \Sigma_s\left(E' \to E, \vec{\Omega}' \to \vec{\Omega}\right) dE' d\Omega' \ , \tag{2.4}$$

where Σ is the macroscopic cross section and subscripts denote a particular reaction; s, f, and t correspond to scatter, fission, and total. In Eqn. (2.4), Σ_s is the double-differential scattering cross section for neutrons of energy E' traveling in direction $\vec{\Omega}'$ scattering to energy E in direction $\vec{\Omega}$. The prompt fission operator omits delayed neutrons and, assuming isotropic prompt neutron emission with energy distribution $\chi_p(E' \to E)$, is given by

$$\mathbf{M} = \frac{1}{4\pi}\int\int \left(1 - \beta(\vec{x},E')\right)\chi_p(E' \to E)\nu\Sigma_f(\vec{x},E')dE'd\Omega' \ , \tag{2.5}$$

where ν is the number of neutrons emitted in a given fission event. The fraction of delayed neutrons is denoted by β. Relatedly, the delayed neutron precursor concentrations are defined by their own rate equations for each group i,

$$\frac{\partial C_i}{\partial t} + \lambda_i C_i(\vec{x}, t) = \mathbf{B}_i \Psi \tag{2.6}$$

where the loss is due to radioactive decay (second term on the left-hand side) and production (the right-hand side) is described by the group-specific delayed fission operator,

$$\mathbf{B}_i = \int \int \beta_i(\vec{x}, E')\nu\Sigma_f(\vec{x}, E')d\Omega' dE'. \tag{2.7}$$

2.3 The k-Eigenvalue Transport Equation

When an assembly is in steady state (when neutron balance is achieved), it is the case that

$$\frac{\partial \Psi}{\partial t} = \frac{dC_i}{dt} = 0. \tag{2.8}$$

The effect of the steady state assumption represented in Eqn. (2.8) on the transport equation in Eqn. (2.3a) is a convenient simplification,

$$\mathbf{L}\Psi(\vec{x}, \vec{\Omega}, E) = \mathbf{F}\Psi(\vec{x}, \vec{\Omega}, E) + Q(\vec{x}, \vec{\Omega}, E), \tag{2.9}$$

assuming the source is not varying in time. The operator $\mathbf{F}$ is the total fission operator, incorporating the delayed neutrons into $\mathbf{M}$. The k-eigenvalue approximation is a common form of Eqn. (2.9). Any boundary source and Q are set to zero ($\Psi^b = 0$), and the prompt fission source is increased or decreased by a constant factor $1/k$, resulting in:

$$\mathbf{L}\Psi(\vec{x}, \vec{\Omega}, E) = \frac{1}{k}\mathbf{F}\Psi(\vec{x}, \vec{\Omega}, E). \tag{2.10}$$

As long as Σ_f is nonzero somewhere in the assembly, there exist eigenvalues $k_0 > k_1 > k_2 > \ldots k_j > \ldots$ with nonzero eigenfunction solutions Ψ_j to Eqn. (2.10); of course, there is always the zero solution $\Psi = 0$ that is not interesting in our application space. The largest k eigenvalue, k_0, corresponding to a nonzero Ψ is the fundamental mode and effective multiplication factor: $k_{\text{eff}} = k_0$. If $k_{\text{eff}} = 1$, the angular flux in the assembly is balanced without adjustment and is said to be *critical*: the production of neutrons from fission balances the loss due to leakage and capture. When Eqn. (2.10) is exactly balanced, a finite steady-state neutron flux is possible; the value of k_{eff} can be adjusted to achieve such a balance. If $k_{\text{eff}} < 1$, the fission term is being increased to balance the equation, thus more fission is required to counteract domination by leakage and capture. Such an assembly is called subcritical. If $k_{\text{eff}} > 1$, the fission term is being constrained and such an assembly is called supercritical. Note that this model is perturbation-based and only has physical significance when $k_{\text{eff}} = 1$. Otherwise, it is a useful mathematical construct for approximating behavior at near-critical conditions: $k_{\text{eff}} \approx 1$.

2.4 The α-Eigenvalue Transport Equation

The neutron flux in a given assembly is not necessarily constant in time; there exist constants α (similar to k of the preceding section) that are eigenvalues describing the exponential time-dependent behavior of the flux. The α-eigenvalue problem is formulated by assuming that time is separable from space, direction, and energy, and writing the angular flux and delayed neutron concentrations as products of a shape function and an exponential time function:

$$\Psi(\vec{x}, \vec{\Omega}, E, t) = \psi(\vec{x}, \vec{\Omega}, E) \exp(\alpha t), \tag{2.11}$$

$$C_i(\vec{x}, t) = C_i(\vec{x}) \exp(\alpha t). \tag{2.12}$$

Equations (2.11) and (2.12) are substituted into Eqns. (2.3a) and (2.7) and the source term is neglected to produce:

$$\frac{\alpha}{v(E)}\psi(\vec{x},\vec{\Omega},E)+\mathbf{L}\psi(\vec{x},\vec{\Omega},E)=\mathbf{M}\psi(\vec{x},\vec{\Omega},E)+\frac{1}{4\pi}\sum_i \chi_i(E)\lambda_i C_i(\vec{x}), \tag{2.13}$$

$$\alpha C_i(\vec{x})+\lambda_i C_i(\vec{x})=\mathbf{B}\psi(\vec{x},\vec{\Omega},E). \tag{2.14}$$

In some applications, the time scales of interest (milliseconds or much less) are much shorter than delayed neutron precursor half-lives and delayed neutrons can therefore be neglected. The α-eigenvalue problem is hence condensed to the prompt α-eigenvalue problem:

$$\frac{\alpha}{v}\psi+\mathbf{L}\psi=\mathbf{M}\psi. \tag{2.15}$$

Note that the α/v term behaves similarly to the $1/k$ term in the k-eigenvalue equation. For supercritical systems, $\alpha > 0$. The α/v term acts as a $1/v$ absorber, which preferentially removes slower neutrons. The preferential remover is interpreted as slow neutrons being too slow to drive a supercritical transient. Similarly, $\alpha < 0$ for subcritical systems. In this case, the $1/v$ term enhances the slower neutrons, as they limit the rate of decrease of the transient. There are many α eigenvalues ($|\Re(\alpha_0)| > |\Re(\alpha_1)| > \cdots > |\Re(\alpha_j)| > \dots$) that correspond to nonzero eigenfunction solutions (and exist even if $\Sigma_f = 0$); the values may be complex, but α_0 is known to be real if it exists. Therefore the $\Re(\cdot)$ operator will henceforth be implicit. By linear independence, the spanning solution to an eigenvalue problem is the sum of all solutions. When the magnitude of α_0 (ignoring complex eigenvalues) dominates all other α magnitudes ($|\alpha_0| \gg |\alpha_1|$), the solution may be truncated from an infinite sum of exponential time functions to just one based on α_0 (this is an approximation). Such an α_0 is called the prompt neutron decay constant (discussed relative to other definitions in Sec. 2.7). It is sometimes the case that α_1 is not dominated by α_0 and the solution must include a sum of exponentials to adequately describe physical observations. Such cases motivate the work in

later chapters of this dissertation. Another development of the α-eigenvalue problem comes from writing the transport equation in terms of the neutron density and neglecting delayed neutrons:

$$\frac{\partial N}{\partial t} = (\mathbf{M} - \mathbf{L})N, \tag{2.16a}$$

$$\frac{\partial N}{\partial t} = \mathbf{A}N. \tag{2.16b}$$

Assuming some initial source $Q = Q(\vec{x}, \vec{\Omega}, E, t = 0)$, the Laplace transform results in

$$\alpha\mathcal{N} - Q = \mathbf{A}\mathcal{N}, \tag{2.17a}$$

$$\mathcal{N} = (\alpha - \mathbf{A})^{-1}Q, \tag{2.17b}$$

and the solution is a sum of the product of time-independent functions $A_j = A_j(\vec{x}, \vec{\Omega}, E)$ and exponential time functions $\exp(\alpha_j t)$ with eigenvalue α_j:

$$N(\vec{x}, \vec{\Omega}, E, t) = \sum_j A_j \exp(\alpha_j t). \tag{2.18}$$

The A_j and α_j can become messy in the context of application; however, such cases can be ignored if long-time behavior driven by the fundamental mode (and sometimes the second largest harmonic) is the focus and dominates all other modes. If the fundamental mode dominates ($|\alpha_0| \gg |\alpha_1| > \dots$) then

$$\Psi(\vec{x}, \vec{\Omega}, E, t) = Ae^{\alpha_0 t}\Psi_0(\vec{x}, \vec{\Omega}, E), \tag{2.19}$$

and A is a scalar factor determined from initial conditions and source neutrons.

2.5 The Adjoint Transport Equation

Suppose x and y are functions, and $\mathbf{A}$ and $\mathbf{B}$ are linear operators. If

$$\langle \mathbf{A}x, y \rangle = \langle x, \mathbf{B}y \rangle, \tag{2.20}$$

where $\langle \cdot \rangle$ indicates integration (or an inner product), $\mathbf{A}$ is said to be adjoint to $\mathbf{B}$:

$$\mathbf{A}^\dagger = \mathbf{B}, \tag{2.21}$$

where the $\dagger$ superscript indicates that it is the adjoint [39]. For a given operator (say $\mathbf{A}$), if

$$\langle x, \mathbf{A}^\dagger y \rangle = \langle y, \mathbf{A}x \rangle, \tag{2.22}$$

then y is the adjoint function to x (Ref. [39]):

$$x^\dagger = y. \tag{2.23}$$

The adjoint flux and adjoint transport equation (valid only when the boundary conditions are zero) are useful tools when studying the neutron flux in an assembly. A detector – whether practical or ideal and omniscient – is required to obtain information from the flux. Given a detector response function (operator – a matrix) $\mathbf{R}^\dagger$, the adjoint flux ($\Psi^\dagger$ or $\psi^\dagger$) can be interpreted as neutron importance relative to that detector. The adjoint transport equation neglecting delayed neutrons is written as [40, 41]:

$$-\frac{1}{v}\frac{\partial \psi^\dagger}{\partial t} + \mathbf{L}^\dagger \psi^\dagger = \mathbf{M}^\dagger \psi^\dagger + Q^\dagger, \tag{2.24}$$

where

$$\mathbf{L}^\dagger = -\vec{\Omega}\cdot\nabla + \Sigma_t(\vec{x},E) - \int\int \Sigma_s(\vec{x},\vec{\Omega}\to\vec{\Omega}',E\to E')d\Omega' dE', \tag{2.25}$$

$$\mathbf{M}^\dagger = \frac{1}{4\pi}\nu\Sigma_f(\vec{x},E)(1-\beta(\vec{x},E))\int\int \chi_p(E\to E')d\Omega' dE'. \tag{2.26}$$

Note that the differential operators have flipped; radiation is transported backwards relative to the lab frame of reference (e.g., from E to E') and time travels in the reverse direction. It can be shown that the "backwards" source $Q^\dagger$ must be nonzero to have nonzero solutions and is analogous to detector response ($Q^\dagger = R^\dagger$). The k_{eff}-eigenvalue adjoint equation is given by

$$\mathbf{L}^\dagger\psi^\dagger = \frac{1}{k_{\text{eff}}}\mathbf{F}^\dagger\psi^\dagger. \tag{2.27}$$

Recall that $\mathbf{F}$ is the total fission operator and $\mathbf{F}^\dagger$ is the corresponding adjoint operator. Note that the forward and adjoint $1/k_{\text{eff}}$ eigenvalues are the same. Similarly multiplying by $\Psi = \psi n$ and integrating over position, direction, and energy, and using linear algebra results in

$$\langle\psi, \mathbf{L}^\dagger\psi^\dagger\rangle n = \frac{1}{k_{\text{eff}}}\langle\psi,\mathbf{F}^\dagger\psi^\dagger\rangle n \tag{2.28a}$$

$$\langle\psi^\dagger, \mathbf{L}\psi\rangle n = \frac{1}{k_{\text{eff}}}\langle\psi^\dagger,\mathbf{F}\psi\rangle n. \tag{2.28b}$$

2.6 Point Kinetics

In practical application and diagnosis of neutron noise measurements, solving the full transport equation is typically unnecessary and can be infeasible. Therefore, the problem is sometimes simplified by condensing the equation from seven variables to just time and the result is called the point kinetics equations. The differentiation between "kinetics" and "dynamics" depends in nomenclature. The most popular nomenclature and the one followed in this work defines kinetics as the subset of dynamics without feedback, maintaining

aggregate behavior. Dynamics may allow feedback such as changing flux or temperature [42, 43].

This section develops the point kinetics equation from the transport equation defined in Eqns (2.3a), (2.4), and (2.5). It is assumed that there is no external source, long-time criteria are met such that that the assembly has reached steady state at a fundamental eigenvalue of k_{eff}, time is separable from the other six variables, and that delayed precursor groups are also in steady state.

Using the separability assumption,

$$\Psi(\vec{x}, \vec{\Omega}, E, t) = \psi(\vec{x}, \vec{\Omega}, E)n(t). \tag{2.29}$$

The separation assumes that the shape of the neutron distribution does not significantly change on the time scale of interest. When we are deeply subcritical and where higher harmonics matter, the assumption is a poor one [43]. The transport equation in Eqn. 2.3a becomes

$$\frac{1}{v}\psi\frac{dn}{dt} + \mathbf{L}\psi n = \mathbf{M}\psi n + \sum_i \chi_i \lambda_i C_i \tag{2.30}$$

using $\Psi = \psi n$ from Eqn, (2.29). Multiplying Eqn. (2.30) by the adjoint flux and integrating over position, direction, and energy results in

$$\langle \psi^\dagger, \frac{1}{v}\psi\rangle\frac{dn}{dt} + \langle \psi^\dagger, L\psi\rangle n = \langle \psi^\dagger, M\psi\rangle n + \frac{1}{4\pi}\sum_i \langle \psi^\dagger, \chi_i\lambda_i C_i\rangle. \tag{2.31}$$

Taking the difference between Eqns. (2.31) and (2.28b) results in

$$\langle \psi^\dagger, \frac{1}{v}\psi\rangle\frac{dn}{dt} = \langle \psi^\dagger, \mathbf{M}\psi\rangle n + \frac{1}{4\pi}\sum_i \langle \psi^\dagger, \chi_i\lambda_i C_i\rangle - \frac{1}{k_{\text{eff}}}\langle \psi^\dagger, \mathbf{F}\psi\rangle n. \tag{2.32}$$

It is convenient to add $\big(0 = \langle \psi^\dagger, \mathbf{B}\psi\rangle n - \langle \psi^\dagger, \mathbf{B}\psi\rangle n\big)$ to the right hand side (RHS) of Eqn. (2.32),

which results in

$$\begin{aligned} RHS &= \langle \psi^\dagger, \mathbf{M}\psi \rangle n + \frac{1}{4\pi} \sum_i \langle \psi^\dagger, \chi_i \lambda_i C_i \rangle - \frac{1}{k_{\text{eff}}} \langle \psi^\dagger, \mathbf{F}\psi \rangle n + \langle \psi^\dagger, \mathbf{B}\psi \rangle n - \langle \psi^\dagger, \mathbf{B}\psi \rangle n \\ &= \langle \psi^\dagger, \mathbf{M}\psi \rangle n + \langle \psi^\dagger, \mathbf{B}\psi \rangle n - \frac{1}{k_{\text{eff}}} \langle \psi^\dagger, \mathbf{F}\psi \rangle n + \frac{1}{4\pi} \sum_i \langle \psi^\dagger, \chi_i \lambda_i C_i \rangle - \langle \psi^\dagger, \mathbf{B}\psi \rangle n \\ &= \langle \psi^\dagger, \mathbf{F}\psi \rangle n - \frac{1}{k_{\text{eff}}} \langle \psi^\dagger, \mathbf{F}\psi \rangle n + \frac{1}{4\pi} \sum_i \langle \psi^\dagger, \chi_i \lambda_i C_i \rangle - \langle \psi^\dagger, \mathbf{B}\psi \rangle n \\ &= \left(1 - \frac{1}{k_{\text{eff}}} \right) \langle \psi^\dagger, \mathbf{F}\psi \rangle + \frac{1}{4\pi} \sum_i \langle \psi^\dagger, \chi_i \lambda_i C_i \rangle - \langle \psi^\dagger, \mathbf{B}\psi \rangle n \end{aligned}$$

and defining reactivity ρ by

$$\rho = 1 - \frac{1}{k_{\text{eff}}} \tag{2.33}$$

results in

$$\langle \psi^\dagger, \frac{1}{v}\psi \rangle \frac{dn}{dt} = \rho \langle \psi^\dagger, \mathbf{F}\psi \rangle n - \langle \psi^\dagger, \mathbf{B}\psi \rangle n + \frac{1}{4\pi} \sum_i \langle \psi^\dagger, \chi_i \lambda_i C_i \rangle. \tag{2.34}$$

Dividing through by $\langle \psi^\dagger, \frac{1}{v}\psi \rangle$ and defining the effective delayed neutron fraction

$$\beta_{\text{eff}} = \frac{\langle \psi^\dagger, \mathbf{B}\psi \rangle}{\langle \psi^\dagger, \mathbf{F}\psi \rangle} \tag{2.35}$$

and the mean neutron generation time

$$\Lambda = \frac{\langle \psi^\dagger, \frac{1}{v}\psi \rangle}{\langle \psi^\dagger, \mathbf{F}\psi \rangle} \tag{2.36}$$

results in

$$\frac{dn}{dt} = \left(\frac{\rho - \beta_{\text{eff}}}{\Lambda} \right) n(t) + \sum_i \lambda_i c_i(t) \tag{2.37}$$

with

$$c_i(t) = \langle \psi^\dagger, \frac{\chi_i(E)}{4\pi} C_i(\vec{x}, t) \rangle. \tag{2.38}$$

The prompt neutron decay constant is defined by

$$\alpha = \frac{\rho - \beta_{\text{eff}}}{\Lambda}. \tag{2.39}$$

Considering only prompt neutrons, n_p, and assuming some initial population, Eqn. (2.37) is solved with

$$n_p(t) = A + Be^{-\alpha t} \tag{2.40}$$

where A and B are constants; A corresponds to fixed sources from processes such as spontaneous fission and B is a coefficient on the exponentially decaying fundamental mode (for sub-prompt critical assemblies) of the α-eigenvalue equation. The formulation in Eqn. (2.39) motivates another definition of the prompt neutron decay constant in terms of the prompt neutron multiplication factor k_p (the component of k_{eff} due to prompt neutrons, only) and the mean prompt neutron lifetime τ_0 [44]:

$$\alpha = \frac{k_p - 1}{\tau_0}. \tag{2.41}$$

The value of k_p is defined [45] by regarding k_{eff} as sum of a prompt component, k_p, and a delayed component, k_d,

$$k_{\text{eff}} = k_p + k_d. \tag{2.42}$$

The prompt component is the ratio of number of prompt neutrons produced in the $(n+1)^{th}$ generation to the number of (any) neutrons produced in the n^{th} generation. The delayed neutron component is obtained by summing over all delayed groups and

$$k_d = \beta_{\text{eff}} k_{\text{eff}}. \tag{2.43}$$

Thus, the values of k_p, k_{eff}, and β_{eff} are related by

$$k_{\text{eff}} = \frac{k_p}{1 - \beta_{\text{eff}}}. \tag{2.44}$$

2.7 Definitions of the Prompt Neutron Decay Constant

This chapter gives rise to several definitions of the prompt neutron decay constant, α, or its negative reciprocal (when $\alpha \neq 0$), the prompt neutron period. The most correct definition of α is based on the angular flux and is defined as the logarithmic rate of change of the (prompt) neutron population in an assembly, which can be obtained by integrating Ψ/v over all phase space. Relatedly, given the density of prompt neutrons as a function of only time, $n_p(t)$,

$$\alpha(t) = \frac{d\left(\ln\left(n_p(t)\right)\right)}{dt} = \frac{1}{n_p(t)} \frac{d\left(n_p(t)\right)}{dt}. \tag{2.45}$$

Solving the transport equation is often infeasible, thus less-precise but more-practical definitions are introduced. For example, the asymptotic form is developed in the α-eigenvalue equations in Sec. 2.4 by assuming separability and describing the neutron population as a series of harmonics. The lowest-order (yet often most practical) approximation presented in this chapter is point kinetics, represented in Eqns. (2.39) and (2.41). Complete separability of time is assumed and the definitions follow from perturbations of k_{eff} from a critical reactor; thus, the model is limited as the absolute difference between k_{eff} and unity grows.

2.8 Two-Region Point Kinetics

In several historical measurements, measured results from the standard (one-region) point kinetics models disagreed with numerical solutions to the multigroup, multidimensional diffusion or transport equations. A famous case involved a measurement of a critical assembly where the point kinetics model estimated a reactivity much greater than 1\$ and Brunson called this "inexplicable behavior" the dollar discrepancy [46, 47, 48]. The anomalous be-

havior was later attributed to higher spatial harmonics, as alluded to in the α-eigenvalue section above, particularly due to the presence of neutron reflectors. Characteristic fission and neutron lifetimes are modulated when neutrons leak into a reflector region and, after some time, are scattered back into the core and continue their fission chain lineage. It has been observed that the second-largest-magnitude, real-valued α in such reflected cases is not negligible, and thus a two-region point kinetic model required. Avery developed a complex model based on the theory of coupled systems for arbitrarily many regions, each having its own multiplication factor k_j and mean neutron lifetime τ_j [32]. Avery's theory was not implementable in practice due to complexity; fitting a sum of exponentials (especially more than two) to experimental data is a mathematically ill-posed problem. Cohn adapted Avery's model for reflected assemblies considering only two regions: a core and reflector with k_c and τ_c for the core and τ_r for the reflector [33]. It is assumed that only the core produces neutrons and therefore $k_r = 0$. The models were still somewhat complex and relied on partial fluxes and separating the total fission neutron source in each region into a series of source components accounting for neutrons from one region inducing fission in another. Spriggs simplified the Avery-Cohn model by replacing the source components by aggregate cross-region leakage probabilities, f_{cr} and f_{rc}, the probability of a neutron leaking from the core/reflector to the reflector/core [49]. The point kinetic balance of neutrons in time and across the two regions is then described by writing a system of first-order differential balance equations for the neutrons in the core and reflector, N_c and N_r, in terms of f_{cr}, f_{rc}, k_c, τ_r, and τ_c. The differential equations are presented in Chapter IV; the goal of this section is to define the aforementioned terms in context of the angular flux. The two-region model has been tested and demonstrated in the inhour equation and at critical, but not for off-critical, general neutron noise measurements. The purpose of Chapter IV (and Chapter VI) is to derive the two-region point kinetic measurement techniques. The Avery-Cohn and Spriggs approaches are somewhat ad hoc and phenomenological, assume average values, and use parameters that are not necessarily measurable of physically interpretable, rather they are

mathematical constructs for convenience. These are engineering approximations that make the validation work in Chapters V and VI very important and contextualize the ranges of applicability of the two-region models.

The two-region differential equations are written in terms of the neutron population instead of angular flux as was done above for the one-region model in Eqn. (2.37). Energy in the angular flux, integrals, and inner products are reparametrized in terms of incoming and outgoing neutron velocities, v and v', for ease of units when defining time constants τ_c and τ_r. The values of τ_c and τ_r are the effective adjoint-weighted neutron lifetimes in the core and reflector regions. The effective system lifetime is

$$\tau_s = \frac{k_{\text{eff}} \int_{\text{sys}} \int \frac{\Psi^\dagger(\vec{x},v)\Psi(\vec{x},v)}{v} d\vec{x}dv}{\int_{\text{sys}\cup\text{ref.}} \int \int \Psi^\dagger(\vec{x},v)\chi(v)\nu\Sigma_f(\vec{x},v')\Psi(\vec{x},v')d\vec{x}dv'dv} \tag{2.46}$$

and, by analogy,

$$\tau_c = \frac{k_c \int_{\text{core}} \int \frac{\Psi^\dagger(\vec{x},v)\Psi(\vec{x},v)}{v} d\vec{x}dv}{\int_{\text{core}\cup\text{ref.}} \int \int \Psi^\dagger(\vec{x},v)\chi(v)\nu\Sigma_f(\vec{x},v')\Psi(\vec{x},v')d\vec{x}dv'dv}, \tag{2.47}$$

$$\tau_r = \frac{k_c \int_{\text{refl}} \int \frac{\Psi^\dagger(\vec{x},v)\Psi(\vec{x},v)}{v} d\vec{x}dv}{f_{cr} \int_{\text{core}\cup\text{ref.}} \int \int \Psi^\dagger(\vec{x},v)\chi(v)\nu\Sigma_f(\vec{x},v')\Psi(\vec{x},v')d\vec{x}dv'dv}. \tag{2.48}$$

Note that it is assumed neutron multiplication happens in the core only, and thus τ_r is defined with respect to the fraction of core neutrons leaking to the reflector. Further note that the angular dependence is ignored (assumed to cancel). With total system neutron population $N_s = N_r + N_c$, k_{eff} can be written as

$$k_{\text{eff}} = \frac{\int_{\text{sys}} \int \nu\Sigma_f(\vec{x},v)\Psi(\vec{x},v)d\vec{x}dv}{\frac{N_s}{\tau_s}} \tag{2.49}$$

and similarly,

$$k_c = \frac{\int_{\text{core}} \int \nu\Sigma_f(\vec{x},v)\Psi(\vec{x},v)d\vec{x}dv}{\frac{N_c}{\tau_c}}. \tag{2.50}$$

Again, since neutron multiplication only happens in the core,

$$k_{\text{eff}} \left(\frac{N_s}{\tau_s} \right) = k_c \left(\frac{N_c}{\tau_c} \right). \tag{2.51}$$

The instantaneous loss rates (N/τ) can be related in terms of neutron utilization fractions,

$$\left(\frac{N_c}{\tau_c} \right) = (P_{ca} + P_{ci} + P_{cr}) \left(\frac{N_s}{\tau_s} \right), \tag{2.52}$$

where P_{ca}, P_{ci}, and P_{cr} are the fraction of core neutrons that get absorbed in the core, permanently leak out of the assembly (to infinity), and leak to the reflector. The neutron utilization fractions can also be related to the cross-region leakage terms. First, as a thought experiment, the mean number of reflections $E[X]$ is calculated given f_{cr} and f_{rc}. The tree diagram for a neutron (originating in the core) is shown in Fig. 2.1.

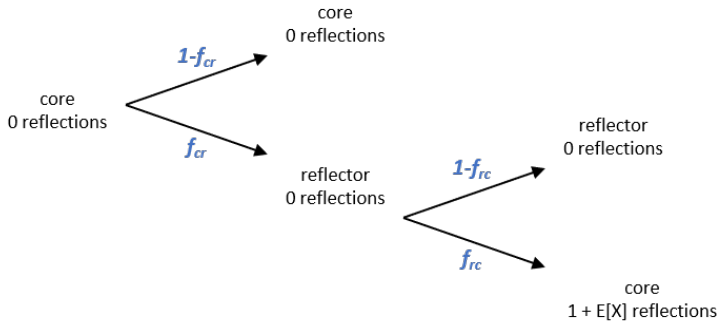

Figure 2.1: Tree diagram of neutron reflection.

The expected number of reflections is then

$$\begin{aligned} E[X] &= (1 - f_{cr})(0) + (f_{cr})((1 - f_{rc})(0) + f_{rc}(1 + E[X])) \\ E[X] &= \frac{f_{cr} f_{rc}}{1 - f_{cr} f_{rc}} \\ E[X] &= \frac{f}{1 - f}, \end{aligned} \tag{2.53}$$

where $f = f_{cr} f_{rc}$. A plot of the number of reflections as a function of f is shown in Fig. 2.2.

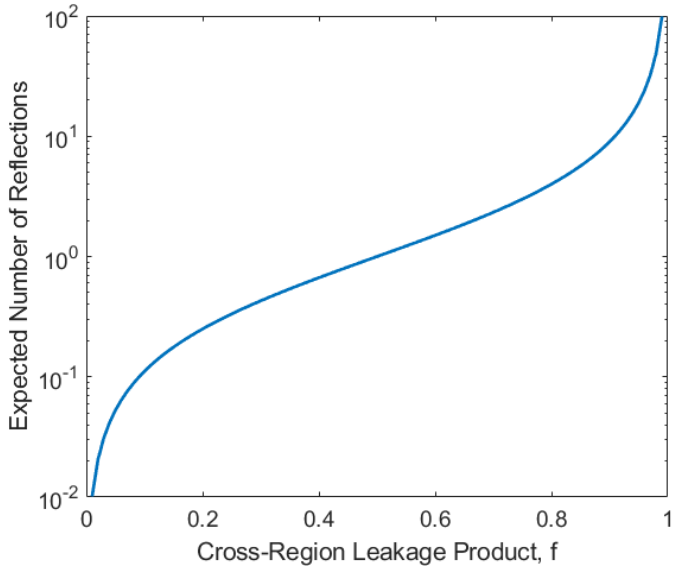

Figure 2.2: The number of reflections as a function of $f = f_{cr}f_{rc}$. The limit as $f \to 1$ is infinity.

The neutron utilization factors are related to cross-region leakage terms by

$$P_{ca} = \frac{f_{ca}}{1-f} \tag{2.54}$$

$$P_{ci} = \frac{f_{ci}}{1-f} \tag{2.55}$$

$$P_{cr} = \frac{f_{cr}}{1-f} \tag{2.56}$$

where the f_{cx} terms are single-pass probabilities. Note that $f_{ca} + f_{ci} + f_{cr} = 1$ and therefore

$$k_{\text{eff}} = \frac{k_c}{1-f}. \tag{2.57}$$

2.9 Simulation: MCNP

Simulations are a useful tool that provide additional information and insight for measurements; for example, the life of an individual neutron can be tracked. This work utilizes the

Monte Carlo N-Particle (MCNP – version MCNP6.2®[1], in particular) code [50, 51] and a derivative, auxiliary version, MCNPX-PoliMi [52]. MCNP has been extensively validated and benchmarked, and it one of the most widely-used transport codes in nuclear applications [53]. The code uses nuclear data from the Evaluated Nuclear Data File (ENDF/B-VII.1). This work uses the codes in two ways: first, the codes are used to model experiments and verify measured quantities. Second, the codes and the extra information they can track are used to independently estimate the prompt neutron decay constant and k_{eff} to validate measured results.

The KCODE subroutine of MCNP is used to invoke the MCNP6 criticality source to determine k_{eff}. Initial guesses are made for k_{eff} and $\Psi^{(0)}$, and particle histories are followed to solve for $\Psi^{(n+1)}$. Fission events during the histories are stored for the next iteration. A new k_{eff} is computed by

$$k_{\text{eff}}{}^{(n+1)} = k_{\text{eff}}{}^{(n)} \frac{\int \mathbf{M}\Psi^{(n+1)} d\vec{x}}{\int \mathbf{M}\Psi^{(n)} d\vec{x}}, \tag{2.58}$$

and the process is repeated until $\Psi^{(n+1)}$ and $k_{\text{eff}}{}^{(n+1)}$ converge. Occasionally, the iterated fission probability process (activated by the KOPTS card) is used to estimate the effective delayed neutron fraction β_{eff}, mean neutron generation time Λ, and prompt neutron decay constant at delayed critical α_{DC}. The process uses adjoint-weighted tallies by determining neutron importance in eigenvalue calculations by counting neutron progeny in a given future generation. The future generation is considered an asymptotic generation. The fixed-source subroutine SDEF is used to estimate neutron lifetimes, in particular, the mean neutron lifetime in the core region τ_c. The value of τ_c is determined with cell flux tallies (F4) where the fissile core must be defined as a single cell. The tally is inverse-velocity weighted to convert track lengths to times and also configured to estimate the total number of neutrons produced due to a seed neutron. The total lifetime is then normalized by the total neutron

[1]MCNP® and Monte Carlo N-Particle® are registered trademarks owned by Triad National Security, LLC, manager and operator of Los Alamos National Laboratory. Any third party use of such registered marks should be properly attributed to Triad National Security, LLC, including the use of the designation as appropriate. For the purposes of visual clarity, the registered trademark symbol is assumed for all references to MCNP within the remainder of this paper.

progeny plus the initial seeds to estimate τ_c.

CHAPTER III

Detection Systems: ^{3}He and Organic Scintillators

This chapter provides background on two detection systems used in the measurements of this dissertation: the Neutron Multiplicity Array Detector (NoMAD) based on ^{3}He gas proportional counters and the Organic Scintillator Array (OSCAR) based on *trans*-stilbene crystal organic scintillation detectors (henceforth called stilbene). The chapter discusses the detection mechanisms and system characteristics; additionally, initial data processing to obtain neutron list mode data (a list of neutron detection times) is presented for the OSCAR. The NoMAD has on-board electronics that output the list mode data. The detection systems are considered off-the-shelf tools used to acquire data and are not a part of the fundamental research and design of this dissertation.

The current state-of-the-art detectors for nuclear criticality safety and safeguards applications are based on moderated ^{3}He for the high detection efficiency. Recent works have shown that organic scintillators augment measurement capabilities. For example, neutron crosstalk (the phenomenon where one neutron can register multiple detections) is exploited to image radioactive sources [54, 55]. Organic scintillator systems typically do not use moderating material, thus neutrons typically do not lose energy and change direction through scattering prior to detection. Therefore organic scintillator systems are sensitive to direction and emission anisotropy [56], a portion of the energy of an incident neutron (only some of the neutron energy is deposited during detection scatters) [57], and the time resolution of

detectors are a nanosecond or less (as compared to tens-of-microseconds for ^{3}He) [58, 59]. The improved time resolution motivates the investigation of organic scintillators.

Portions of the work in this chapter were adapted from my journal article titled "Rossi-alpha measurements of fast plutonium metal assemblies using organic scintillators" published in Nuclear Instruments and Methods in Physics Research Section A: Accelerators, Spectrometers, Detectors and Associated Equipment [3].

3.1 ^{3}He Detection System

3.1.1 ^{3}He-Gas Proportional Counters

Proportional counters are gaseous tube detectors that exploit gas multiplication to amplify the signal from a charge-producing reaction. The multiplicative properties are achieved by applying a voltage to the tube such that an electric field causes electrons and ions to respectively flow to the cathode and anode. The electrons proportionally multiply during the drift when the applied voltage is sufficiently high; applying a too-low voltage results in an ion counter, whereas a too-high voltage results in a Geiger-Mueller counter. The multiplication process is a Townsend avalanche: electrons collide with other atoms on the way to the cathode, liberate more electrons in the collision, and liberated electrons perpetuate the avalanche. The signal depends on the electron drift since the ions drift more slowly. In the case of neutron detection with ^{3}He, the reaction

$$ {}^1_0n \ + \ {}^3_2\mathrm{He} \ \rightarrow \ {}^1_1\mathrm{H} \ + \ {}^3_1\mathrm{H} \ + \ 764 \text{ keV} \tag{3.1} $$

produces two charged particles: a proton and a triton. Using a ^{3}He fill gas for neutron detection is popular since the cross section for the thermal capture reaction represented in Eqn. (3.1) is 5330 barns [60] and higher than typical alternatives based on ^{10}B and ^{6}Li. The cross section is much smaller for fast neutrons; thus, ^{3}He tubes are typically embedded in a matrix of hydrogenous moderating material like high density polyethylene (HDPE) [60].

3.1.2 Neutron Multiplicity Array Detector (NoMAD)

The NoMAD comprises 15 ^{3}He detectors (Reuter-Stokes, RS-P4-0815-103) embedded in an HDPE (0.96 g/cm^3) matrix; a photo is shown in Fig. 3.1 and a schematic is shown in Fig. 3.2. Each ^{3}He tube is sealed in 0.079375-cm (1/32-inch) thick aluminum with a 2.54-cm outer diameter and a 38.1-cm tall active region. The gas is pressurized to 150 psia to increase density to increase detection efficiency. The NoMAD system has on-board electronics that processes signals to produce list mode data with a 100-ns clock-tick length, a 1.5-μs dead time per tube, and a known 35-40 μs thermalization (slowing-down) time.

Figure 3.1: Photograph of the NoMAD.

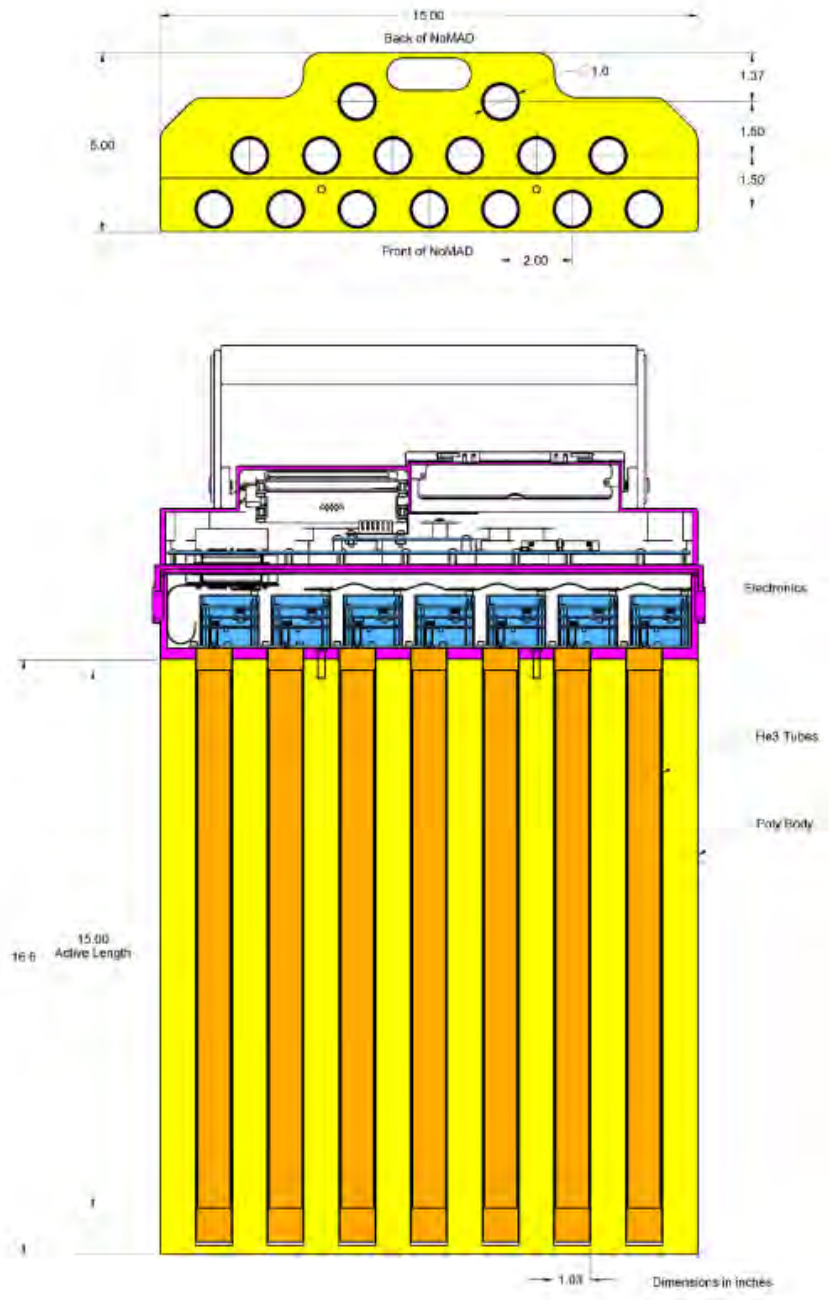

Figure 3.2: Schematic of the NoMAD; figure taken from [1].

3.2 Organic Scintillator Detection System

Organic scintillator packages are sensitive to both neutrons and photons; neutrons scatter on nuclei and photons Compton scatter on electrons [60, 61, 62]. Incident radiation transfers

energy to the organic scintillator through the scatter reaction, molecules de-excite by scintillating (emitting ultraviolet-to-visible light), and the scintillation photons are collected by a photomultiplier tuber (PMT). The energy deposited in elastic scattering by a non-relativistic neutron as constrained by conservation of energy and momentum is

$$E_{\text{deposited}} = \frac{4A}{(1+A)^2}(\cos^2\theta)E_n, \tag{3.2}$$

where E_n is the initial neutron energy, θ is the angle between the incident neutron and the recoil nucleus, and A is the ratio of the recoil nucleus mass to that of the neutron. Similarly, the energy deposited by a photon of energy E_γ is

$$E_{\text{deposited}} = E_\gamma \left(1 - \frac{1}{1+\frac{E_\gamma}{m_e c^2}(1-\cos\theta)}\right), \tag{3.3}$$

where $m_e c^2$ is the rest mass of the electron (511 keV) and θ is the angle between incident and scattered photon. The PMT converts scintillation light to electrons via the photoelectric effect in an optical window, and the electrons are multiplied by electric fields (induced by an applied high voltage) accelerating electrons into dynodes. The electrons are collected at the cathode and the voltage signal is sampled at regular time intervals by a digitizer [60].

The rest of this section will describe stilbene organic scintillators, which are used in the OSCAR system, the OSCAR itself, and the data preprocessing required to produce neutron list mode data.

3.2.1 *Trans*-Stilbene Detector

Stilbene organic scintillators are $C_{14}H_{12}$ crystals [63, 64]. Stilbene is chosen over other commercial alternatives such as EJ-309 liquid organic scintillators for the excellent PSD properties [64], further discussed in Sec. 3.2.2.1. The stilbene crystals (Inrad Optics) used in this work are 5.08-cm thick × 5.08-cm diameter cylinders; a photo of a bare crystal is shown in Fig. 3.3. Each crystal is wrapped in polytetrafluoroethylene (teflon), housed in

aluminum, and coupled to a PMT. The housing includes open cell foam on the front face, and the opposite face that is coupled to the PMT is a polished, fused silica window. The PMTs are Electron Tubes 9214B, have an active divider base (TB1102BFN2), are wrapped in mu metal magnetic shielding (MS52D), and encased in a custom 3D-printed plastic case. A schematic of the detector is shown in Fig. 3.4.

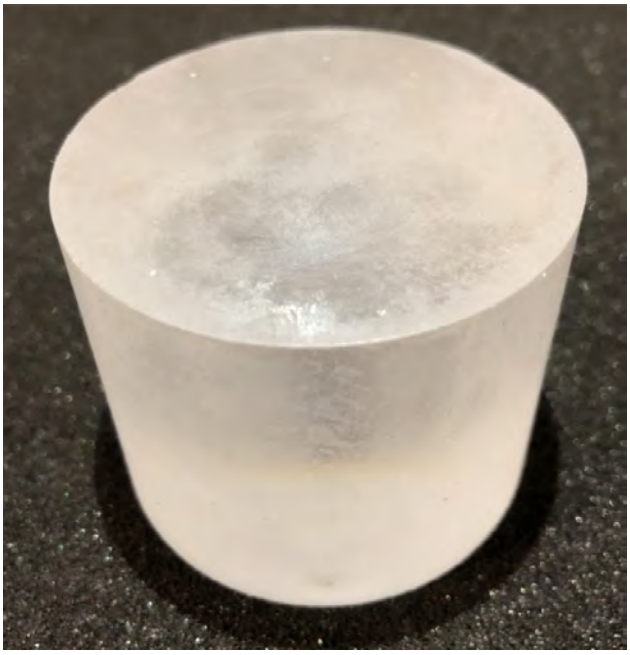

Figure 3.3: Photograph of a stilbene organic scintillator; figure from Ref. [2].

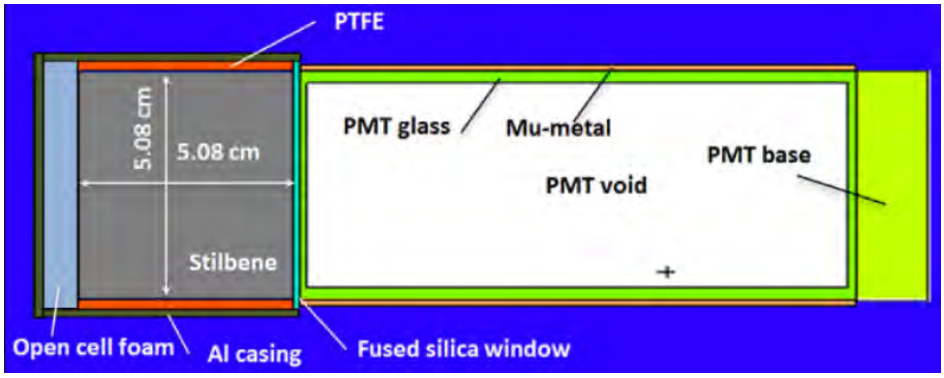

Figure 3.4: Schematic of a stilbene organic scintillator coupled to a photomultiplier tube; figure from Ref. [2].

The relationship between light output and energy deposition by a photon on an electron is adequately modeled by a linear function, whereas the relationship between light output

and neutron energy deposition on a nucleus is not. Hence, light output units (electronvolt-electron-equivalent) are defined relative to energy deposition (electronvolt) of a photon on an electron:

$$1 \text{ eV} = 1 \text{ eVee}. \tag{3.4}$$

The relationship for neutrons follows the Birks distribution (Ref. [61]) given by

$$L(E_{\text{deposited},n}) = \int \frac{a}{1 + b\left(\frac{dE}{dx}\right)} dE_{\text{deposited},n}, \tag{3.5}$$

where $\frac{dE}{dx}$ represents the differential energy deposition and a and b are parameters, typically determined from a fit [61, 65]. The value of $-\frac{dE}{dx}$ is also called the stopping power, proportional to the number of ionizations per path length, and describes the loss of energy (typically by a charged particle) as a function of distance in a medium. Other literature determined that $a = 2.027$ and $b = 27.83$ for 5.08-cm thick $\times$ 5.08-cm diameter stilbene cylinders and a sample distribution is shown in Fig. 3.5 [2].

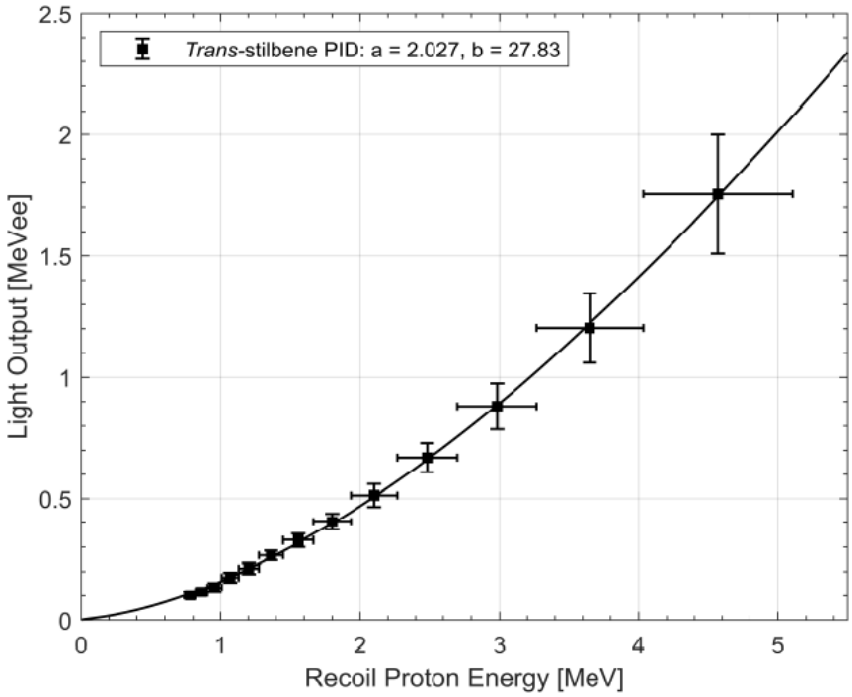

Figure 3.5: Light output distribution for 5.08-cm thick × 5.08-cm diameter stilbene cylinders; figure from Ref. [2]. Measured data points were obtained from measurements of quasi-monoenergetic neutrons.

3.2.2 Organic Scintillator Array (OSCAR)

The OSCAR comprises 12 stilbene detectors arranged in a 3×4 array; a photo is shown in Fig. 3.6. The detectors are contained in a wire frame array and held in place with porous foam (polyurethane, 0.021 g/cm^3). The housing and foam have a negligible effect on the neutron count rate.

Figure 3.6: Photo of the OSCAR system, a 3×4 array of stilbene detectors; figure from Ref. [3].

The PMTs are powered by CAEN high voltage supplies and the pulses are digitized by CAEN v1730 digitizers. The digitizer has a 500 MHz sampling rate, recording voltages from each detector every 2 ns. Constant fraction discrimination based on linear interpolation is used to achieve finer timing samples [66, 59]. In this work, the system has a time resolution of 1.34 ± 0.04 ns between two detectors, virtually negligible dead time, and no thermalization (slowing down) time like the NoMAD. Each pulse above a light output threshold of 35 keVee is afforded 144 samples or 288 ns of acquisition; thus, the dead time is *virtually* negligible, but multiple pulses in the same 288-ns window are discarded. The 35-keVee threshold is used to reduce noise, low-energy background, and room-returned radiation, and it is a good

threshold for determining detected particle type. Current and future works are using artificial neural networks to recover these piled-up pulses, but such machine learning algorithms are not used in this work [67, 68].

3.2.2.1 Data Preprocessing to Obtain List Mode Data

The pulse polarity is negative and the initial units are digitizer analog-to-digital conversion (ADC) units versus sample. Samples are converted to time by multiplying by 2 ns/sample. The dynamic range of the digitizer is 0-2 V over 14 bits (2^{14} channels), therein defining the following conversion factor. Pulse polarity is inverted and units are converted to volts by

$$(\text{Signal [V]}) = (\text{Signal [ADC]}) \times \left(\frac{2 \text{ [V]}}{2^{14} - 1 \text{ [ADC]}} \right). \tag{3.6}$$

A sample of 100 raw pulses is shown in Fig. 3.7. The sample pulses include an example of pulse pile-up (multiple pulses in the same 288 ns window); there is a second pulse between 200-250 ns. Pulses exhibiting pile-up and clipped pulses (those resulting in peak signals greater than the dynamic range) are removed.

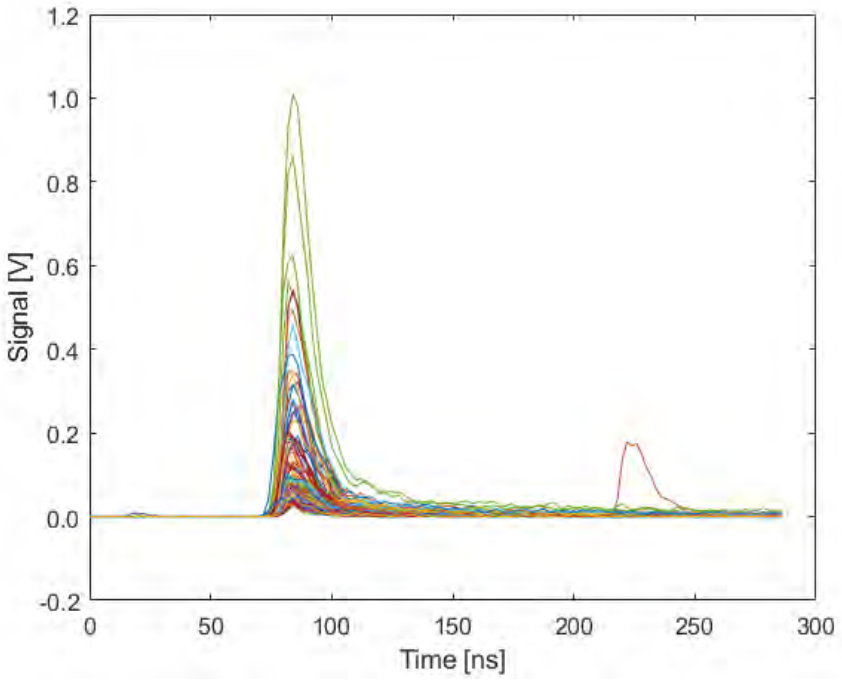

Figure 3.7: A sample of 100 pulses from an OSCAR measurement of a 4.5-kg sphere of weapons-grade plutonium reflected by 7.62 cm of tungsten.

The pulses detected in the OSCAR and the samples shown in Fig. 3.7 come from both neutrons and photons. The pulses from each type of radiation exhibit different pulse shapes – photon pulses decay more rapidly than neutron pulses as shown in Fig. 3.8 – and this phenomenon may be exploited to discriminate particle types. The difference in pulse shapes is due to different stopping powers for nuclei (protons) and electrons. The exploitation process is called pulse shape discrimination (PSD) and a charge integration technique used in this work. The ratio of the pulse tail and total integrals is compared to the total integral, resulting in Fig. 3.9. A line is drawn between the bands and pulses above/below the band are classified as neutrons/photons [69, 70, 71]. The total pulse integral (V-ns) is converted to units of light output (MeVee) via a conversion factor. The high voltage is applied to each PMT such that the pulse integral distribution Compton edge for a measurement of ^{137}Cs (corresponding to 0.478 MeVee) occurred at 1.6 V-ns, resulting in a total range of 0.035-2.389 MeVee.

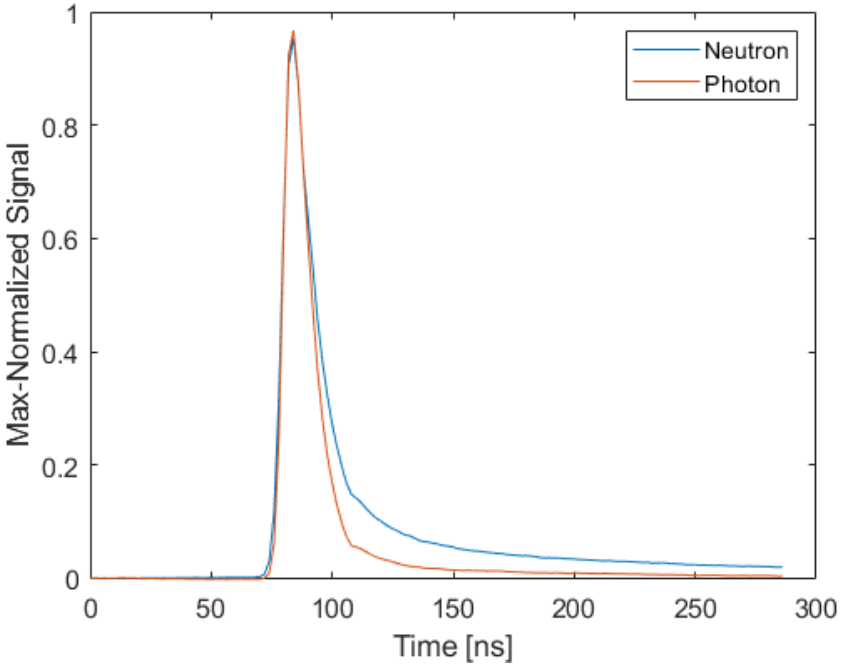

Figure 3.8: Mean, max-normalized, measured neutron and photon pulses.

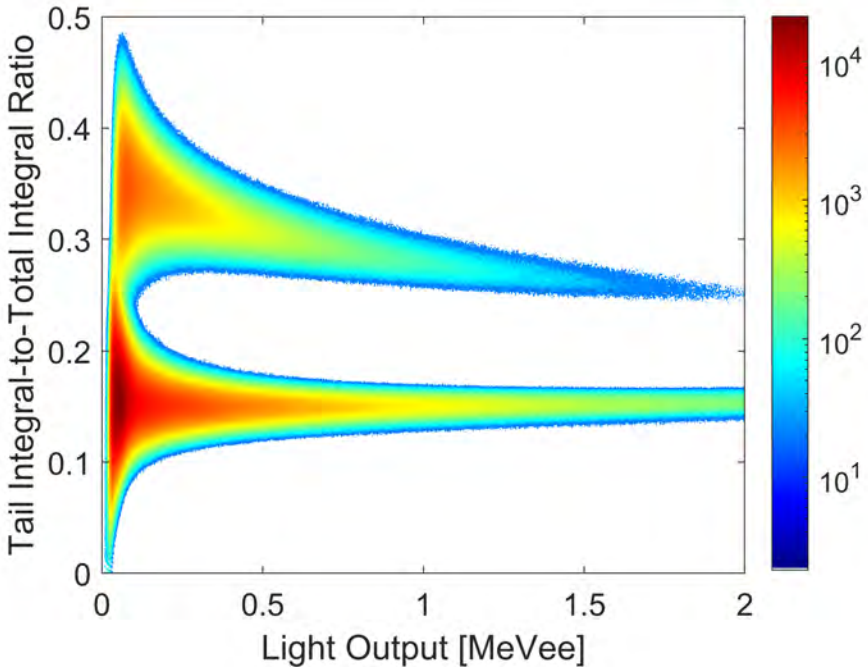

Figure 3.9: A sample pulse shape discrimination plot for a measurement of a bare spherical shell of highly enriched uranium. The top band corresponds to neutron detections, whereas the bottom band corresponds to photon detections.

One final correction is required for the OSCAR system to account for time differences due to nonuniform source-to-detector distances and electronic time offsets. Having discriminated the pulses, the photon data are used to create a time-coincidence plot between a reference detector and all other detectors. In this work, the lower left detector when looking at the front face of the OSCAR is the reference detector. A sample coincidence plot is shown in Fig. 3.10. The peak should occur at zero; if it does not, a constant time shift is applied to all neutron and photon times such that it does.

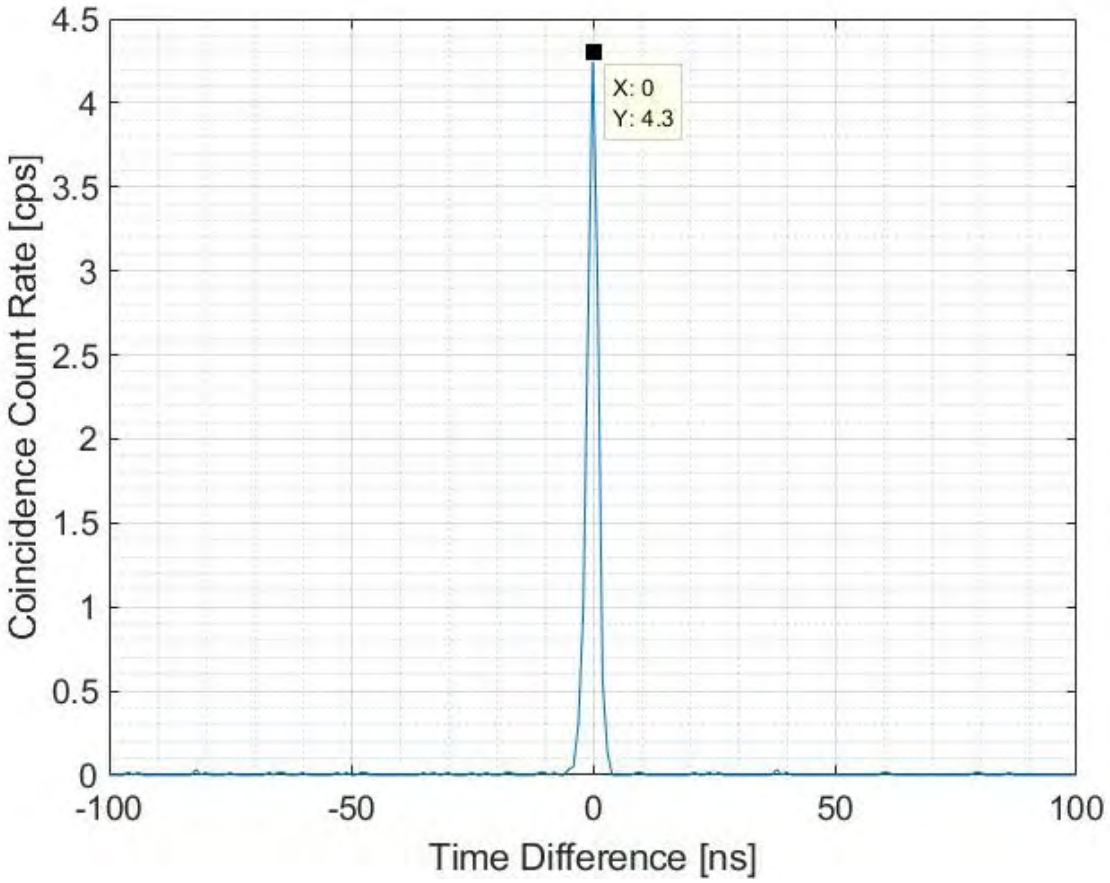

Figure 3.10: Sample photon-photon time-difference offset plot. The data peak at $x = 0$ is the expected result when there is not timing offset.

CHAPTER IV

Theory of Rossi-alpha Measurements

This chapter presents the existing theory for Rossi-alpha measurements, the new theory for Rossi-alpha measurements of reflected assemblies, and the new theory for the propagation of measurement uncertainty. The work in this chapter comes from two of my works titled "Derivation of the Two-Exponential Probability Density Function for Rossi-Alpha Measurements of Reflected Assemblies and Validation for the Special Case of Shielded Measurements" published in Nuclear Science and Engineering [72] and "Measurement uncertainty of rossi-alpha neutron experiments" published in Annals of Nuclear Energy [73].

4.1 Theory of Rossi-alpha Probability Density Functions

In a neutron-multiplying assembly, neutrons having a common ancestor are correlated in time [36, 24, 19]. One method of observing the correlation is by constructing a histogram of the time differences between the time of detection of a single neutron and the times of all subsequent neutron detections that are within a predetermined "reset time" of the original detection time [4]. The resultant plot is known as the Rossi-alpha histogram. The value of the prompt neutron decay constant, α, is experimentally determined by fitting the Rossi-alpha histogram with a probability density function (PDF) and calculating α from the fit parameters. A schematic of the time differences is shown in Fig. 4.1 and a sample Rossi-alpha histogram with a one-exponential fit is shown in Fig. 4.2; explanation of the

shape and significance of the one-exponential fit is discussed in the next subsection. Reset times are selected by experimenters such that sufficient correlated behavior is captured in the histogram for the fit to be applied. The reset time for measurements of a deeply subcritical assembly is typically much longer than typical fission chain durations.

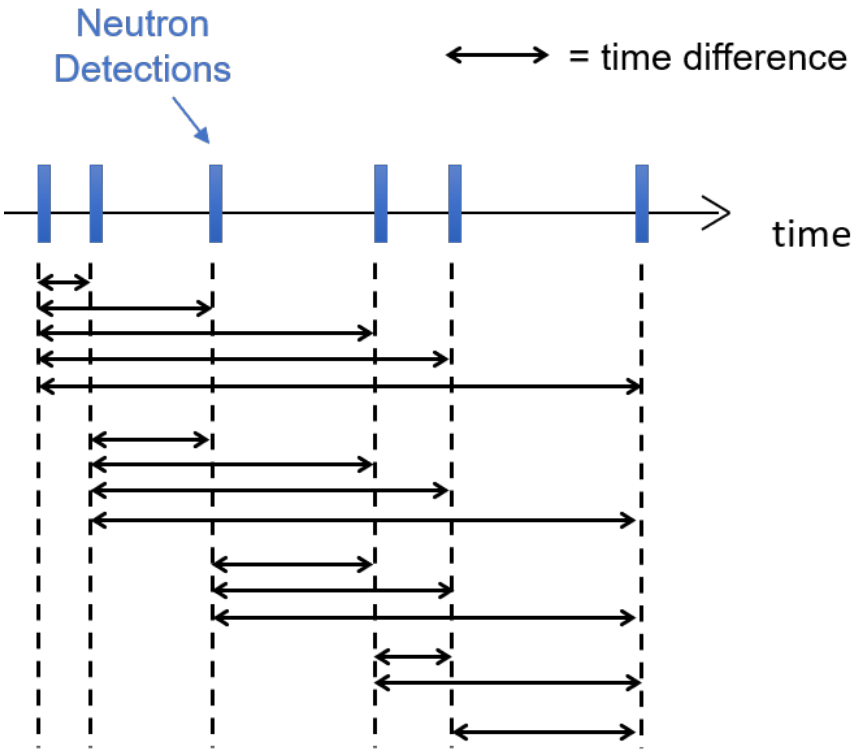

Figure 4.1: Schematic of time differences between any and all neutron detections (type-I binning [4]).

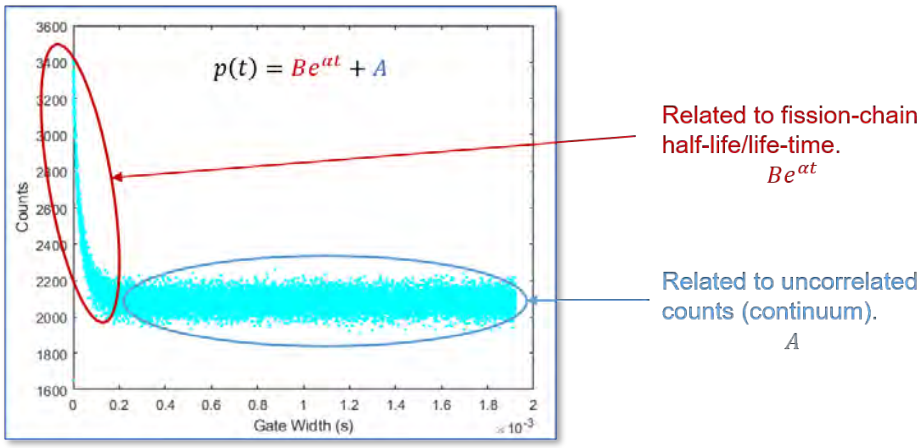

Figure 4.2: Sample Rossi-alpha plot for a NoMAD measuring a 4.5-kg sphere of weapons-grade, alpha-phase plutonium (BeRP Ball) with the one-region probability density function applied and annotated.

The derivation of the two-exp PDF will follow Orndoff's derivation of the one-exp PDF (see Reference [20]); the one-exp model is briefly summarized in Section 4.1.1. The derivation of the PDF, $p(t)$, begins with the number of prompt neutrons in a fissile core, N. In the one-region (core-only) model, $N = N_1$ is a single decaying exponential used to derive $p_1(t)$, the one-exp PDF. Section 4.1.2 uses the two-region point kinetics model (core *and reflector*) to derive $N = N_2$, a two-exponential equation. Section 4.1.3 uses N_2 (instead of N_1) in Orndoff's derivation to obtain $p_2(t)$, the two-exp PDF.

4.1.1 Traditional, One-Exp Rossi-alpha Method

Recall from Chapter II that the prompt neutron decay constant α for an assembly is given by (Ref. [20])

$$\alpha = \frac{k_p - 1}{\tau_{0,1}}, \tag{4.1}$$

where k_p is the prompt neutron multiplication factor and $\tau_{0,1}$ is the mean prompt neutron lifetime in the one-region model [20, 18, 74]. The change in subscript in this chapter ($\tau_c \rightarrowtail \tau_{0,1}$) is used to distinguish the one- and two-region definitions of τ_c until it is shown that they are the same. This work focuses on prompt neutrons; delayed neutrons are considered

chance coincidences that can be separately accounted for with a sum of exponentials [19]. Note that α in this definition is negative for sub-prompt-critical assemblies and $-1/\alpha$ is the prompt neutron period [75]. The value of α is also defined as the negative asymptotic logarithmic time derivative of the prompt neutron population in Eqn. (2.45) and (2.40) and thus the population of prompt neutrons described by one-region point kinetics N_1 at a time t due to $N(0)$ initial neutrons is mathematically described by

$$N_1(t) = N(0)e^{\alpha t}. \tag{4.2}$$

Equation (4.2) is used to derive the probability $p_1(t)dt$ of detecting a neutron between t and dt after an initial neutron detection at $t_0 = 0$. The one-exp PDF, $p_1(t)$, is given by

$$p_1(t)\ dt = A\ dt + Be^{\alpha t}\ dt \qquad \text{for } t \leq t_{\text{reset}}, \tag{4.3}$$

where A and B are constants, and t_{reset} is the reset time; $p_1(t) = 0$ for $t > t_{\text{reset}}$. The A term represents the uniform probability of uncorrelated counts, while the $Be^{\alpha t}$ term represents counts due to correlated prompt neutrons.

4.1.2 Two-Region Point Kinetics Model

The two-region point kinetics model separately considers a fissile core and a reflector region, whereas the one-region approach treats space as uniform. An aside: the reflector is defined as anything that is not the core and other terminologies like moderator or shield are considered subsets. Macroscopically, it may simple to define distinct reflector and core regions (e.g., a uranium sphere, the core, in a tank of water, the reflector) as is the case for most of the work in this dissertation. Microscopically, the regions are defined probabilistically: a uranium atom that scatters and thermalizes a neutron behaves as a reflector atom, whereas a uranium atom that absorbs a neutron and then fissions behaves as a core atom. The macroscopic interpretation is a good approximation for many assemblies and the

microscopic interpretation is like a quantum mechanical analog that is more accurate... fin aside. From References [33, 76, 31] and Chapter II, the time dependent prompt-neutron population in a reflected assembly is given by

$$\frac{dN_c}{dt} = \frac{k_{p,c} - 1}{\tau_c} N_c + f_{rc} \frac{N_r}{\tau_r} \tag{4.4a}$$

$$\frac{dN_r}{dt} = f_{cr} \frac{N_c}{\tau_c} - \frac{N_r}{\tau_r}, \tag{4.4b}$$

where:

N_c is the number of prompt neutrons in the fissile core region,

N_r is the number of prompt neutrons in the reflector,

$k_{p,c}$ is the prompt multiplication factor in the fissile core region,

τ_c is the mean prompt neutron lifetime in the fissile core region,

τ_r is the mean prompt neutron lifetime in the reflector region,

f_{cr} is the fraction of neutrons leaking from core to reflector, and

f_{rc} is the fraction of neutrons leaking from reflector to core.

Note that lifetime accounts for both leakage and absorption/capture (which may lead to fission). The differential model above assumes neutrons are only capable of multiplication in the fissile core. For small-volume (point-like) samples, the assumption generally holds and any multiplying volume is considered a part of the fissile core. When the assumptions are satisfied, all multiplication occurs in the core and thus, the total and core prompt neutron multiplication factors are the same:

$$k_{p,c} = k_p. \tag{4.5}$$

It follows from Equation (4.5) that the prompt neutron decay constant of the core α_{core} is given by

$$\alpha_{\text{core}} = \frac{k_p - 1}{\tau_c} \tag{4.6}$$

and algebraic manipulation of Equations (4.1) and (4.6) gives

$$\alpha_{\text{core}}\tau_c = \alpha\tau_{0,1} \iff \alpha_{\text{core}} = \alpha\frac{\tau_{0,1}}{\tau_c}. \tag{4.7}$$

τ_c is the prompt neutron lifetime in the core (and not the mean time to capture). In one-region point-kinetics (a reduced-order model), the entire assembly is reduced into one temporal group and time is separated from the rest of the variables. Therefore, the *total prompt neutron lifetime* and the *prompt neutron lifetime in the core* are the same, i.e.,

$$\tau_{0,1} = \tau_c. \tag{4.8}$$

In two-region analyses, the mean prompt neutron lifetime $\tau_{0,2}$ is a combination of the mean lifetimes in each region, τ_c and τ_r; the reduced-order model is more sophisticated, allowing for separate temporal behavior in the reflector and the core. The quantity $\tau_{0,2}$ is not a sum of τ_c and τ_r due to cross-region leakage. The number of neutrons in the core is to be related to the fission rate; α should describe only those neutrons in the core [20]. Therefore, combining Equations (4.1) and ((4.5)-(4.8)),

$$\alpha = \alpha_{\text{core}} = \frac{k_p - 1}{\tau_{0,1}} = \frac{k_p - 1}{\tau_c}. \tag{4.9}$$

Assuming $N_c(0) = N(0)$ and $N_r(0) = 0$, Reference [31] simultaneously solves Equations (4.4a) and (4.4b), yielding

$$N_c(t) = N(0)\left[(1-R)e^{r_1 t} + Re^{r_2 t}\right], \tag{4.10}$$

where

$$r_j = \frac{(-1)^j \sqrt{4\tau_c\tau_r(f_{rc}f_{cr} + k_p - 1) + (\tau_c - \tau_r(k_p - 1))^2} - \tau_c + \tau_r(k_p - 1)}{2\tau_c\tau_r}, \tag{4.11}$$

and

$$R = \frac{r_1 - \alpha}{r_1 - r_2}. \tag{4.12}$$

Note that $N_2 = N_c$, which will be used in Sec. 4.1.3. The coefficient R is a positive real number less than one. If a single exponential fit is adequate, R will equal one or zero, α will be one of the r_j, and Equation (4.10) reduces to a single exponential (Equation (4.3)). It is useful to define $f' = f_{rc}f_{cr}/\tau_c$; as a result, the r_j can be expressed as a function of three variables instead of five variables as seen in Equation (4.11). Using the definition of f' and Equation (4.9), Equation (4.11) simplifies to

$$r_j = (-1)^j \sqrt{\frac{1}{\tau_r}(f' + \alpha) + \frac{1}{4}\left(\frac{1}{\tau_r} - \alpha\right)^2} + \frac{1}{2}\left(\alpha - \frac{1}{\tau_r}\right), \quad \text{where} \quad f' = \frac{f_{rc}f_{cr}}{\tau_c}. \tag{4.13}$$

Having obtained Equation (4.10), the new two-exp PDF can be derived following a clarification in definition. The mean neutron lifetime in the reflector region, τ_r, is an assembly parameter equivalent to the mean neutron lifetime outside the core. A detection system is not directly sensitive to neutrons it does not detect and thus measurements are not directly sensitive to τ_r; there are biases such as energy-based thresholds and detection efficiency. Instead, measurements are sensitive to ℓ_{ctd}, the mean core-to-detection lifetime. For $\ell_{ctd} \gg \tau_c$ and $\ell_{ctd} \gg \tau_r$, ℓ_{ctd} is approximately the mean time to detection or the time between neutron birth and detection, ℓ_{ttd}. This case is common for moderated ^{3}He detectors measuring fast (sub-microsecond) assemblies. In such a scenario, the dominant eigenmodes correspond to

ℓ_{ttd} and a convolution of τ_r and τ_c. The functional dependences are

$$\ell_{ttd} = \ell_{ttd}(\tau_c, \tau_r, \ell_D) \text{ and} \tag{4.14a}$$

$$\ell_{ctd} = \ell_{ctd}(\tau_r, \ell_D), \text{ and} \tag{4.14b}$$

the nomenclature is further shown in Figure 4.3. Henceforth, τ_r is implicitly replaced by ℓ_{ctd}.

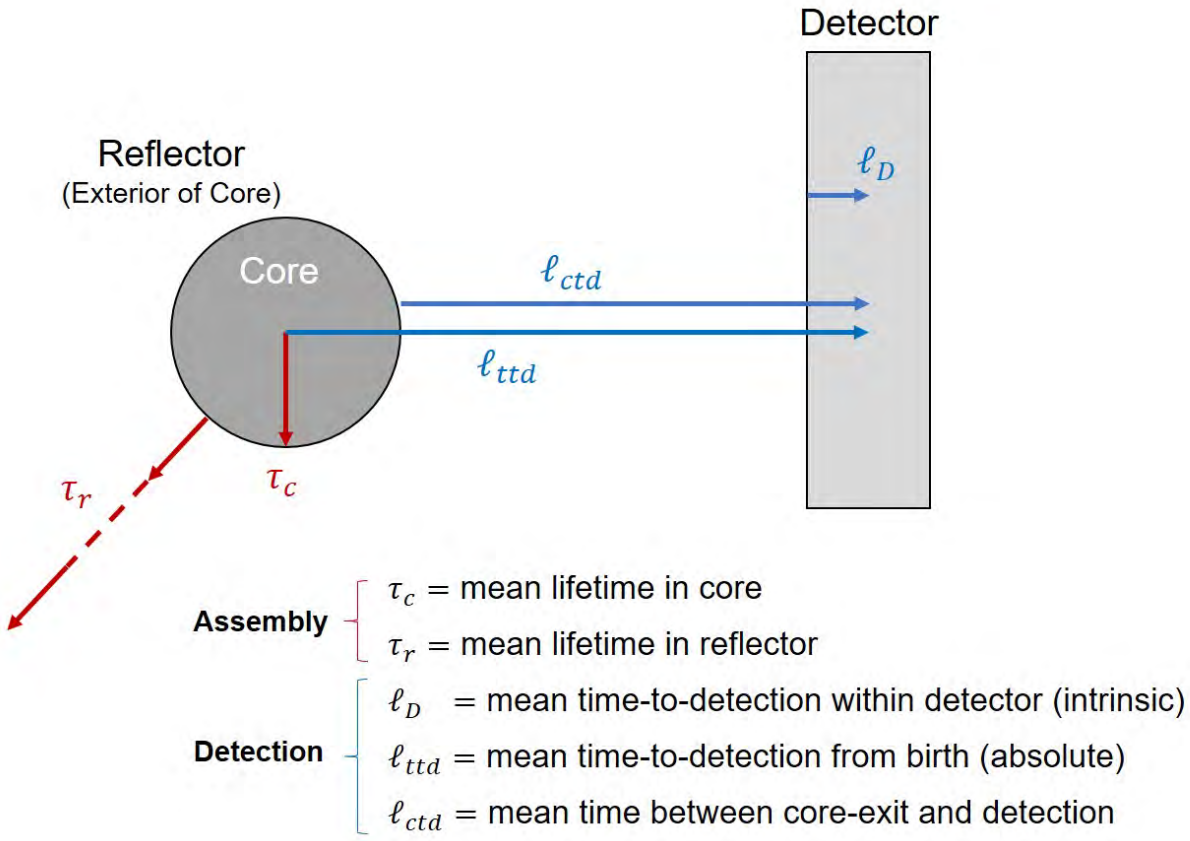

Figure 4.3: Graphic depicting the nomenclature used to describe time constants in this paper. Although only leakage is depicted, lifetimes τ also account for absorption/capture (which may lead to fission).

A second clarification is required when $\alpha_{\text{core}} \neq \alpha$ or such an assumption (negligible multiple cross-region leakages) cannot be made. The measured α_{core} corresponds to core-

only macroscopic quantities:

$$\alpha_{\text{core}} = \frac{k_{p,\text{core}} - 1}{\tau_c} \iff k_{p,\text{core}} = 1 + \alpha_{\text{core}}\tau_c \ . \tag{4.15}$$

The k_{eff} multiplication factor is calculated from $k_{p,\text{core}}$ and β_{eff} by

$$k_{\text{eff,core}} = \frac{k_{p,\text{core}}}{1 - \beta_{\text{eff}}}. \tag{4.16}$$

The total/composite k_{eff} is calculated by considering cross-region leakage terms: f_{cr}, the fraction of neutrons leaking from the core to the reflector, and f_{rc}, the fraction of neutrons leaking from the reflector to the core. Taken together,

$$\begin{aligned} k_{\text{eff}} &= \frac{k_{\text{eff,core}}}{1 - f_{rc}f_{cr}} \\ &= \frac{k_{\text{eff,core}}}{1 - f'\tau_c} \\ &= \frac{k_{p,\text{core}}}{(1 - f'\tau_c)(1 - \beta_{\text{eff}})} \\ &= \frac{1 + \alpha_{\text{core}}\tau_c}{(1 - f'\tau_c)(1 - \beta_{\text{eff}})}, \end{aligned} \tag{4.17}$$

where α_{core} and f' are measured quantities, and β_{eff} and τ_c are simulated or otherwise-obtained quantities.

4.1.3 Two-Exp Rossi-alpha Method Accounting for Reflection

This section will follow the same PDF derivation in Reference [20], which was first proposed in Reference [77]. The difference between Reference [20] and this work is Reference [20] uses $N = N_1$ (Equation (4.2)), whereas this work uses $N = N_2$ (Equation (4.10)).

Suppose there are initially ($t = 0$) $N(0)$ neutrons in a near-critical assembly. The probable number of neutrons at a time $t > 0$ is given by Equation (4.10). Hence, the probable number

of fissions produced in dt about $t > 0$ is given by

$$dF = N_2 \frac{dt}{\tau_f} = N_c \frac{dt}{\tau_f} = N(0) \frac{dt}{\tau_f} \left[(1-R) e^{r_1 t} + R e^{r_2 t} \right], \tag{4.18}$$

where τ_f is the mean time to fission. The number of resulting neutrons is given by

$$dN_2 = \overline{\nu} dF = \overline{\nu} N(0) \frac{dt}{\tau_f} \left[(1-R) e^{r_1 t} + R e^{r_2 t} \right] \tag{4.19}$$

where $\overline{\nu}$ is the mean number of neutrons produced per fission. The goal is to obtain $p_2(t)dt$, the probability of a count in $[t,t+dt]$ following a count at $t = 0$. For a purely random source following Poisson statistics, the probability is uniform following

$$p(t)\ dt = A\ dt, \quad (A\ dt \ll 1), \tag{4.20}$$

which accounts for uncorrelated counts from (α,n) neutrons and background, for example. For a (fission) source emitting correlated neutrons, $p(t)\ dt$ is expected to increase by a correlated term. To derive the correlated term, the following probabilities are needed:

I. the probability of a fission at some time t_0 in dt_0;

II. the probability of a count at t_1 in dt_1 as a result of a fission at t_0;

III. the probability of a correlated (same ancestor) count at t_2 in dt_2 assuming a count at t_1; and,

IV. the combination of probabilities I-III integrated over all time t_0 for occurrence of fission.

I is given in terms of the average fission rate in the assembly $\dot{F}_0$ as

$$\text{I.} \implies \dot{F}_0 dt_0. \tag{4.21}$$

Allowing ε to be efficiency in units of counts-per-fission, II and III can be expressed as

$$\text{II.} \implies \varepsilon\nu\frac{dt_1}{\tau_f}\left[(1-R)e^{r_1(t_1-t_0)}+Re^{r_2(t_1-t_0)}\right], \quad \text{and} \tag{4.22}$$

$$\text{III.} \implies \varepsilon(\nu-1)\frac{dt_2}{\tau_f}\left[(1-R)e^{r_1(t_2-t_0)}+Re^{r_2(t_2-t_0)}\right], \tag{4.23}$$

where ν is the number of neutrons emitted in the fission at t_0 and $(\nu-1)$ accounts for the neutron branch resulting in the count at t_1. "The final probability of a count at t_1 and a second count at t_2 from a common ancestor (not at t_1) is obtained by integrating the product of I, II, and III over $[-\infty < t_0 < t_1]$ and averaging over the distribution of neutrons emitted per fission.... Performing the integration for sub-prompt critical" (Ref. [20]) assemblies gives

$$\varepsilon\dot{F}_0 dt_1 p_2(t_1,t_2)dt_2 =$$
$$\dot{F}_0\varepsilon^2\overline{\nu(\nu-1)}\frac{dt_1dt_2}{\tau_f^2}\times\left[(1-R)^2\frac{e^{r_1(t_2-t_1)}}{-2r_1}+(R)^2\frac{e^{r_2(t_2-t_1)}}{-2r_2}+\frac{(1-R)(R)\left(e^{r_2(t_2-t_1)}+e^{r_1(t_2-t_1)}\right)}{-(r_1+r_2)}\right]. \tag{4.24}$$

"Reckoning time from $t_1 = 0$ and including the" (Ref. [20]) uncorrelated probability (Eqn. (4.20)) yields

$$p_2(t)\,dt = A\,dt - \frac{\varepsilon\overline{\nu(\nu-1)}}{2\tau_f^2}\left[e^{r_1t}\rho_1+e^{r_2t}\rho_2\right]\,dt \tag{4.25}$$

$$= A\,dt - B\left[e^{r_1t}\rho_1+e^{r_2t}\rho_2\right]\,dt \tag{4.26}$$

where

$$\rho_1 = \frac{(1-R)^2}{r_1}+\frac{2(1-R)(R)}{r_1+r_2}, \quad \text{and} \tag{4.27a}$$

$$\rho_2 = \frac{R^2}{r_2}+\frac{2(1-R)(R)}{r_1+r_2} \tag{4.27b}$$

for $t \leq t_{\text{reset}}$ and $p_2(t) = 0$ otherwise. Note that ρ_1 and ρ_2 are constants (not reactivity) with respect to t. Further note that Equation (4.25) does not satisfy normalization requirements of a PDF, but is normalizable. Normalization is not necessary in practical implementation since only r_1, r_2, and the ratio ρ_1/ρ_2 are needed to obtain α and ℓ_{ctd}; however, expressions have been derived in Reference [77, 73] and appear in Eqn. (4.44). Equations (4.25) and (4.26) are the desired results of this section: the two-exp PDF for fitting Rossi-alpha histograms of reflected fissile cores. Using Equations (4.12) and (4.13), α and ℓ_{ctd} can be obtained from the fit parameters by

$$\alpha = r_1(1-R) + r_2(R) \quad \text{and} \tag{4.28}$$

$$\ell_{ctd} = \frac{-1}{r_1(R) + r_2(1-R)}. \tag{4.29}$$

Note that α and $-1/\ell_{ctd}$ are linear combinations of the r_j exponents and, in particular,

$$\alpha + \left(-\frac{1}{\ell_{ctd}}\right) = r_1 + r_2. \tag{4.30}$$

In the case that f' is needed, it is calculated from the fit parameters by

$$f' = \frac{(R)(1-R)(r_1+r_2)(r_2-r_1)}{(R)(r_1) - (1-R)(r_2)}. \tag{4.31}$$

4.2 Theory of Measurement Uncertainty Propagation for Rossi-alpha Measurements

In this section, uncertainty propagation is analytically derived for Rossi-alpha measurements and a quasi-analytic method for determining vertical error bars for the histogram is developed. Currently, there are two main methods to estimate uncertainty.

method one. Repeat a single Rossi-alpha experiment many times to obtain many values of the prompt neutron decay constant. Estimate the uncertainty by taking the sample

standard deviation of the values.

method two. Use the standard deviation provided by the unweighted nonlinear least squares fit algorithm.

Method one requires long total measurement times to precisely estimate the uncertainty. This work develops uncertainty propagation from histogram error bars to the uncertainty in the prompt neutron decay constant and a new analytic method to infer histogram error bars that does not rely on repeated measurements. Inferring uncertainty from one measurement reduces the total measurement time and therein results in reduced procedural and operational costs.

Unlike method one, method two is different for the one- and two-exponential models. In the one-exponential model, the prompt neutron decay constant is a fit parameter, whereas the quantity is a combination of fit parameters in the two-exponential model. Thus, while taking the fit uncertainty is straightforward for the one-exponential model, the uncertainty must be propagated when the two-exponential model is used. Furthermore, simply taking the fit uncertainty does not consider the uncertainty in the data unless the fit is weighted. The uncertainty propagation developed in this work propagates uncertainty by way of weights and propagates uncertainty from the two-exponential fit parameters to the prompt neutron decay constant. We assume that the first-order Taylor series of the random variable about the meas in sufficiently accurate of the range of variation to estimate the variance (and covariance).

4.2.1 Uncertainty Propagation from Fit Parameters to Point Kinetics Parameters

The uncertainty in fit parameters is an output of many fitting algorithms; in this work, a nonlinear least squares algorithm is used. When Rossi-alpha histograms are fit with the one-exponential model (Eqn. (4.3)), α is a fit parameter and therefore σ_α is an output. When Rossi-alpha histograms are fit with the two-exponential model (Eqn. (4.26)), $\alpha =$

$\alpha(r_1, r_2, B\rho_1, B\rho_2)$ is calculated from the fit parameters and therefore the uncertainties in the fit parameters must be propagated to obtain σ_α. In this subsection, given variances in and covariances between the fit parameters, equations are derived to propagate uncertainty to α. For notational simplicity,

$$P_1 = B\rho_1 \tag{4.32a}$$

and

$$P_2 = B\rho_2. \tag{4.32b}$$

The value of α is expressed in terms of the fit parameters; namely, R is eliminated in Eqn. (4.28) by independently solving for R and substituting. The measured values P_1 and P_2 in Eqn. (4.32) depend on B, r_1, and r_2 by substituting in Eqns. (4.27a) for ρ_1 and ρ_2. The values of r_1 and r_2 are known from the fit, thus an expression for R in terms of known values is obtained by taking the ratio of Eqns. (4.32a) and (4.32b). Only one of Eqns. (4.32a) and (4.32b) would be needed to determine R if the fitting algorithm returned values for ρ_1 and ρ_2; however, both are needed to eliminate the scaling term, B. The resulting equation is

$$R = \frac{-r_2(r_1P_1 + r_2P_2) \pm \sqrt{r_1r_2(r_2P_1 + r_1P_2)(r_1P_1 + r_2P_2)}}{(r_1 - r_2)(r_1P_1 + r_2P_2)}. \tag{4.33}$$

Taking the $+$ in $\pm$ results in the physical value of R between 0 and 1. Subsequently substituting Eqn (4.33) into Eqn. (4.9) results in

$$\alpha = (r_1 + r_2) + \sqrt{r_1r_2\frac{(P_2r_1 + P_1r_2)}{(P_1r_1 + P_2r_2)}}. \tag{4.34}$$

Accounting for first-order covariance, the variance in α is:

$$\begin{aligned}
{\sigma_\alpha}^2 = &\left(\frac{\partial\alpha}{\partial r_1}\right)^2 {\sigma_{r_1}}^2 + \left(\frac{\partial\alpha}{\partial r_2}\right)^2 {\sigma_{r_2}}^2 + \left(\frac{\partial\alpha}{\partial P_1}\right)^2 {\sigma_{P_1}}^2 + \left(\frac{\partial\alpha}{\partial P_2}\right)^2 {\sigma_{P_2}}^2 \\
&+ 2\left(\frac{\partial\alpha}{\partial r_1}\right)\left(\frac{\partial\alpha}{\partial r_2}\right)\sigma_{r_1 r_2} + 2\left(\frac{\partial\alpha}{\partial r_1}\right)\left(\frac{\partial\alpha}{\partial P_1}\right)\sigma_{r_1 P_1} + 2\left(\frac{\partial\alpha}{\partial r_1}\right)\left(\frac{\partial\alpha}{\partial P_2}\right)\sigma_{r_1 P_2} \\
&+ 2\left(\frac{\partial\alpha}{\partial r_2}\right)\left(\frac{\partial\alpha}{\partial P_1}\right)\sigma_{r_2 P_1} + 2\left(\frac{\partial\alpha}{\partial r_2}\right)\left(\frac{\partial\alpha}{\partial P_2}\right)\sigma_{r_2 P_2} \\
&+ 2\left(\frac{\partial\alpha}{\partial P_1}\right)\left(\frac{\partial\alpha}{\partial P_2}\right)\sigma_{P_1 P_2}
\end{aligned} \tag{4.35}$$

The partial derivatives in Eqn. (4.35) are:

$$\frac{\partial\alpha}{\partial r_1} = 1 + \frac{P_2 r_2(2P_2 r_1 r_2 + P_1({r_1}^2 + {r_2}^2))}{\delta} \tag{4.36a}$$

$$\frac{\partial\alpha}{\partial r_2} = 1 + \frac{P_1 r_1(2P_1 r_1 r_2 + P_2({r_1}^2 + {r_2}^2))}{\delta} \tag{4.36b}$$

$$\frac{\partial\alpha}{\partial P_1} = \frac{P_2 r_1 r_2({r_2}^2 - {r_1}^2)}{\delta} \tag{4.36c}$$

$$\frac{\partial\alpha}{\partial P_2} = \frac{P_1 r_1 r_2({r_1}^2 - {r_2}^2)}{\delta} \tag{4.36d}$$

where

$$\delta = 2\sqrt{r_1 r_2(P_2 r_1 + P_1 r_2)(P_1 r_1 + P_2 r_2)^3}. \tag{4.36e}$$

Thus, given the uncertainties in the fit parameters, typically in the form of the variance-covariance matrix, the uncertainty in α is obtained from Eqn. (4.35). Sec. 4.2.2 outlines how to obtain the variance-covariance matrix.

4.2.2 Uncertainty in Fit Parameters

Suppose a fit with P number of parameters is applied to a histogram with N number of bins/data points using least squares regression. The Jacobian, J, of the fit is an $[N \times P]$ matrix and is an available output of the fitting algorithm. If the fit is not weighted, the

variance-covariance matrix, Σ, of the fit parameters is given by

$$\Sigma = (\text{RMSE})^2 \left[J^T J\right]^{-1}, \tag{4.37}$$

where RMSE is the root mean square error [78]. The diagonal of the variance-covariance matrix contains the variances of the fit parameters, and the off-diagonal terms contain the covariances. If the fit is weighted by the $[N \times N]$ matrix

$$W = \begin{bmatrix} w_{1,1} & 0 & \cdots & 0 \\ 0 & w_{2,2} & \cdots & 0 \\ \vdots & \vdots & \ddots & \vdots \\ 0 & 0 & \cdots & w_{N,N} \end{bmatrix} = \begin{bmatrix} \frac{1}{\sigma_{1,1}^2} & 0 & \cdots & 0 \\ 0 & \frac{1}{\sigma_{2,2}^2} & \cdots & 0 \\ \vdots & \vdots & \ddots & \vdots \\ 0 & 0 & \cdots & \frac{1}{\sigma_{N,N}^2}, \end{bmatrix} \tag{4.38}$$

where $\sigma_{n,n}^2$ is the variance of the n^{th} bin (therefore $\sigma_{n,n}$ is the error bar), then the variance-covariance matrix is given by [78]

$$\Sigma = \left[J^T W J\right]^{-1}. \tag{4.39}$$

The choice to use inverse variance weights minimizes the variance in the weighted least squares estimate [78]. Sec. 4.2.3 describes two methods to obtain the $\sigma_{n,n}$ needed to construct W and weight the fit.

4.2.3 Bin-by-Bin Error Bars for Rossi-alpha Histograms

Two ways to calculate vertical error bars, or the standard deviation of the number of counts in each bin, are described in this section. The first, shown in Sec. 4.2.3.1, is the sample variance method. The sample variance method uniformly divides a long measurement into many sequential, smaller ones (or uses many identical measurements) and takes the variance of the set of smaller measurements. The second method, called the analytic method, uses the

fit to calculate an average time difference and standard deviation for each bin and applies Gaussian smearing (horizontal spread) to infer the vertical error bars.

In this work, the total histogram has N bins, uniform bin widths Δ, left bin edges $t_1, t_2, \ldots, t_N$, fit $p(t)$ of the functional form described in Eqn. (4.26), and histogram values $H_1, H_2, \ldots, H_N$.

4.2.3.1 Expressions for Sample Variance Method

The error bars in the sample variance method are calculated by taking a bin-by-bin standard deviation between M many independent, identically distributed measurements. The standard deviation in the n^{th} bin (with bin edges $t_n, t_n + \Delta$) σ_n is given by

$$\sigma_n = \sqrt{\frac{1}{M-1}\sum_{m=1}^{M}\left(H_{n,m} - \overline{H}_n\right)^2}, \tag{4.40}$$

where

$$\overline{H}_n = \frac{1}{M}\sum_{m=1}^{M} H_{n,m}, \tag{4.41}$$

and $H_{n,m}$ is the histogram value in the n^{th} bin of the m^{th} repeated measurement. The equations given in this subsection are standard definitions of sample mean and standard deviation.

4.2.3.2 Expressions for Analytic Method

Heuristically, the analytic approach infers horizontal error bars (compounded uncertainties in the time of neutron detections) from the fit and uses them to estimate vertical error bars due to bin-to-bin spreading. A Gaussian-distributed spread is assumed with bin-specific means and variances calculated from the bin-specific probability density function (obtained from bin-specific normalizations of the fit). A Gaussian distribution is selected based on the high number of counts in each bin and an approximate application of the central limit theorem.

The probability density function for the j^{th} bin $p(t; t_j, \Delta)$ is given by

$$p(t; t_j, \Delta) = \eta(t_j, \Delta) p(t) \quad \text{for } t \in [t_j, t_j + \Delta), \tag{4.42}$$

where $\eta(t_j, \Delta)$ is the normalization constant for the j^{th} bin. The normalization constant is obtained by solving

$$1 = \int_{t_j}^{t_j+\Delta} \eta(t_j, \Delta) \left[A + B \left(e^{r_1 t} \rho_1 + e^{r_2 t} \rho_2 \right) \right] dt, \tag{4.43}$$

which results in

$$\eta(t_j, \Delta) = \left[A\Delta + B \left(\frac{\rho_1}{r_1} e^{r_1 t_j} \left(e^{r_1 \Delta} - 1 \right) + \frac{\rho_2}{r_2} e^{r_2 t_j} \left(e^{r_2 \Delta} - 1 \right) \right) \right]^{-1}. \tag{4.44}$$

Given the probability density function, the mean and variance are calculated analytically. The mean is given by

$$\begin{aligned} \mu(t_j, \Delta) &= \int_{t_j}^{t_j+\Delta} t p(t; t_j, \Delta) dt \\ &= \eta(t_j, \Delta) \left[A\Delta \left(t_j + \tfrac{1}{2}\Delta \right) + B(m_1 + m_2) \right], \end{aligned} \tag{4.45}$$

where

$$m_k = \frac{\rho_k}{{r_k}^2} \left(e^{r_k (t_j + \Delta)} \left(r_k (t_j + \Delta) - 1 \right) - e^{r_k t_j} (r_k t_j - 1) \right). \tag{4.46}$$

The variance is given by

$$\begin{aligned} \sigma^2(t_j, \Delta) &= \int_{t_j}^{t_j+\Delta} t^2 p(t; t_j, \Delta) dt - \mu^2 \\ &= \eta(t_j, \Delta)[A\Delta({t_j}^2 + t_j \Delta + \tfrac{1}{3}\Delta^2) + B(s_1 + s_2)] - \mu^2(t_j, \Delta), \end{aligned} \tag{4.47}$$

where

$$s_k = \frac{\rho_k}{{r_k}^3}\left(e^{r_k(t_j+\Delta)}\left((r_k(\Delta+t_j))^2 - 2r_k(\Delta+t_j)+2\right) - e^{r_k t_j}\left((r_k t_j)^2 - 2r_k t_j + 2\right)\right) \quad (4.48)$$

Using the mean and variance above, the random distribution for the time t in bin j is assumed to be normally distributed as

$$G(t;t_j,\Delta) = \frac{1}{\sqrt{2\pi\left(x\sigma(t_j,\Delta)\right)^2}} \exp\left(\frac{-(\mu(t_j,\Delta)-t)^2}{2\left(x\sigma(t_j,\Delta)\right)^2}\right), \quad (4.49)$$

where x is the number of standard deviations; $x = 1$ and 3 correspond to 68.3% and 99.7% confidence intervals, respectively. Note that larger values of x result in diminishing returns by nature of the exponential decay of the Gaussian away from the mean and that any value of $x \geq 3.5$ are essentially equivalent. This work arbitrarily uses seven standard deviations, twice the 3.5 limit, which corresponds to a $(100 - 3\times10^{-10})\%$ confidence interval. Note that these confidence intervals are only valid when considering a single bin since there is correlation between different bins; by applying these confidence intervals to all bins in the same measurement, we are making an approximation by ignoring the correlated effect and could see deviations.

Heuristically, the probability of a bin j count belonging in bin i, $q_i(j)$, is equal to the area under $G(t;t_j,\Delta)$ between the bounds of bin i, $[t_i, t_i+\Delta)$ (note that $G(t;t_j,\Delta)$ is normalized). The value of $q_i(j)$ is given by

$$q_i(j) = \int_{t_i}^{t_i+\Delta} \frac{1}{\sqrt{2\pi\sigma^2(t_j,\Delta)}} \exp\left(\frac{-(\mu(t_j,\Delta)-t)^2}{2\sigma(t_j,\Delta)^2}\right) dt \quad (4.50)$$

$$= \frac{1}{2}\left[\operatorname{erf}\left(\frac{(t_i+\Delta)-\mu(t_j,\Delta)}{\sqrt{2\sigma^2(t_j,\Delta)}}\right) - \operatorname{erf}\left(\frac{t_i-\mu(t_j,\Delta)}{\sqrt{2\sigma^2(t_j,\Delta)}}\right)\right]. \quad (4.51)$$

The binomial theorem is applied to calculate the variance in bin i due to bin j and

summed over all j to get the total variance ${\beta_i}^2$ (and the error bar is β_i). Taken together,

$$ {\beta_i}^2 = \sum_{j=1}^{N} p\big(\mu(t_j, \Delta)\big) \times q_i(j)\big(1 - q_i(j)\big). \tag{4.52} $$

4.2.4 Uncertainty in Error Bars for the Purpose of Validation

This section develops equations for the variance of the variance, Var[Var[X]], where X is a random variable. Error bars from the sample variance and analytic methods will be compared for validation, thus uncertainty or variance of the variance Var[Var[X]] is needed (the content in this subsection is not required for the implementation of the uncertainty analysis). In terms of the moments μ_i (defined by $\mu_i = \mathrm{E}[X^i]$),

$$ \mathrm{Var}[\mathrm{Var}[X]] = \mu_4 - 4\mu_3\mu_1 + 8\mu_2{\mu_1}^2 - {\mu_2}^2 - 4{\mu_1}^4. \tag{4.53} $$

Note that Eqn. (4.53) is a biased estimate of the variance of the variance that is adequate for large samples. To give Eqn. (4.53) meaning in the context of this work, the moments for the sample variance and analytic methods must be calculated. The moments for the j^{th} bin in the sample variance method $\mu_i^s(j)$ are

$$ \mu_1^s(j) = \frac{1}{M}\sum_{m=1}^{M} H_{j,m}, \tag{4.54a} $$

$$ \mu_2^s(j) = \frac{1}{M}\sum_{m=1}^{M} H_{j,m}^2, \tag{4.54b} $$

$$ \mu_3^s(j) = \frac{1}{M}\sum_{m=1}^{M} H_{j,m}^3, \tag{4.54c} $$

and

$$ \mu_4^s(j) = \frac{1}{M}\sum_{m=1}^{M} H_{j,m}^4. \tag{4.54d} $$

The first four moments for a binomial distribution with n trials and probability p are [79]

$$\mu_1(j) = np, \tag{4.55a}$$

$$\mu_2(j) = np(1 - p + np), \tag{4.55b}$$

$$\mu_3(j) = np(1 - 3p + 3np + 2p^2 - 3np^2 + n^2p^2), \tag{4.55c}$$

and

$$\mu_4(j) = np(1 - 7p + 7np + 12p^2 - 18np^2 + 6n^2p^2 - 6p^3 + 11np^3 - 6n^2p^3 + n^3p^3). \tag{4.55d}$$

The analytic method assumes a binomial model with $n = p(\mu(t_j, \Delta))$ and $p = q_i(j)$.

CHAPTER V

Validation of New Rossi-alpha Theory

The work presented in this chapter comes from two of my publications titled "Validation of the two-region Rossi-alpha model for reflected assemblies" published in Nuclear Instruments and Methods in Physics Research Section A [6] and "Measurement uncertainty of rossi-alpha neutron experiments" published in Annals of Nuclear Energy [73]. The purpose of this chapter is to validate the two-region point kinetics model and associated uncertainty quantification/propagation for Rossi-alpha experiments on reflected assemblies. The two-region model and uncertainty theory (presented in Chapter IV) are validated with experimental data from uranium and plutonium by comparing measured values to simulated values, which are treated as the reference in this work.

5.1 Introduction and Experimental Setups

The experiments described in this chapter were performed at the National Criticality Experiments Research Center within the Device Assembly Facility at the Nevada National Security Site. The apparatus arrangement are the same for all experiments; the differences are the assembly (combination of fissionable material and reflector), the detector that is used, and the objective of the experiment. There are three objectives: validate the two-region Rossi-alpha theory presented in section 4.1.3, the analytic quantification of bin-by-bin Rossi-alpha histogram uncertainty presented in section 4.2.3.2, and the propagation of

measurement uncertainty presented in sections 4.2.1 and 4.2.2. A broad summary of the assemblies, detectors from which data are analyzed, a link to the corresponding results section, and reference are given in Tab. 5.1. Subsections in this experimental setups section detail the assemblies in greater detail. The front face of each detection system was 47 cm from the center of the radiation test object; the layout and detection systems are identical to those of Ref. [3] and a photo is shown in Fig. 5.1. Two types of detection systems were present during the experiments: two organic scintillator arrays (OSCARs) [3] and two Neutron Multiplicity Array Detectors (NoMADs) [1], detailed in Chapter III.

Table 5.1: Tabulated list of experimental objectives and the associated assemblies that were measured.

Objective	**SNM**	**Reflector**	**Detector**	**Section**	**References**
Validate the Two-Region Rossi-alpha Theory	BeRP Ball – Pu	Cu	OSCAR	5.3	[6]
	Rocky Flats – U	HDPE	OSCAR		
Validate bin-by-bin analytic uncertainty quantification	BeRP Ball – Pu	Cu	OSCAR	5.5.1	[73]
	BeRP Ball – Pu	Poly and Cu	NoMAD		
Validate Uncertainty Propagation	BeRP Ball – Pu	Ni, Cu, or W	OSCAR	5.5.2	[73]

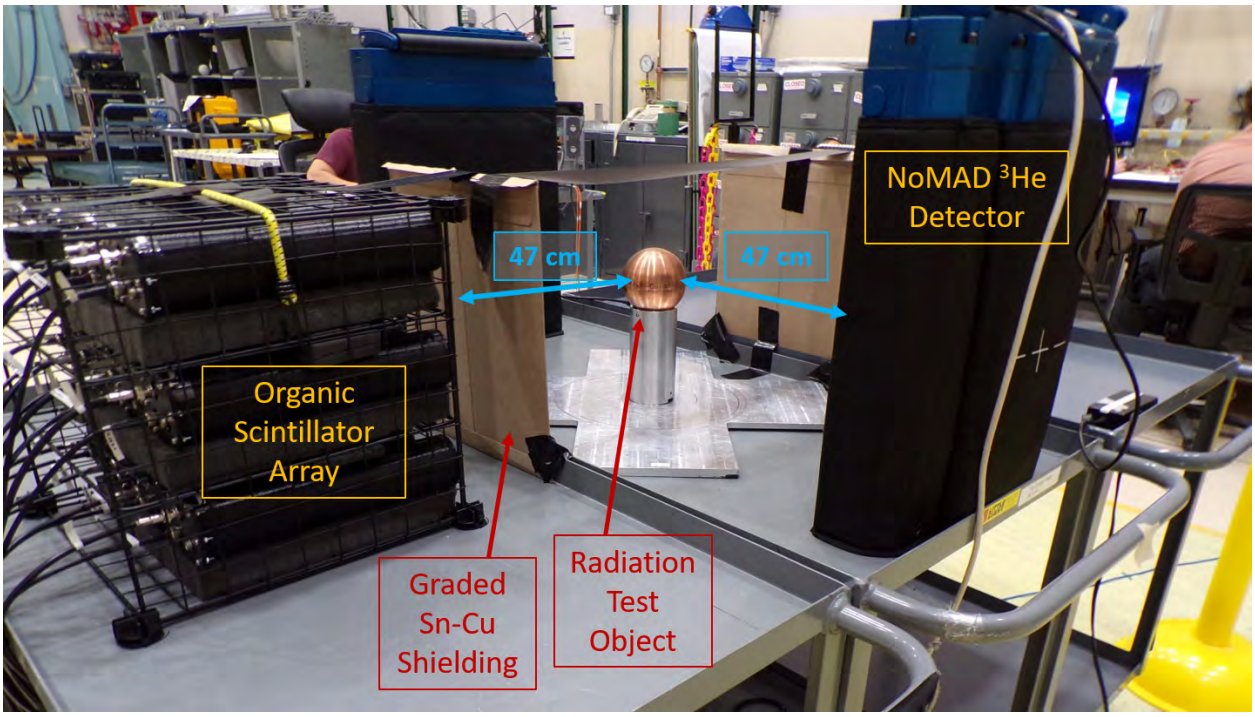

Figure 5.1: Annotated layout of detection systems and measurement setup.

The plutonium assemblies use a 4.5-kg sphere of weapons-grade (93% ^{239}Pu), alpha-phase plutonium encased in stainless steel known as the BeRP Ball [80, 81]. The BeRP Ball has recently been used in several benchmark measurements that comprehensively specify the object and provide detailed MCNP input files [82, 83, 1]. The measured uranium radiation test object is made from shells of highly enriched uranium (HEU, 93.16% ^{235}U) known as the Rocky Flats shells [84]. The composite shell contains Rocky Flats shells 3-30, is encased in aluminum for contamination control, has inner and outer HEU diameters of 4.02 and 13.34 cm, and totals a mass of 21.6 kg.

5.1.1 Assemblies for the Validation of the Two-Region Rossi-alpha Model

The measurements for this first objective replicate the copper-only configurations of the subcritical copper-reflected α-phase plutonium (SCRαP) benchmark [1], where the BeRP Ball is reflected by tight-fitting copper shells with thicknesses ranging from 1.27 cm to 10.16 cm in 1.27 cm increments. Photos of the configurations are shown in Fig. 5.2. Each con-

figuration was measured for 20 minutes. These configurations were selected since the fissile core remains constant and the amount of reflector is modulated to attain k_{eff} values ranging from 0.8278 - 0.9394 as calculated from MCNP KCODE simulations (see section 5.2.1) and in agreement with the SCRαP benchmark [1].

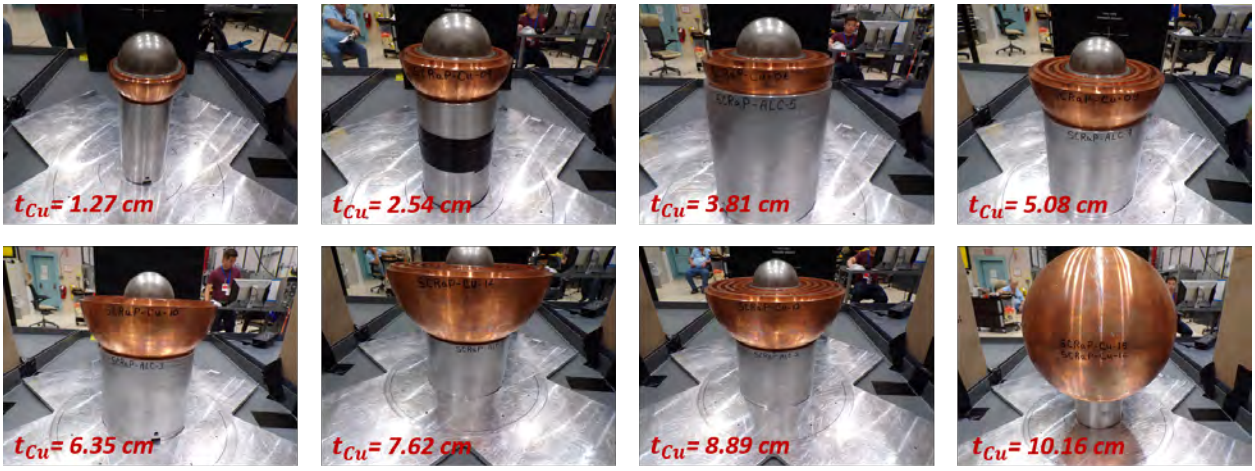

Figure 5.2: Photos of the BeRP Ball reflected by various copper thicknesses; the other half of the reflector shells are affixed during measurement.

A rendering of the unencased HEU Rocky Flats shells that form the fissile core is shown in Fig. 5.3. A total of three configurations were measured: the core (shown in Fig 5.4), the core reflected by 3.81 cm of high-density polyethylene (HDPE), and the core reflected by 6.35 cm of HDPE. The assembly was driven by a ^{252}Cf source that was taped to the bottom of the assembly; the source-to-sample distance changes between configurations. Each configuration was measured for 30 minutes. These configurations were again chosen for the fixed fissile core and varying reflector that achieves k_{eff} values between 0.7325 - 0.9508 as calculated from MCNP KCODE simulations (see section 5.2.1).

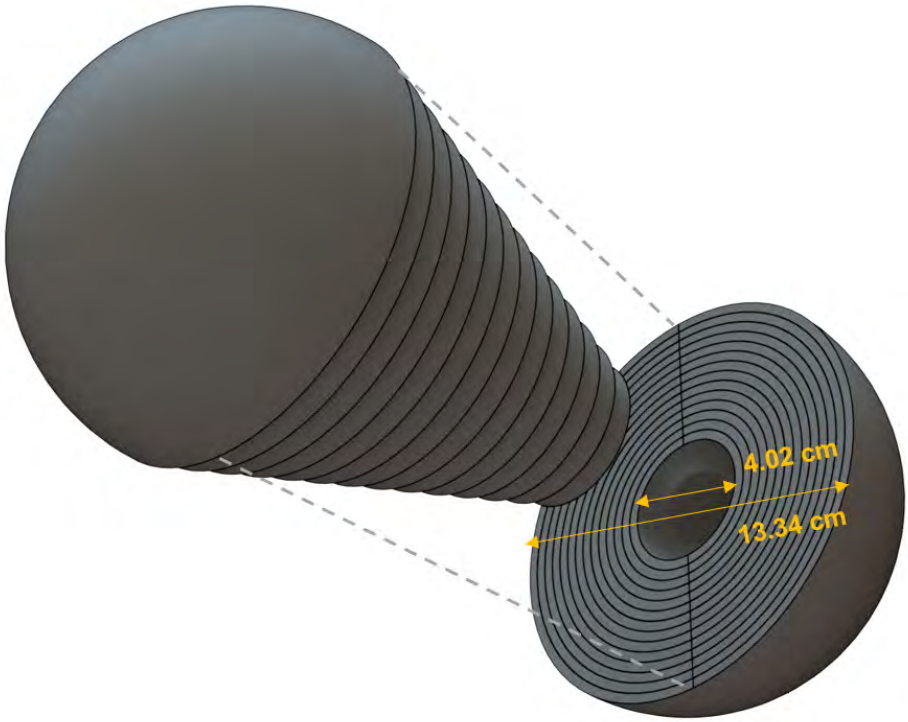

Figure 5.3: Three-dimensional rendering of Rocky Flats shells 3-30 with inner and outer diameters of 4.02 and 13.34 cm.

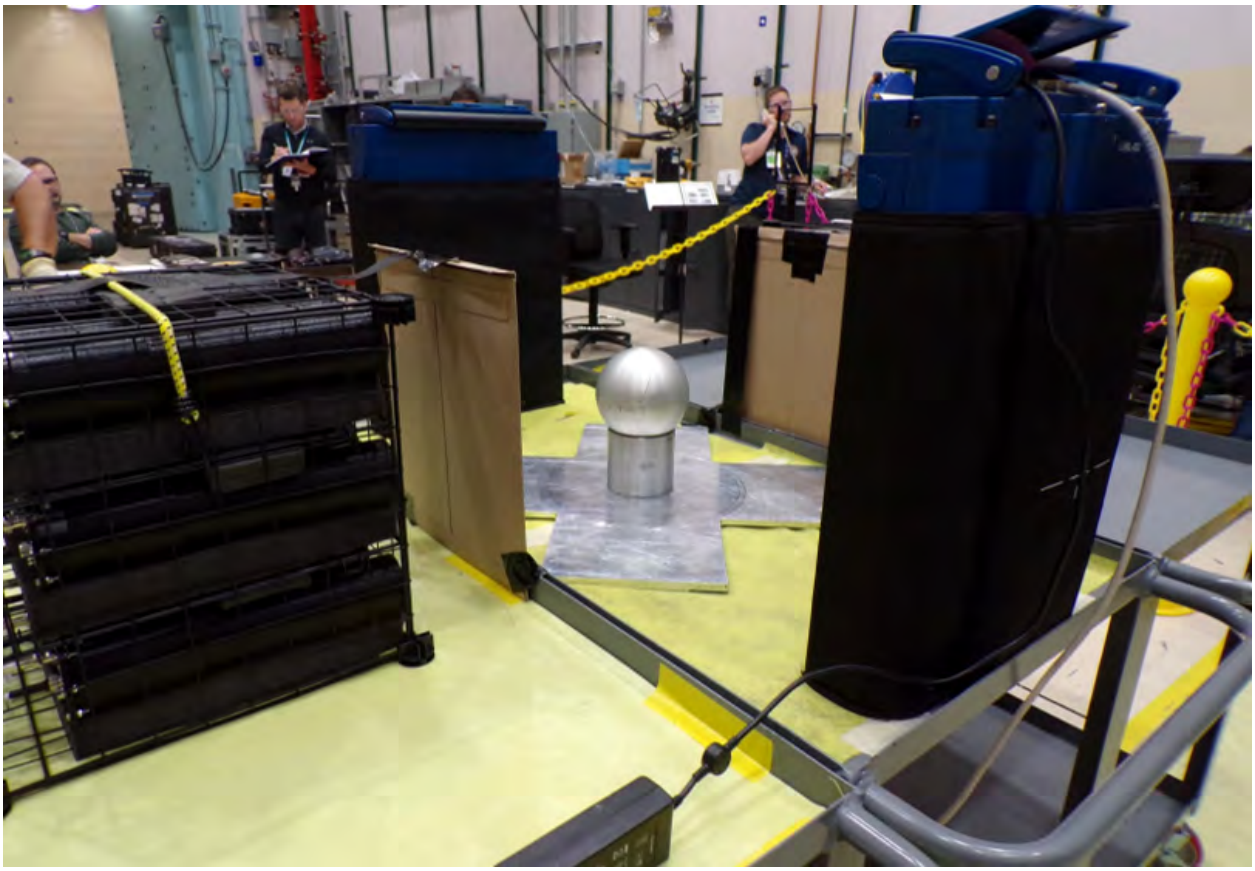

Figure 5.4: A photo of the measurement setup for the Rocky Flats experiment; in particular, the bare case is shown.

5.1.2 Assemblies for the Validation of Rossi-alpha Measurement Uncertainty Quantification and Propagation

The experiments for uncertainty validation also used the BeRP Ball. The BeRP Ball [81] was used in several benchmarks with the tungsten [83], nickel [85, 82], copper, and heterogeneous reflectors [1], all containing comprehensive details on the apparatus and materials; the k_{eff} of the assemblies were 0.948, 0.916, 0.932, and 0.951, respectively [3, 1]. Photos of the assemblies with half of the hemishells removed are shown in Fig. 5.5; note that the nickel reflector in Fig. 5.5b is completed with cylindrical slugs [85, 82].

(a) **(b)**

(c) **(d)**

Figure 5.5: Configurations used in the experiments. The BeRP ball is reflected by 7.62 cm of tungsten, nickel, or copper shown in Figs. 5.5a, 5.5b, and 5.5c, respectively. Fig. 5.5d shows the BeRP ball reflected by 3.81 cm of polyethylene and 5.08 cm of copper.

The copper-reflected case was measured by an OSCAR for 20 minutes (the same measurement as the 7.62-cm case of Sec. 5.1.1) and the tungsten and nickel cases were measured by an OSCAR for 30 minutes. The heterogeneously-reflected BeRP Ball with high-density polyethylene and copper was measured for 75 minutes with two NoMADs. The front face of the NoMAD detectors were 50 cm from the center of the assembly and the optional cadmium

liners were not used; the detection system and setup are identical to the one used in Ref. [1]. A photo of the heterogeneous-reflector case is shown in Fig. 5.6, since it differs from all other configurations in this section.

Figure 5.6: Photo of the experimental setup for the ^{3}He measurements.

5.2 Data Analysis

The output of the NoMAD is list mode data, a list of neutron detection times. Preliminary pulse processing to obtain list mode data for the OSCAR assemblies is described in Chapter III. Pulse shape discrimination (PSD – see Chapter III) is performed to separate neutron and photon pulses since organic scintillators are sensitive to both types of radiation. Sample PSD plots for copper-reflected plutonium and bare HEU are respectively shown in Figs. 5.7 and Figs. 5.8.

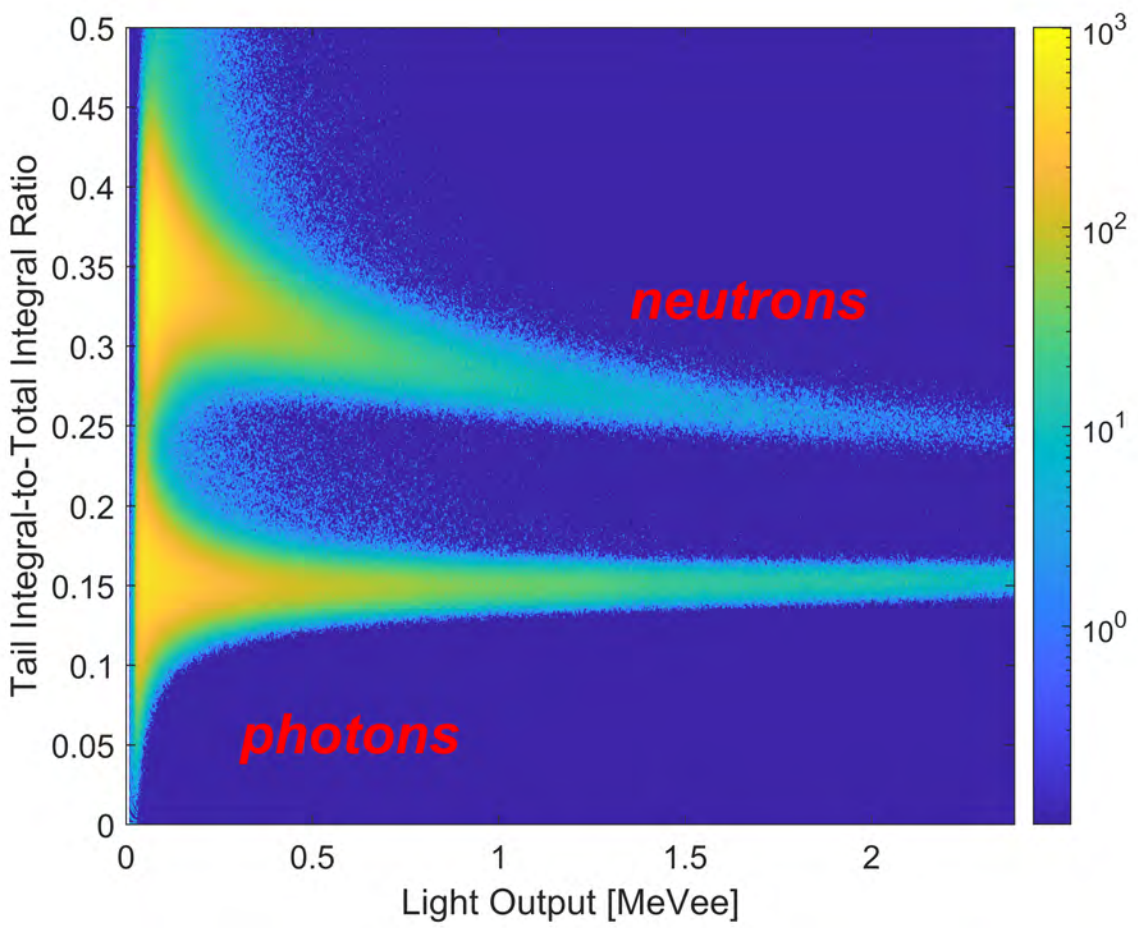

Figure 5.7: Pulse shape discrimination plot for the organic scintillator measurement of the copper-reflected plutonium.

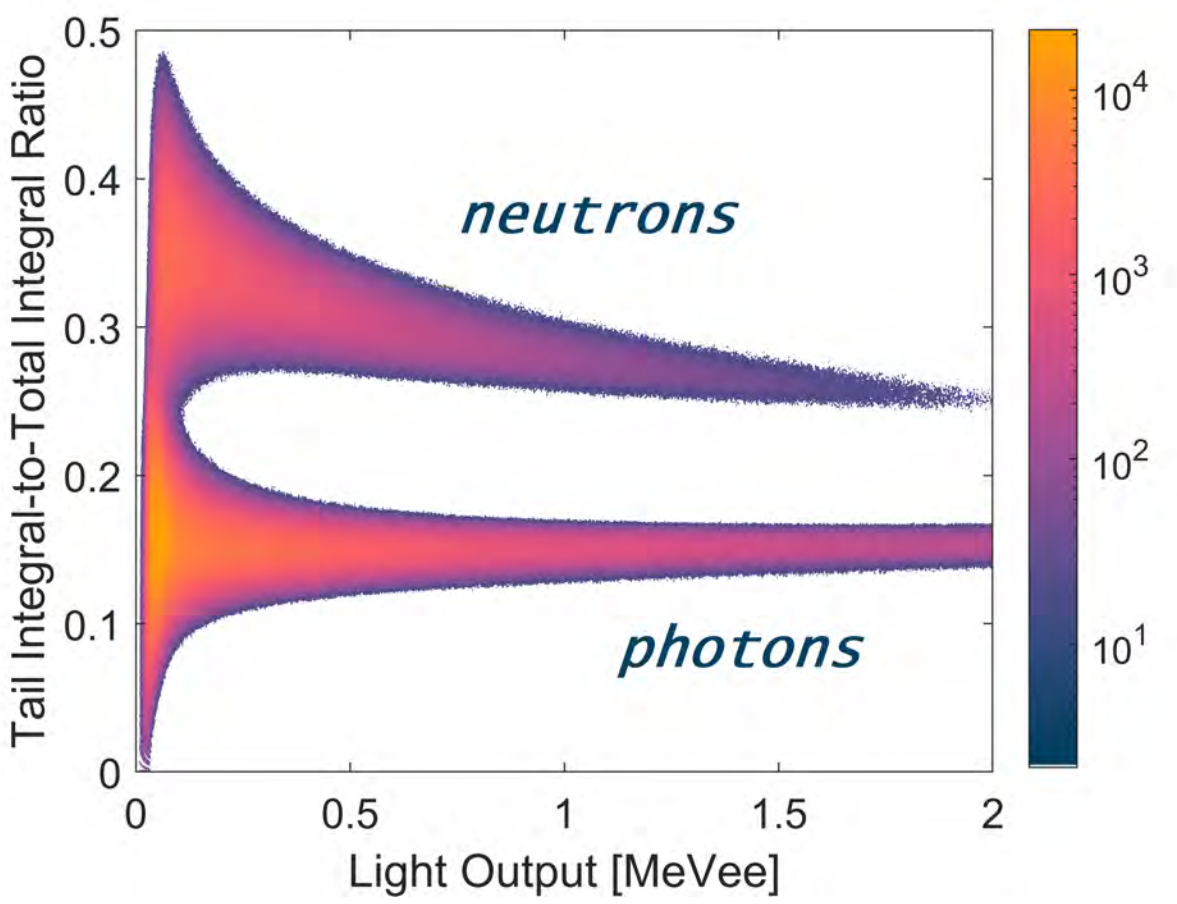

Figure 5.8: Sample pulse shape discrimination plot for the bare HEU assembly.

Time differences less than a given reset time – 1 μs for the OSCAR and 80 μs for the NoMAD – are calculated between any and all neutron detections (type-I binning [4]) and a histogram of resultant values is constructed for each configuration. The organic scintillator array uses 1-ns bin widths, whereas the NoMADs use 100-ns bin widths. Each histogram is constant-subtracted by subtracting the mean of the tail and the first $2b + 1$ points are omitted in the fit, where b is the index of the bin with the most counts. The $2b+1$ lower time-difference threshold accounts for dead time and short time-correlated effects such as neutron cross talk [3]. Nonlinear least squares fitting is used to fit Eqn. (4.26) (without the A term, which is accounted for in the constant subtraction) to the histograms and Eqn. (4.28) is used to calculate $\alpha = \alpha_{\text{core}}$. The k_{eff} multiplication factor is calculated using Eqn. (4.17). Unless

otherwise noted, the methodologies described in Chapter IV are used to inverse-variance weight fits (when applicable) and calculate uncertainties; the sample method is used in this work. All error bars shown in this work are one standard deviation, σ.

5.2.1 Simulations to Obtain Reference Values

There are three simulated parameters from the simulations of the experiments: k_{eff}, β_{eff}, and τ_c. The KCODE subroutine of MCNP6.2 is used to simulate the k_{eff} values, which are considered ground truth reference values in this work. A three-dimensional rendering of the simulation geometry is shown in Fig. 5.9.

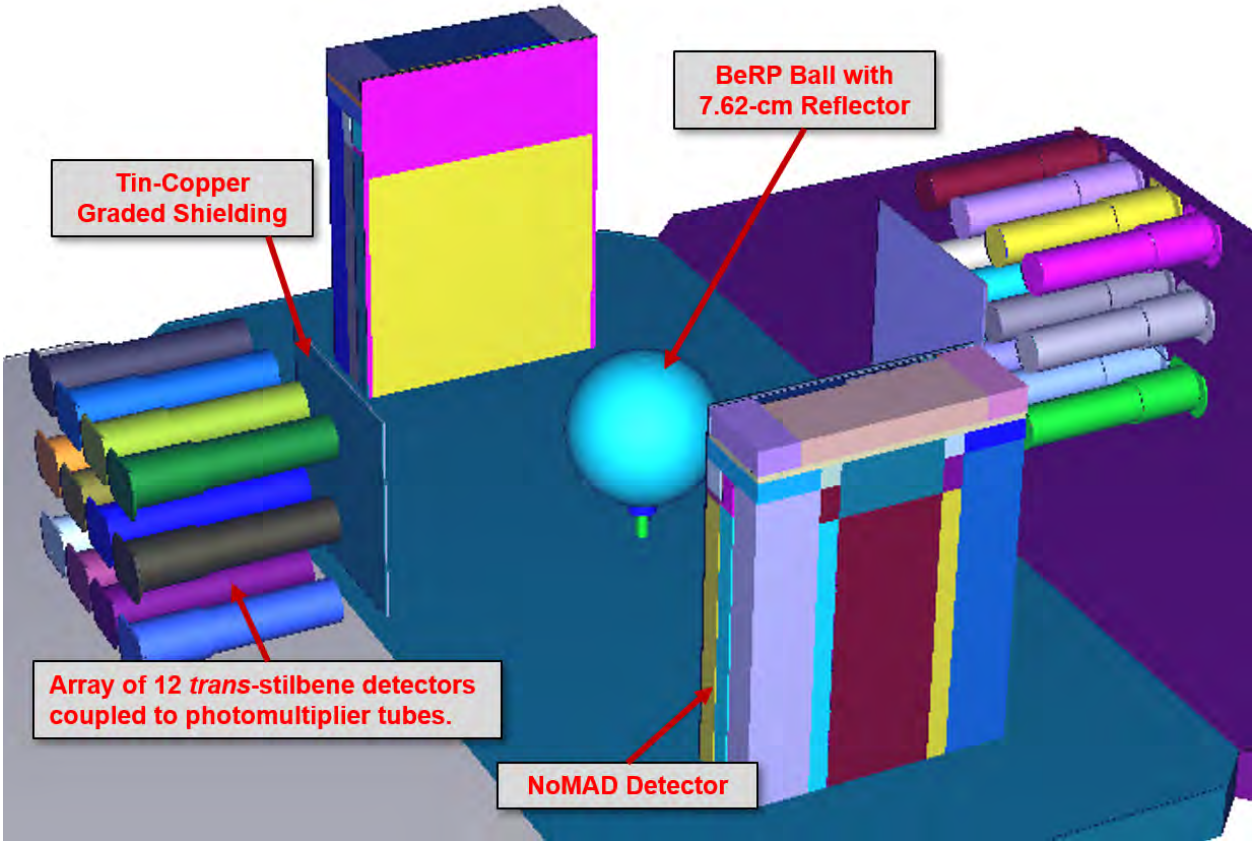

Figure 5.9: Three-dimensional rendering of the simulation geometry that emulates the photo shown in Fig. 5.2.

The KOPTS option of the KCODE subroutine was used to invoke calculation of β_{eff}. An F4 track-length tally for the fissile core cell (multiple cells were combined into a single

cell) weighted by inverse velocity and separately configured to calculate total progeny is used in a fixed-source calculation (SDEF subroutine) to estimate τ_c. A simulated value of α is calculated using the three simulated values, and a quasi-measured value of k_{eff} is calculated using the measured α and simulated β_{eff} and τ_c.

5.3 Validation of the Two-Region Rossi-alpha Theory

The simulated reference values and measured values for the prompt neutron period for the copper-reflected plutonium assemblies are tabulated in Tab. 5.2. Table 5.2 also includes a column for the number of standard deviations for the means to overlap. The tabulated data are plotted in Fig. 5.10, and the table and figure are reproduced for k_{eff} instead of α in Tab. 5.3 and Fig. 5.11; however, the comparative column for k_{eff} shows relative error. The agreement between measurement and reference simulation improves as k_{eff} approaches unity; the trend is expected since the point kinetics models assume $k_{\text{eff}} \approx 1$. The measured and reference α values agree within one standard deviation for k_{eff} values above 0.9; similarly, the k_{eff} values agree in less than 5% error for k_{eff} values greater than 0.8831.

Table 5.2: Tabulated plutonium prompt neutron lifetime estimates $-\alpha^{-1}$ from measurement and reference values from simulation for validation.

Copper Thickness [cm]	Simulated [ns]		Measured [ns]		σ-Separation
	$-\alpha^{-1}$	$\sigma_{-\alpha^{-1}}$	$-\alpha^{-1}$	$\sigma_{-\alpha^{-1}}$	
1.27	7.6	0.2	13.4	1.0	4.91
2.54	12.5	0.4	19.5	1.0	4.97
3.81	17.9	0.9	27.6	4.0	1.99
5.08	25.0	2.3	32.1	4.9	1.00
6.35	33.7	3.5	40.8	7.4	0.65
7.62	40.5	6.2	43.6	5.1	0.28
8.89	60.7	4.8	68.8	3.6	0.96
10.16	73.4	8.6	75.6	4.5	0.17

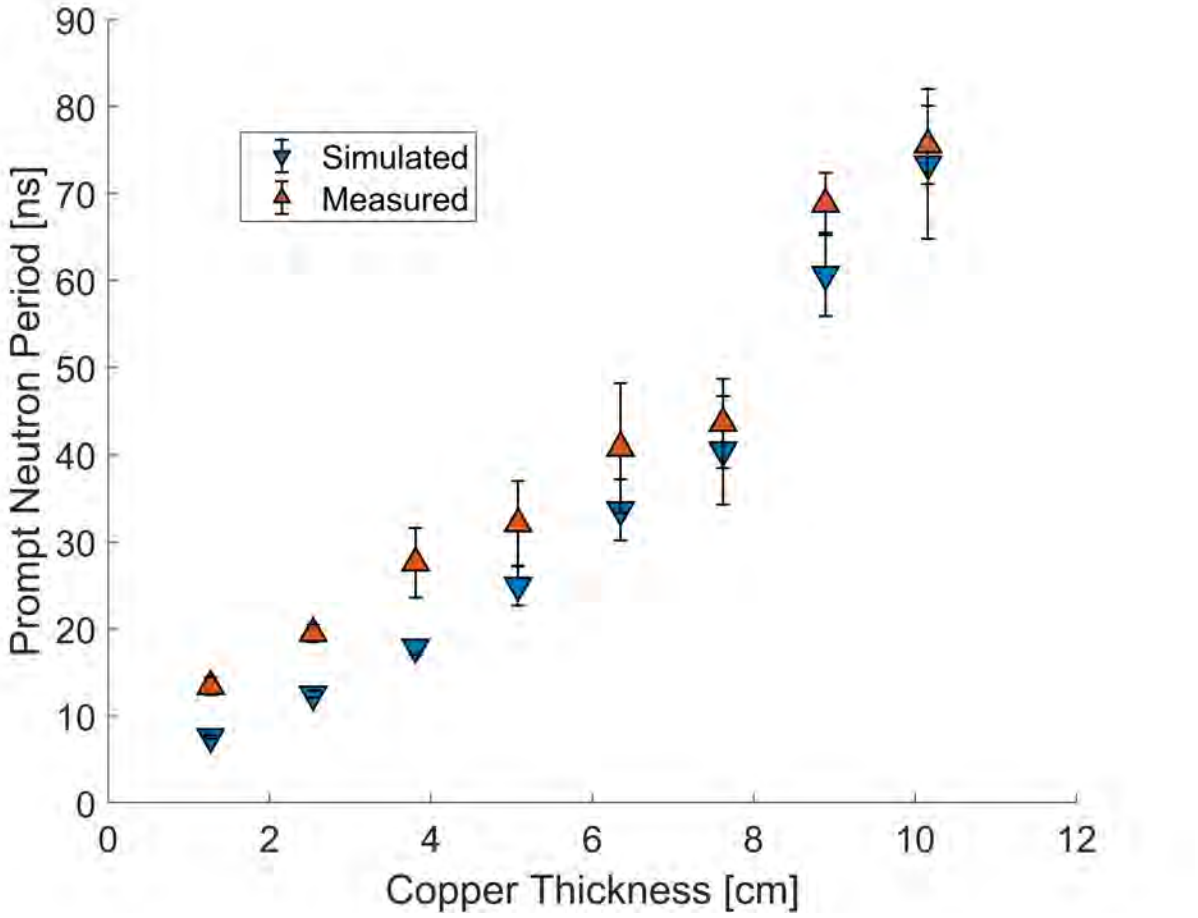

Figure 5.10: Simulated and measured prompt neutron periods for the BeRP Ball reflected by various amounts of copper.

Table 5.3: Tabulated plutonium k_{eff} estimates from measurement and reference values from simulation for validation.

Copper Thickness [cm]	Simulated		Measured		Error
	k_{eff}	$\sigma_{k_{\text{eff}}}$	k_{eff}	$\sigma_{k_{\text{eff}}}$	(M-S)/S
1.27	0.8278	0.0003	0.9045	0.0085	9.27%
2.54	0.8604	0.0003	0.9136	0.0071	6.18%
3.81	0.8831	0.0003	0.9271	0.0133	4.97%
5.08	0.9005	0.0003	0.9254	0.0168	2.77%
6.35	0.9137	0.0003	0.9309	0.0182	1.88%
7.62	0.9239	0.0003	0.9306	0.0176	0.73%
8.89	0.9322	0.0003	0.9411	0.0070	0.95%
10.16	0.9394	0.0003	0.9415	0.0093	0.22%

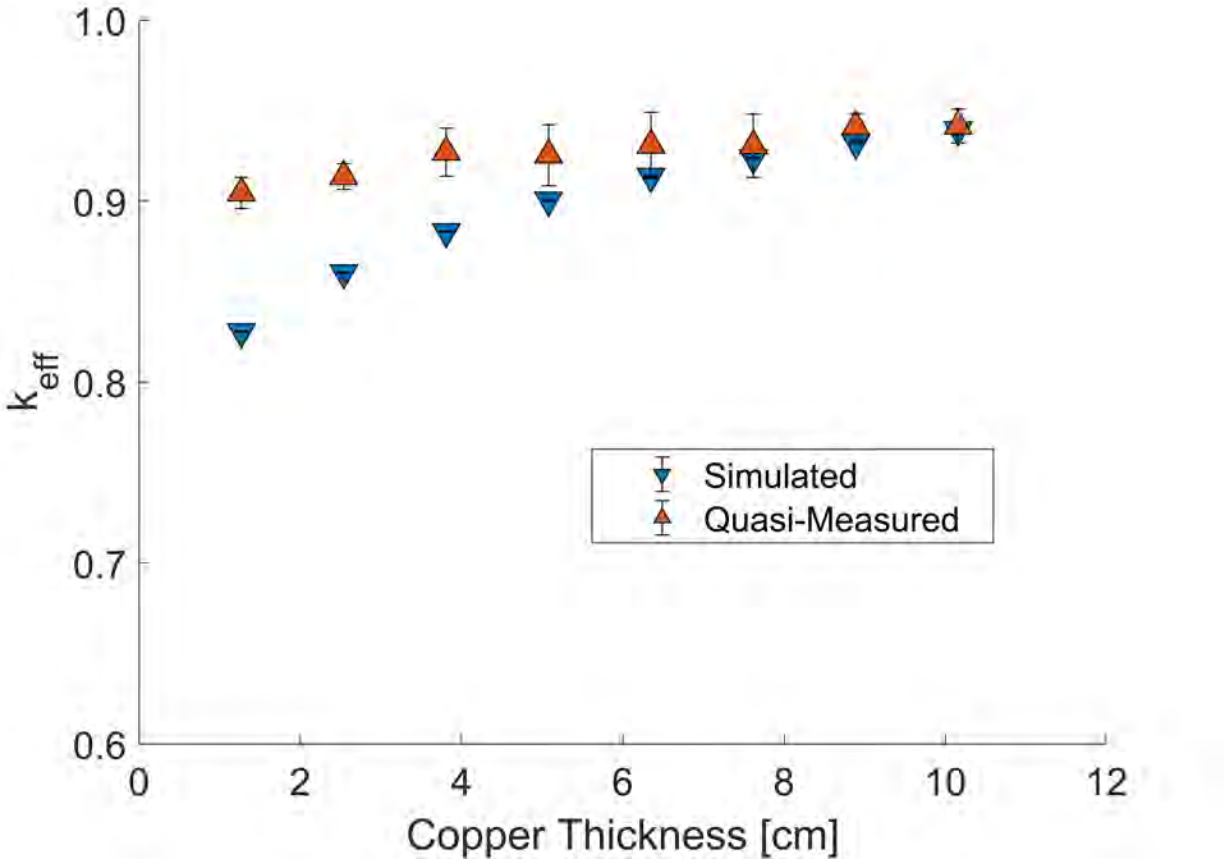

Figure 5.11: Comparison of quasi-measured k_{eff} to simulated reference values of k_{eff} for the copper-reflected plutonium measurements.

The prompt neutron period generally increases in a bare fissile core that increases k_{eff} by increasing in volume. A decreasing prompt neutron period (16.3, 13.3, 11.7 ns) as k_{eff} increased (0.7325, 0.9087, 0.9508) due to increased amounts of HDPE reflector (0.00, 3.81, 6.35 cm) was observed when analyzing the uranium data of this work. The trend was investigated by simulating the measured assemblies in MCNPX-PoliMi, observing the volumetric density of induced fission, and simulating track lengths/mean core lifetimes, which are summarized in Fig. 5.12. Photos of the assemblies are shown in Figs. 5.12a, 5.12b, and 5.12c; area-normalized heat maps of induced-fission density are shown in Figs. 5.12d, 5.12e, and 5.12f; and volume-normalized heat maps of induced-fission density are shown in Figs. 5.12g, 5.12h, and 5.12i. The area-normalized plots project the y-dimension data onto the x-z plane via

summing, thus the void in the center of the assembly is visible. As the HDPE thickness and k_{eff} values increase from Fig. 5.12d-5.12f, the bulk of induced fissions move from the center towards the cusp of the shell. The same transition is shown in the volume-normalized plots, which include annotations for τ_c and the mean track length in the core, λ_c, that decrease with increasing HDPE and k_{eff}. The trend is due to increased moderation of neutrons in the reflector (outside of the core) and, despite the neutrons being slower, ultimately shorter lifetimes in the core after reentry since the probability of induced fission significantly increases for moderated neutrons. The reducing prompt neutron period is therein verified. Furthermore, the reduction shows that increasingly thermal assemblies have faster core lifetimes and prompt neutron periods.

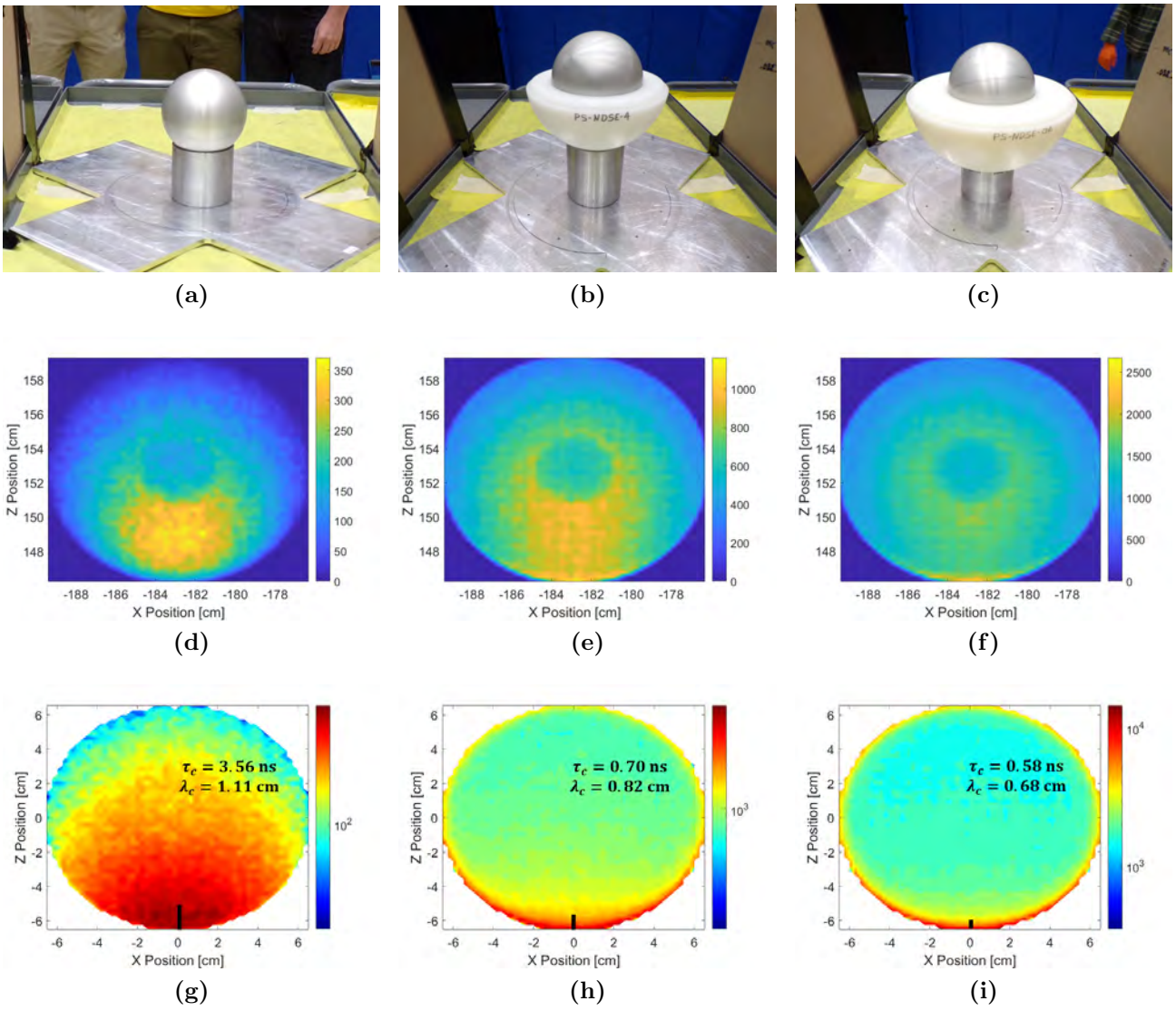

Figure 5.12: Photos of the aluminum-encased Rocky Flats shells (5.12a) bare, (5.12b) reflected by 3.81 cm of HDPE, and (5.12c) by 6.35 cm of HDPE; the other half of the reflector shells are affixed during measurement. The heat maps in the second and third row show the density of induced fission locations per area and per volume, respectively. Subfigs. (5.12d and 5.12g) correspond to the bare configuration, (5.12e and 5.12h) to the 3.81-cm-reflected configuration, and (5.12f and 5.12i) to the 6.35-cm-reflected configuration.

The verified prompt neutron periods, simulated effective delayed neutron fractions β_{eff}, and simulated prompt neutron lifetimes in the core τ_c were used to calculate quasi-measured k_{eff} values. The measured values of α were validated by comparing the quasi-measured k_{eff} to simulated reference values of k_{eff}, shown in Fig. 5.13 and tabulated in Tab. 5.4 with relative

error. The relative error is again shown to decrease as k_{eff} tends to unity.

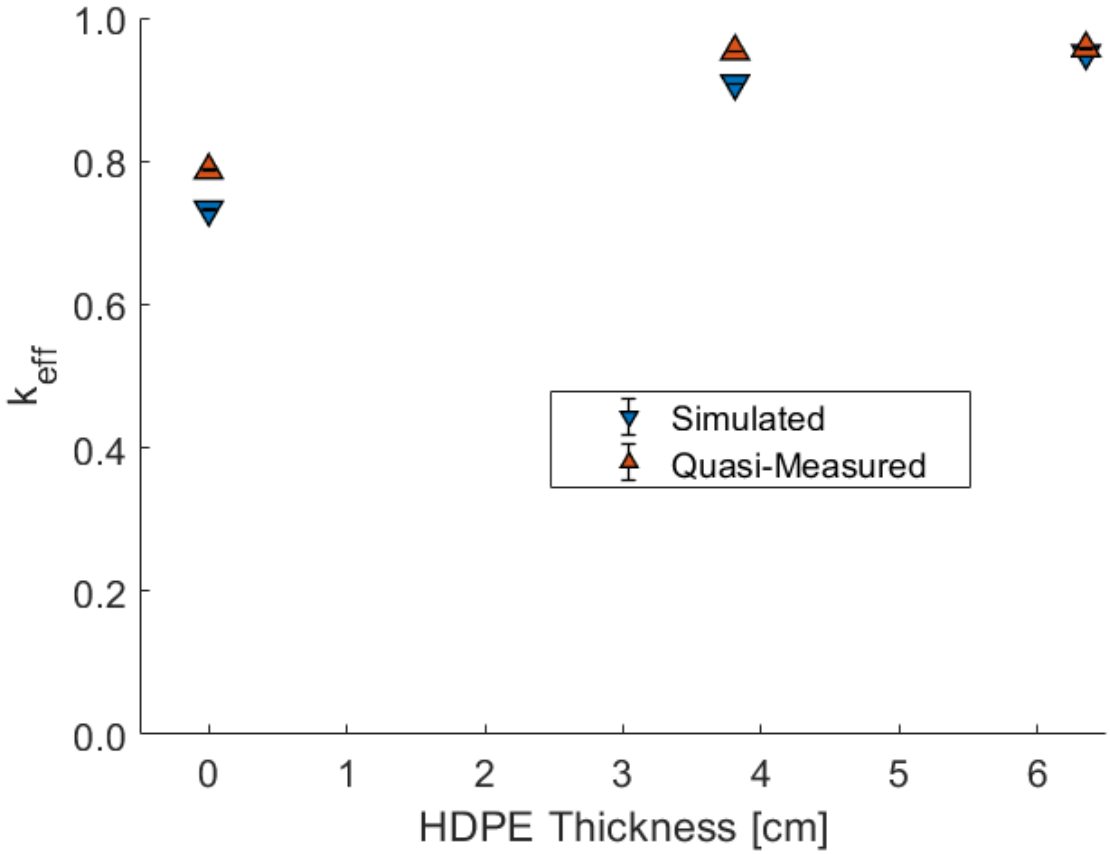

Figure 5.13: Comparison of quasi-measured k_{eff} to simulated reference values of k_{eff} for the HDPE-reflected HEU measurements.

Table 5.4: Tabulated uranium k_{eff} estimates from measurement and reference values from simulation for validation.

HDPE Thickness [cm]	Simulated		Measured		Error
	k_{eff}	$\sigma_{k_{\text{eff}}}$	k_{eff}	$\sigma_{k_{\text{eff}}}$	(M-S)/S
0.00	0.7325	0.0002	0.7947	0.0066	8.49%
3.81	0.9087	0.0004	0.9580	0.0018	5.43%
6.35	0.9508	0.0004	0.9603	0.0043	0.99%

5.4 Additional Signatures of Validated Two-Region Model

The two-region point kinetics model resulting in the two-exponential fits presents new measurable parameters, including the exponent-weighting parameter R. The purpose of this section is to study R with simulations of a moderated uranium assembly with MCNP6.2 [50] and MCNPX-PoliMi [52]. The simulated uranium assemblies are made from alternating spherical-shell layers of HEU (pure ^{235}U) and HDPE (0.97 g/cm^3) with an air-filled 2.25-cm sphere in the center. The total thicknesses of HEU and HDPE are 4.25 cm and 4.00 cm, respectively, and the HEU is always interior to the HDPE for a given layer. The configurations are designed to maintain a k_{eff} of 0.95 and vary the amount of reflection by increasing the number of alternating layers, N. The value of N is varied from 1 to 60 in addition to a homogeneous case ($N \to \infty$), and a constant k_{eff} is maintained by changing the HEU density (the HDPE density as well in the homogeneous case). Two-dimensional renderings of the simulation geometry for $N = 1, 2, \ldots, 5$ are shown in Fig. 5.14 and k_{eff} and density values are tabulated in Tab. 5.5. Fission chains were driven by an exterior, inward-facing, spherical-surface ^{252}Cf source.

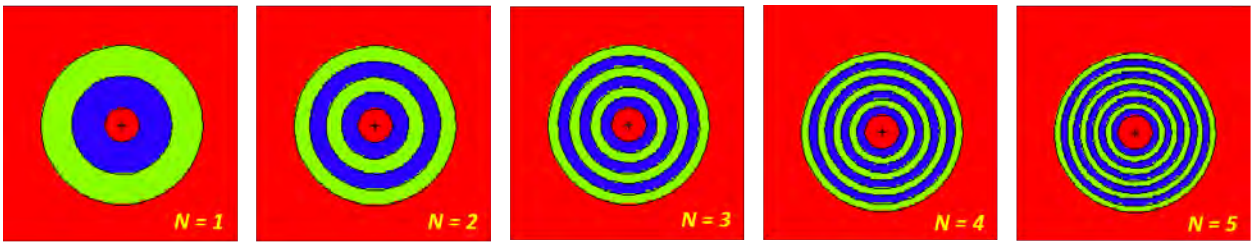

Figure 5.14: Two-dimensional rendering of sample geometries for the simulation study where N indicates the number of repeated HEU-HDPE layers. The blue layers are HEU and the green layers are HDPE.

Table 5.5: Approach-to-homogeneity simulation specifications and results. Densities are for the HEU regions only (HDPE density is fixed at 0.97 g/cm^3) except for the homogeneous case where there is one ^{235}U atom per CH_2. Values for $< E_n >$ are the mean neutron energy inducing fissions.

N	k_{eff}	$\sigma_{k_{\text{eff}}}$	HEU Density [g/cm^3]	R	$\langle E_n \rangle$ [MeV]
1	0.9496	0.0005	19.10	0.05	1.11
2	0.9497	0.0005	17.00	0.07	0.90
3	0.9499	0.0005	16.60	0.07	0.85
4	0.9499	0.0005	16.50	0.10	0.82
5	0.9489	0.0005	16.48	0.13	0.81
7	0.9497	0.0006	16.50	0.18	0.80
11	0.9501	0.0005	16.52	0.24	0.79
15	0.9500	0.0005	16.53	0.27	0.79
20	0.9496	0.0005	16.54	0.29	0.79
25	0.9497	0.0004	16.56	0.32	0.79
30	0.9495	0.0005	16.57	0.32	0.78
40	0.9494	0.0005	16.58	0.33	0.78
50	0.9502	0.0005	16.60	0.35	0.78
60	0.9501	0.0005	16.60	0.36	0.78
∞	0.9499	0.0006	8.75	0.39	0.75

In Eq. (4.9), R balances the two exponents of the fit to calculate α. As R approaches 0.5, the two-region model is more important; thus, between similar configurations, R could be an indicator of the type and amount of reflection for like assemblies. In the approach to homogeneity, the amount of reflection increases to maintain the same k_{eff}. A Rossi-alpha histogram was constructed for each N and treated with the two-exponential analysis to calculate R. The value of R as a function of the number of layers in the simulated assembly is shown in Fig. 5.15. Note that the order of the exponents can be switched such that R is always less than 0.5. The values of R asymptotically increase with the amount of reflection, approaching $R = 0.39$.

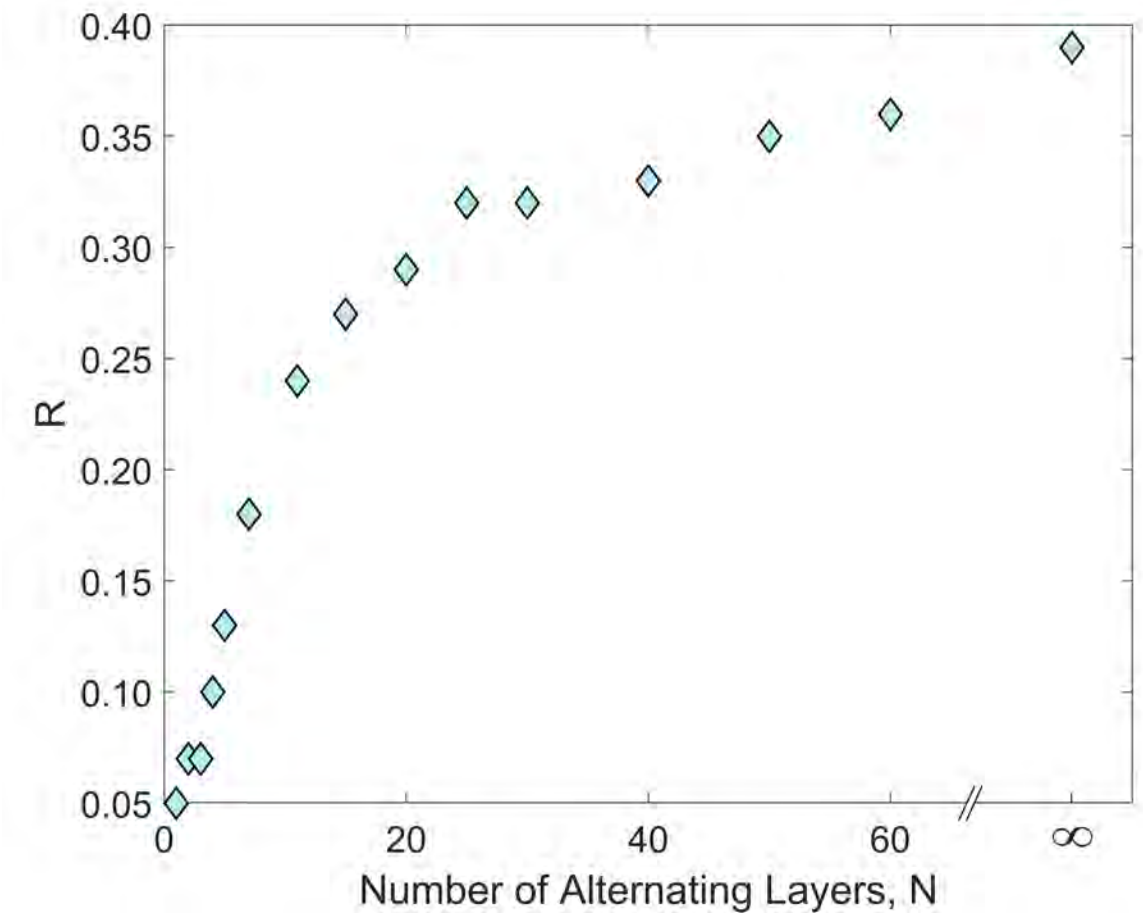

Figure 5.15: R parameter as a function of N, the number of alternating layers.

5.5 Validation of the Quantification and Propagation of Rossi-alpha Measurement Uncertainty

5.5.1 Validation of the bin-by-bn analytic uncertainty quantification

For a normal distribution, 68.3% and 99.7% of data are expected to fall within the 1- and 3-σ confidence intervals, respectively. Such confidence intervals were calculated using the sample variance method (20 estimates corresponding to independent 1-minute measurements) for the copper-reflected organic scintillator data, shown in Fig. 5.16; 67.2% and 99.8% of data were respectively contained within the 1- and 3-σ confidence intervals, verifying the sample variance method for bin-by-bin error bars.

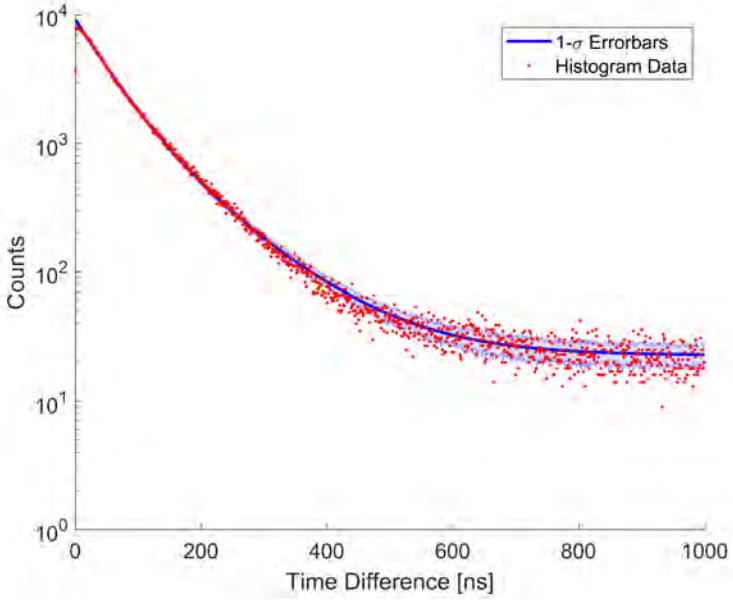

(a)

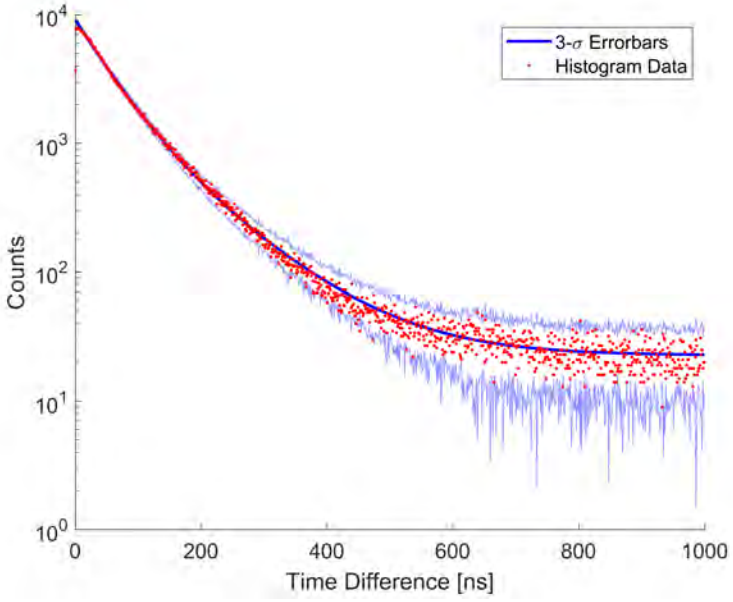

(b)

Figure 5.16: Rossi-alpha histograms for the organic scintillator measurement of the copper-reflected plutonium with error bars calculated from the sample variance method. The solid, blue line through the center of the red data points is the mean histogram value of the 20 measurements, and the blue region about the center line represent one or three standard deviation error bars. Fig. 5.16a shows one standard deviation error bars, whereas Fig. 5.16b shows three.

The analytic bin-by-bin error bars are validated by comparison to those of the sample

variance method. The relative uncertainties from both methods are shown in Fig. 5.17 for both detection systems, using the copper-reflected data for organic scintillators (every 20 data points) and copper- and polyethylene-reflected data for ^{3}He. The analytic error bars overlap the sample method error bars for the organic scintillators and overestimate the relative uncertainty. Even better agreement is shown in the ^{3}He data and the analytic method again estimates relative uncertainties greater than the center of the sample error bars. Note that the overestimation increases for larger time differences; the trend could be due to accidental counts contributing more uncertainty than the correlated counts are, though further investigation is the subject of future work. Further note that analytic error bars are less noisy than those of the sample method and that relative uncertainty scales as (measurement time)$^{-1/2}$, as shown in Fig. 5.18. If there was greater noise, the shape of relative uncertainty in time would include an additional $+B$ term to account for asymptotic noise limits. The relative uncertainties in the ^{3}He data are much lower than those of the organic scintillator data; the ^{3}He system had double the measurement time and an efficiency 10-100 times greater than that of the organic scintillator system. Precise efficiency ratios are not available because the organic scintillator system did not measure the heterogeneous assembly.

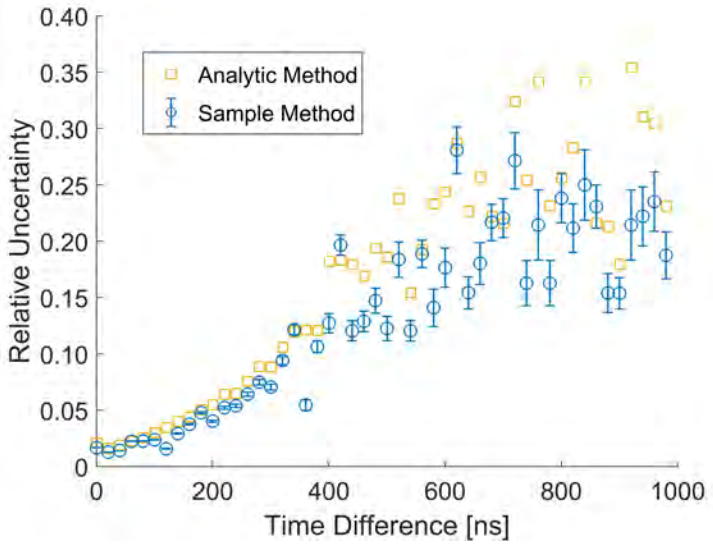

(a)

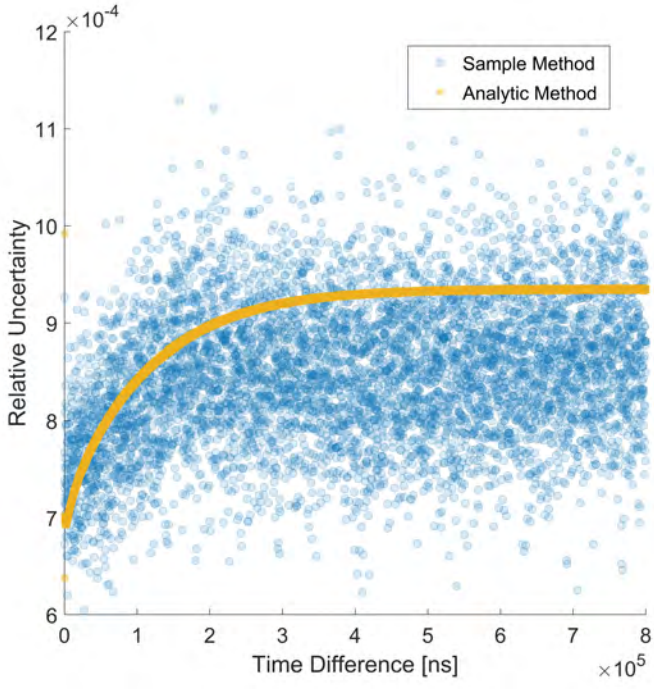

(b)

Figure 5.17: Direct comparisons of bin-by-bin relative uncertainty estimates between the sample variance and analytic methods for the (a) organic scintillator system measuring the copper-reflected BeRP Ball and (b) ^{3}He system measuring the copper-and-polyethylene-reflected BeRP Ball.

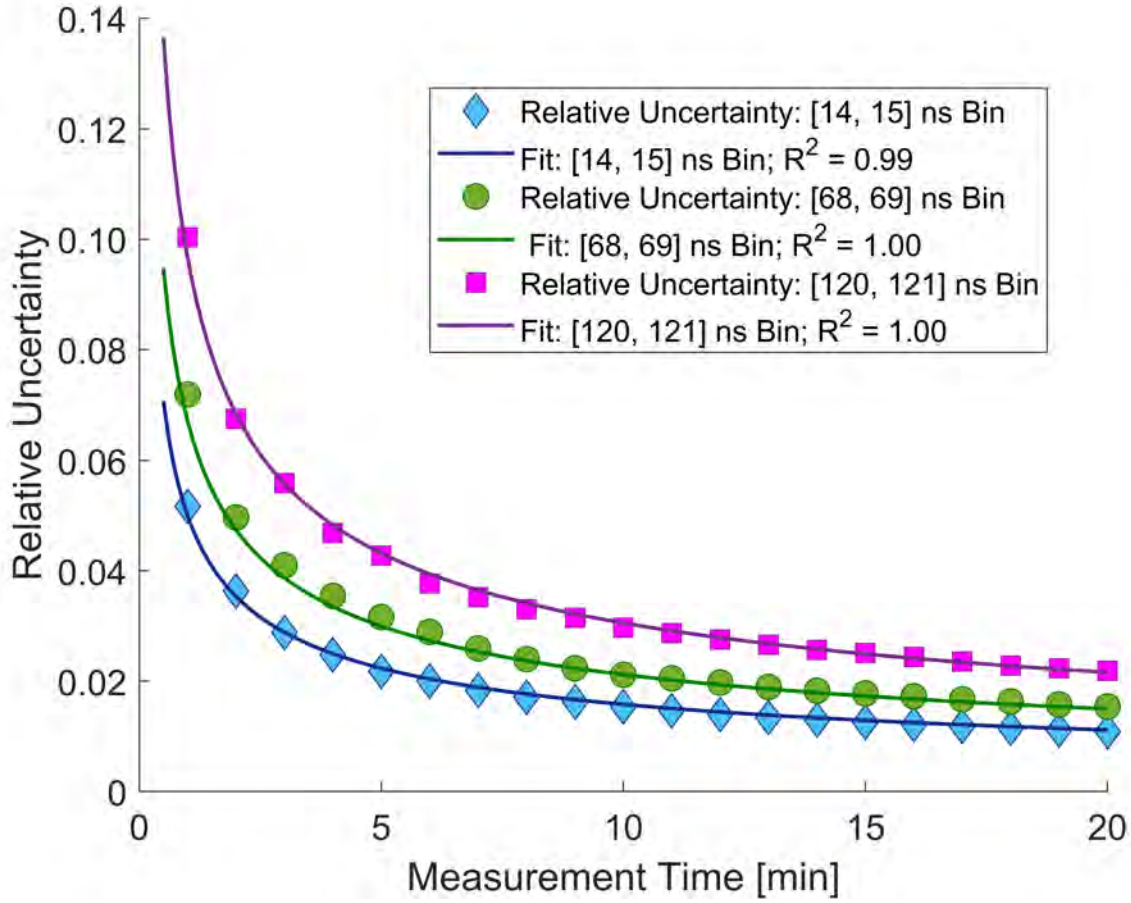

Figure 5.18: Relative uncertainty as a function of measurement time in three bins, $y = Ax^{-.5}$ fits for each data series, and R^2 values for the fits for the organic scintillator measurement of the copper-reflected BeRP Ball.

5.5.2 Validation of Uncertainty Propagation

Weights are calculated such that uncertainty from the histograms can be propagated to the estimate of α and such that the fitting is more accurate. Weights for the organic scintillator measurements of the copper-reflected BeRP Ball are shown in Fig. 5.19. If the weights are noisy, a fit of the weights can be used instead. A sample fit is also shown in Fig. 5.19. Fig. 5.20 shows the improvement in accuracy due to weighting; note that this work chooses to take the simulated values of the prompt period from Ref. [3] as the reference value.

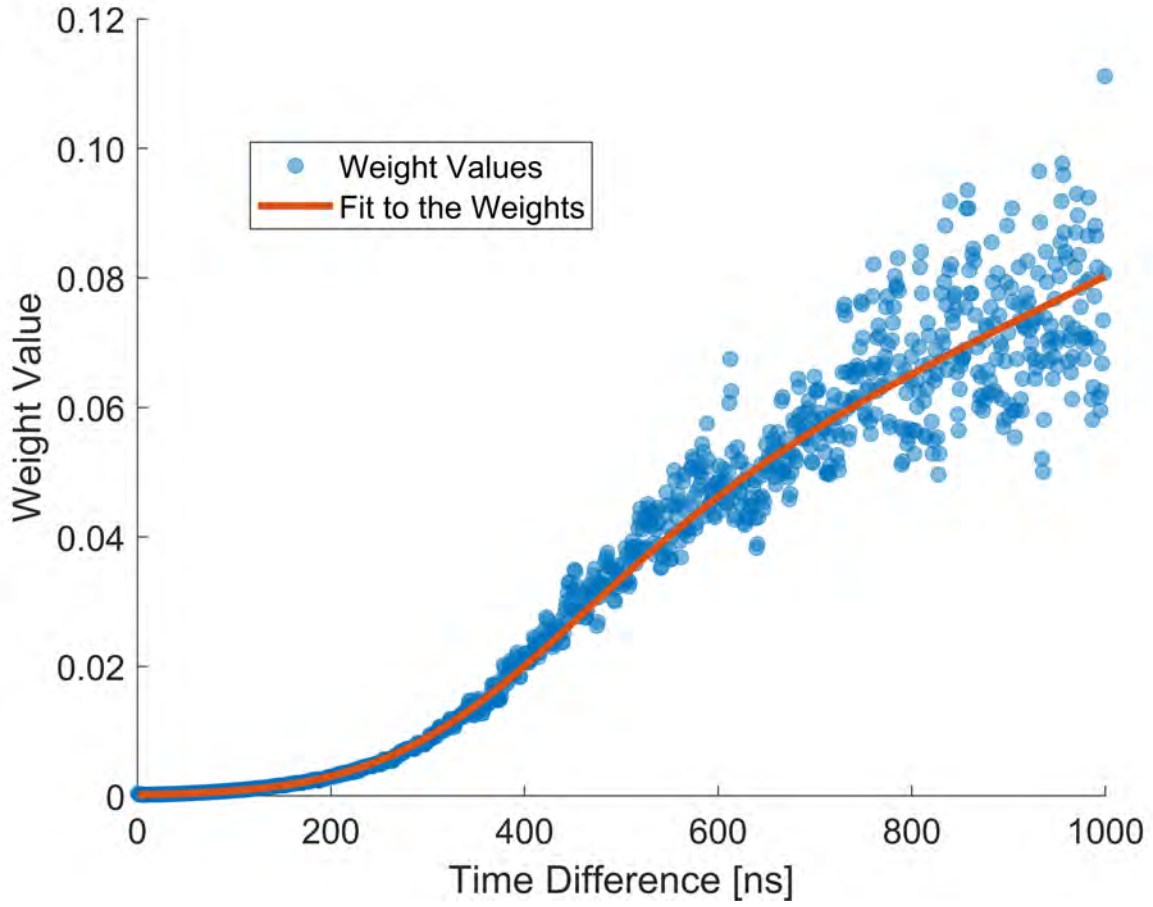

Figure 5.19: Sample weights with a fit for the organic scintillator measurement of the copper-reflected BeRP Ball.

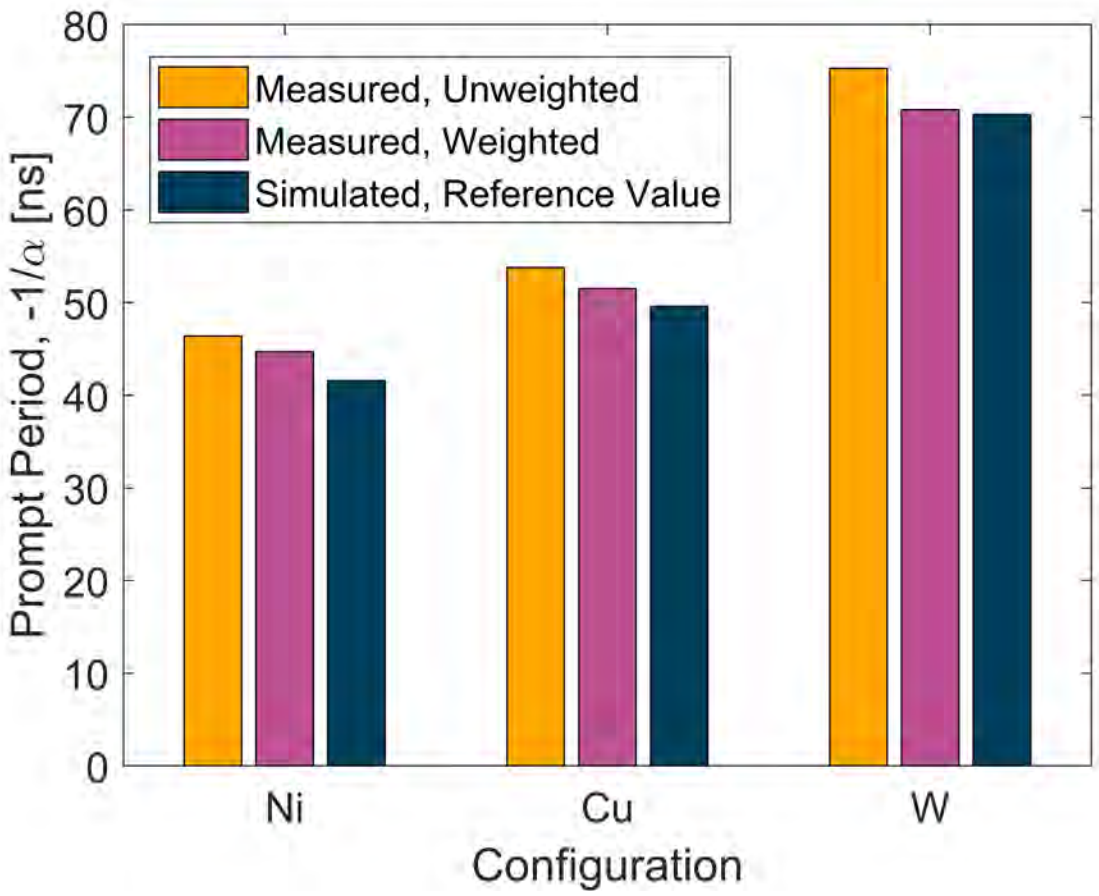

Figure 5.20: Estimates of the prompt period with unweighted and weighted fits, and the simulated reference value.

The analytic error bars were used to construct weights, weighted fits were applied to the organic scintillator data, and uncertainty was propagated from the fit parameters to obtain an analytic standard deviation on the estimate of the prompt period, $1/\alpha$. A sample standard deviation of the prompt period is also obtained by taking the standard deviation of the prompt periods calculated from 20 one-minute measurements for the copper case, and 30 one-minute measurements for the tungsten and nickel cases. The two methods are compared in Fig. 5.21 and agree within one standard deviation.

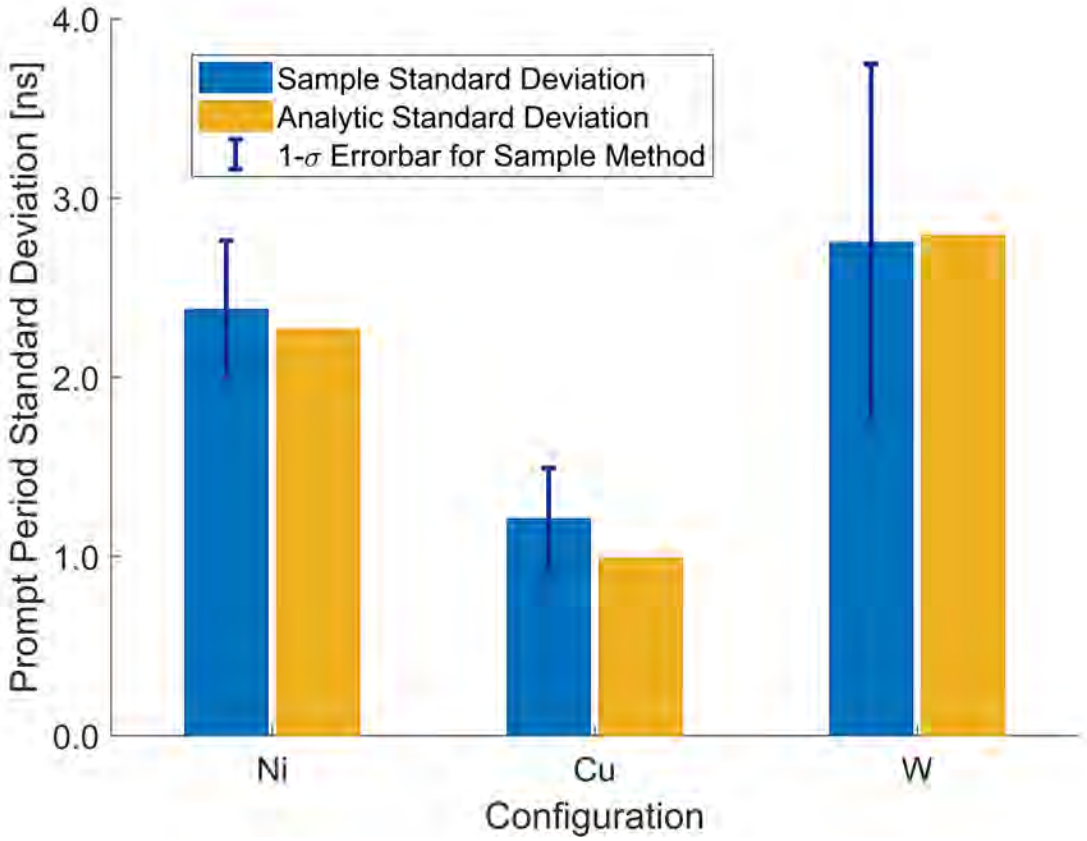

Figure 5.21: Standard deviations of the prompt-period estimates obtained from the sample variance and analytic methods.

5.6 Summary, Conclusion, and Future Work

The two-exponential probability density function for Rossi-alpha experiments on reflected assemblies from two-region point kinetics is validated with organic scintillator measurements of copper-reflected plutonium and HDPE-reflected uranium. The agreement between measurement and simulation, which is used as the reference in this work, improves as k_{eff} approaches unity and is notably good above $k_{\text{eff}} = 0.9$. The trend in agreement for large k_{eff} is expected since point kinetics assumes $k_{\text{eff}} \approx 1$. The disagreement for small k_{eff} is also observed when directly comparing the prompt neutron periods, which is again expected. It is preferential to use the Rossi-alpha method when evaluating near- or delayed-critical assemblies and methods such as neutron multiplicity counting or the Feynman-Y method

for deeply subcritical assemblies. The transition between methods is the subject of future work and the upcoming Measurement of Uranium Subcritical and Critical (MUSiC) benchmark [86, 87]. The transition between Rossi-alpha and Feynman-alpha are preliminarily investigated for reflected assemblies in Chapter VI.

Helium-3 detectors utilizing moderation cannot be used for two-region Rossi-alpha measurements unless the prompt neutron period of the core is larger than tens of microseconds and these large times cannot be achieved by making a system more thermal; the results show that increasingly thermal assemblies have shorter prompt neutron periods. Sufficiently large prompt neutron periods may occur for high k_{eff} multiplication factors; however, depending on the assembly, the associated large neutron fluxes may oversaturate and otherwise disqualify ^{3}He detectors. Future work will compare ^{3}He and organic scintillator systems for assemblies between delayed- and prompt-critical.

The mean neutron generation time Λ is traditionally used to infer k_{eff} in the one-region model. In the two-region model, either Λ of the core must be simulated (currently only Λ of the composite assembly is available in standard tools) to be paired with α of the core, α of the composite assembly must be measured (currently unavailable) to be used with the standard composite Λ, or the simulation of the mean neutron lifetime in the core τ_c approach of this work must be used. An experimentalist approach to measure a composite α may be to introduce a time constant (such as slowing down time) to the detection process (that does not affect the time correlations or behavior of the assembly) that is larger than both α and τ_r for detected neutrons. The data would then be treated with the two-exponential analysis and the smaller time constant that is calculated would correspond to the composite α. If assembly-decoupled moderator is added around the detectors for this approach, organic scintillators could not be used due to practical limits on detection threshold and the use of ^{3}He detectors may be preferential. This experimental approach is a hypothesis only and the subject of future feasibility tests.

A simulation study was performed to evaluate a newly available weighting parameter,

R, that varies between zero and one. It was shown that R gets closer to 0.5 as reflection increases. The correlated behavior indicates that R could be used as a signature to infer reflector properties such as type and amount for similar assemblies. The value of R cannot necessarily be compared between substantially different assemblies since R is biased by the detected neutrons.

The analytic method for estimating bin-by-bin histogram uncertainty is validated by comparison to the sample variance method. Note that the analytic estimate of the uncertainty is less noisy and more stable than that of the sample variance method. Therefore, it may be preferential to use the analytic method when long, redundant measurements are infeasible and hence when the sample variance method is unreliable. In general, reducing the number of repeated measurements will reduce procedural and operational costs.

The validation is shown for both an organic scintillation detector-based system and a ^{3}He-based system, demonstrating that the analytic method is detection-system-agnostic. The histogram error bars are propagated to the uncertainty in the fit parameters by weighting the fit. In addition to correctly propagating uncertainty, weighting the fit improves the accuracy of prompt neutron decay constant estimates. Thus, fit algorithms should be weighted.

CHAPTER VI

Theory of Feynman-alpha Measurements and Validation for New Theory

The work in this chapter comes from my work titled "On the Feynman-alpha method for reflected fissile assemblies" published in Annals of Nuclear Energy (accepted for publication on 11 December 2020) [88].

6.1 Introduction

The Feynman-alpha method utilizes time correlations between neutron detections to estimate the prompt neutron period of fissile assemblies [22, 23, 24, 18]. The prompt neutron period is itself interesting in the context of applications and it is also used to infer derivative values such as the k_{eff} multiplication factor.

The Feynman-alpha method was originally developed for bare cores of fissile material and shortcomings in adequacy have been identified when reflectors are introduced [29]. Therefore, it is desirable to extend the traditional one-region point kinetic models to two-region point kinetics to account for the region introduced by reflector, which has been addressed in greater generality by existing literature [30, 89]. This work simplifies the equations and follows a different derivation based on the double integration of the Rossi-alpha method [90, 91]. The Rossi-alpha-integration approach is selected to utilize recent two-region point kinetic

generalizations to the Rossi-alpha equations [72], which have been validated [6].

Beyond the derivation, this work develops rigorous first-order propagation of measurement uncertainty similar to Refs. [73, 92]. The propagation involves weighting a fit to the Feynman histogram data, which results in a more accurate fit that adequately incorporates measurement uncertainty with fit uncertainty to estimate a composite uncertainty in the fit parameters. The prompt neutron period is a function of the fit parameters in the two-region model (whereas it is a fit parameter in the one-region model), thus the uncertainty in fit parameters is propagated to a final estimate of the prompt neutron period. Two methods of determining the uncertainty in the Feynman histogram data, analytic and sample methods, are presented.

The theory is validated with experimental data and simulations to determine reference values. An organic scintillator array (OSCAR) is used to measure a 4.5-kg sphere of weapons-grade, alpha-phase plutonium reflected by various amounts of copper to attain different levels of reflection and multiplication. Additionally, the one- and two-region estimates of the prompt neutron period are compared.

The structure of this chapter is as follows. The derivation of the two-region Feynman-alpha theory based on the double integration of the Rossi-alpha equations is presented in Sec. 6.2. Associated uncertainty propagation is discussed in Sec. 6.3, the experimental setups are shown in Sec. 6.4, and the analysis of data is discussed in Sec. 6.5. Results are presented in Sec. 6.6 and subsequent conclusions are made in Sec. 6.7.

6.2 Feynman-alpha Method

The number of neutron counts c in a given window τ (note that τ here is a time window and not a physical lifetime associated with the assembly) deviates from a Poisson random variable due to multiplication/fluctuations in the prompt neutron population [22, 23, 24, 19]. The deviation is used as a signature to estimate the prompt neutron decay constant α; the

signature Y is called "excess variance" and is related to c by

$$Y = \frac{\text{variance}}{\text{mean}} - 1 = \frac{\langle c^2 \rangle - \langle c \rangle^2}{\langle c \rangle} - 1, \tag{6.1}$$

where $\langle c^2 \rangle$ is the second moment of the counting distribution for a given window τ. In the one-region point kinetics model, Y is related to α by

$$Y = \gamma \left(1 - \frac{1 - e^{-\alpha\tau}}{\alpha\tau} \right), \tag{6.2}$$

where γ is a scaling constant and both γ and α are determined by fitting Y as a function of τ. The probability density function for the two-region Rossi-alpha distribution in Eqn. (4.25) can be integrated twice and algebraically manipulated [90, 89, 91] to obtain the two-region point kinetics model. Note that other methods of derivation exist in greater generality [30]. The double integration is related to c by

$$\frac{\langle c^2 \rangle - \langle c \rangle}{2} = \int_0^\tau dt_2 \int_0^{t2} dt_1 p_{\mathrm{R}}(t_2 - t_1), \tag{6.3}$$

where $\tau = t_2 - t_1$. Performing the integrations results in

$$\frac{\langle c^2 \rangle - \langle c \rangle}{2} = \frac{{F_0}^2 \epsilon^2 \tau^2}{2} - B' F_0 \epsilon^2 \tau \left(\frac{\rho_1}{r_1} \left(1 + \frac{1 - e^{r_1\tau}}{r_1\tau} \right) + \frac{\rho_2}{r_2} \left(1 + \frac{1 - e^{r_2\tau}}{r_2\tau} \right) \right), \tag{6.4}$$

where B' is treated as an arbitrary constant. Noting that $\langle c \rangle = F_0 \epsilon \tau$, multiplying both sides of the equation by $2/\langle c \rangle$, and rearranging terms further results in

$$Y = \frac{\langle c^2 \rangle - \langle c \rangle^2}{\langle c \rangle} - 1 = -B' \epsilon \left(\frac{\rho_1}{r_1} \left(1 + \frac{1 - e^{r_1\tau}}{r_1\tau} \right) + \frac{\rho_2}{r_2} \left(1 + \frac{1 - e^{r_2\tau}}{r_2\tau} \right) \right). \tag{6.5}$$

The equation can be condensed into

$$Y = \gamma_1 \left(1 + \frac{1 - e^{r_1\tau}}{r_1\tau} \right) + \gamma_2 \left(1 + \frac{1 - e^{r_2\tau}}{r_2\tau} \right) \tag{6.6a}$$

for practical fitting applications, where

$$\gamma_1 = -B'' \frac{\rho_1}{r_1} \tag{6.6b}$$

$$\gamma_2 = -B'' \frac{\rho_2}{r_2} \tag{6.6c}$$

such that there are only four fit parameters: γ_1, γ_2, r_1, and r_2. Note that B'' absorbs the efficiency variable to define a new arbitrary constant. The value of R is calculated by taking the ratio of γ_1 and γ_2; the ratio eliminates B'' and results in an equation relating numeric values, R, r_1, and r_2. Since r_1 and r_2 are known from the fit, R may be calculated. Then, the numeric values for R, r_1, and r_2 are used to calculate α by Eqn. (4.9). Hence, using Eqns. (4.27a), (4.9), and (6.6), α is expressed in terms of the fit parameters as:

$$\alpha = (r_1 + r_2) + r_1 r_2 \sqrt{\frac{\gamma_1 + \gamma_2}{\gamma_1 {r_1}^2 + \gamma_2 {r_2}^2}}. \tag{6.7}$$

6.2.1 In Terms of Factorial Moments

Equation (6.6) can be applied to the Y_2 parameter, which in turn can be expressed in terms of factorial counting moments by [93, 94]

$$Y_2(\tau) = \frac{1}{2} \frac{m_1(\tau)}{\tau} Y(\tau) = \frac{1}{\tau} \left(m_2(\tau) - \frac{1}{2} {m_1}^2(\tau) \right). \tag{6.8}$$

The factorial moments m_2 and m_1 are calculated as a function of τ from list mode data (a sorted list of neutron detection times) and the random gate generation technique is used in this work [93]. Mathematically,

$$m_\mu(\tau) \approx \sum_{x=\mu}^{\infty} \binom{x}{\mu} {b_x}^+(\tau), \tag{6.9}$$

where

$${b_x}^+(\tau) = \frac{B_x(\tau)}{K} \tag{6.10}$$

and $B_x(\tau)$ is, after looking in K inspection windows, the number of windows containing exactly x neutron detections. A histogram is constructed by calculating Y_2 as a function of τ (and α is determined from a fit of this histogram).

6.3 Propagation of Measurement Uncertainty

Rigorous quantification of measurement uncertainty for the Feynman-alpha method that propagates histogram uncertainty (uncertainty in Y_2) through the fitting algorithm to α is needed. Furthermore, whereas α is a fit parameter in the one-region model, it is a function of the fit parameters in the two-region model. Therefore, uncertainty must be propagated from the fit parameters to the final estimate of α. Subsection 6.3.1 presents two methodologies for estimating histogram uncertainty, subsec. 6.3.2 describes the process for propagating histogram and fit uncertainty to the fit parameters, and subsec. 6.3.3 propagates uncertainty from the fit parameters to the final estimate of α. The collective process is adapted from Refs. [73, 92].

6.3.1 Uncertainty in the Feynman Histogram

The first method of determining histogram uncertainty, called the sample method, divides a total measurement into multiple smaller measurements, calculates a histogram for each submeasurement, and then calculates the error bars by taking bin-by-bin standard deviations. The second method – an analytic approach – calculates the bin-by-bin standard deviation using up to the fourth factorial moment (see Eqn. (6.9)) and is given by [94, 95]

$$\sigma_{Y_2} = \frac{1}{\tau}\sqrt{\frac{1}{K-1}\left(6m_4 - 6m_3m_1 + 6m_3 - {m_2}^2 + 4m_2{m_1}^2 - 4m_2m_1 + m_2 - {m_1}^4 + {m_1}^3\right)}. \tag{6.11}$$

The analytic method is preferential to the sample method so long as the calculation of the fourth factorial moment is reliable and, relatedly, so long as K is sufficiently large. For a 20-minute measurement with a maximal gate width of 10 μs (for an organic scintillator system

measuring fast assemblies as in this work, for example), K is sufficiently large at 1.2×10^8 such that statistical biases are negligible. Reliability also depends on a variety of variables such as accidentals rate, detector efficiency, assembly multiplication, and measurement time; if the accidentals rate is comparable to the fourth factorial moment, the uncertainty in the latter may become unbounded.

6.3.2 Uncertainty Propagation through Fitting Algorithm to Fit Parameters

Weighting the nonlinear least-squares fit to experimental data reduces fit uncertainty, results in greater accuracy, and appropriately propagates experimental uncertainty through the fit algorithm. Inverse-variance weighting – weighting bin i by $1/{\sigma_i}^2$ – optimally reduces the uncertainty. The uncertainties in the fit parameters are given by the covariance matrix,

$$\Sigma_{\text{covar}} = [J^T W J]^{-1} = \begin{bmatrix} {\sigma_{\gamma_1}}^2 & \sigma_{\gamma_1\gamma_2} & \sigma_{\gamma_1 r_1} & \sigma_{\gamma_1 r_2} \\ \sigma_{\gamma_2\gamma_1} & {\sigma_{\gamma_2}}^2 & \sigma_{\gamma_2 r_1} & \sigma_{\gamma_2 r_2} \\ \sigma_{r_1\gamma_1} & \sigma_{r_1\gamma_2} & {\sigma_{r_1}}^2 & \sigma_{r_1 r_2} \\ \sigma_{r_2\gamma_1} & \sigma_{r_2\gamma_2} & \sigma_{r_2 r_1} & {\sigma_{r_2}}^2 \end{bmatrix}, \tag{6.12}$$

that has variances on the diagonal and covariances on the off-diagonal terms. The Jacobian matrix J is an output of the fitting algorithm and an $[N \times P]$ matrix where N is the number of histogram bins and P is the number of fit parameters ($P = 4$ when fitting with Eqn. (6.6)). The weighting matrix W is $[N \times N]$, zero on off-diagonal terms, $W_{i,i} = 1/{\sigma_i}^2$ on the diagonal, and given by

$$W = \begin{bmatrix} \frac{1}{{\sigma_1}^2} & & & \\ & \frac{1}{{\sigma_2}^2} & & \\ & & \ddots & \\ & & & \frac{1}{{\sigma_N}^2} \end{bmatrix}. \tag{6.13}$$

Note that off-diagonal covariance terms may also be included; the increased complexity and comprehensiveness, which was discussed in Ref. [35], provides an even better estimate of

uncertainty on the prompt neutron period and other calculated values. The covariance terms are omitted in this work for simplicity and thus the chi-squared normalization condition of the nonlinear least-squares fitting algorithm is equal to the degrees of freedom of the fit function.

6.3.3 Uncertainty Propagation from Fit Parameters to α

The first order uncertainty in α is determined by propagating the uncertainty in the fit parameters through Eqn. (6.7) via

$$\begin{aligned}
{\sigma_\alpha}^2 = &\left(\frac{\partial\alpha}{\partial r_1}\right)^2 {\sigma_{r_1}}^2 + \left(\frac{\partial\alpha}{\partial r_2}\right)^2 {\sigma_{r_2}}^2 + \left(\frac{\partial\alpha}{\partial\gamma_1}\right)^2 {\sigma_{\gamma_1}}^2 + \left(\frac{\partial\alpha}{\partial\gamma_2}\right)^2 {\sigma_{\gamma_2}}^2 \\
&+ 2\left(\frac{\partial\alpha}{\partial r_1}\right)\left(\frac{\partial\alpha}{\partial r_2}\right)\sigma_{r_1 r_2} + 2\left(\frac{\partial\alpha}{\partial r_1}\right)\left(\frac{\partial\alpha}{\partial\gamma_1}\right)\sigma_{r_1\gamma_1} + 2\left(\frac{\partial\alpha}{\partial r_1}\right)\left(\frac{\partial\alpha}{\partial\gamma_2}\right)\sigma_{r_1\gamma_2} \\
&+ 2\left(\frac{\partial\alpha}{\partial r_2}\right)\left(\frac{\partial\alpha}{\partial\gamma_1}\right)\sigma_{r_2\gamma_1} + 2\left(\frac{\partial\alpha}{\partial r_2}\right)\left(\frac{\partial\alpha}{\partial\gamma_2}\right)\sigma_{r_2\gamma_2} \\
&+ 2\left(\frac{\partial\alpha}{\partial\gamma_1}\right)\left(\frac{\partial\alpha}{\partial\gamma_2}\right)\sigma_{\gamma_1\gamma_2}. \qquad (6.14)
\end{aligned}$$

The partial derivatives are given by

$$\frac{\partial\alpha}{\partial\gamma_1} = \frac{\gamma_2(\gamma_1+\gamma_2)(r_1 r_2)^4({r_2}^2 - {r_1}^2)}{2\delta^3} \qquad (6.15a)$$

$$\frac{\partial\alpha}{\partial\gamma_2} = \frac{\gamma_1(\gamma_1+\gamma_2)(r_1 r_2)^4({r_1}^2 - {r_2}^2)}{2\delta^3} \qquad (6.15b)$$

$$\frac{\partial\alpha}{\partial r_1} = \frac{(\gamma_1+\gamma_2)(r_1 r_2)^2(\gamma_2 {r_2}^4 r_1(\gamma_1+\gamma_2) + \delta(\gamma_1 {r_1}^2 + \gamma_2 {r_2}^2))}{\delta^3} \qquad (6.15c)$$

$$\frac{\partial\alpha}{\partial r_2} = \frac{(\gamma_1+\gamma_2)(r_1 r_2)^2(\gamma_1 {r_1}^4 r_2(\gamma_1+\gamma_2) + \delta(\gamma_1 {r_1}^2 + \gamma_2 {r_2}^2))}{\delta^3} \qquad (6.15d)$$

where the common term δ is given by

$$\delta = \left((\gamma_1+\gamma_2)(r_1 r_2)^2(\gamma_1 {r_1}^2 + \gamma_2 {r_2}^2)\right)^{1/2}. \qquad (6.15e)$$

6.4 Experimental Setup

Experimental data were obtained at the National Criticality Experiments Research Center within the Device Assembly Facility at the Nevada National Security Site to validate the two-region model. The fissile material was a 4.5-kg sphere of weapons-grade, alpha-phase plutonium encased in stainless steel (to prevent contamination) known as the BeRP Ball, which has been extensively detailed in integral benchmark experiments [81, 85, 82, 83, 96, 1]. The BeRP Ball was reflected by various amounts of copper ranging from 1.27 cm to 10.16 cm in 1.27-cm increments for a total of eight configurations with a simulated k_{eff} multiplication factor ranging between 0.8278 and 0.9394; these configurations are the same as the copper-only cases of the subcritical copper-reflected α-phase plutonium (SCRαP) benchmark. Three-dimensional renderings with the bottom half of the hemishells and a two-dimensional schematic of the copper-reflected BeRP Ball assemblies are shown in Fig. 6.1. The 10.16-cm copper configuration measurement was repeated with the BeRP Ball replaced by a ^{252}Cf source; a photo of the open-face assembly is shown in Fig. 6.2. All measurements were 20 minutes long.

The assemblies were measured with an organic scintillator array (OSCAR [6]). Previous works have also used organic scintillators to perform Feynman-alpha measurements [97, 98, 99], although ^{3}He detectors are traditionally used. A photo of the experimental setup is shown in Fig. 6.3.

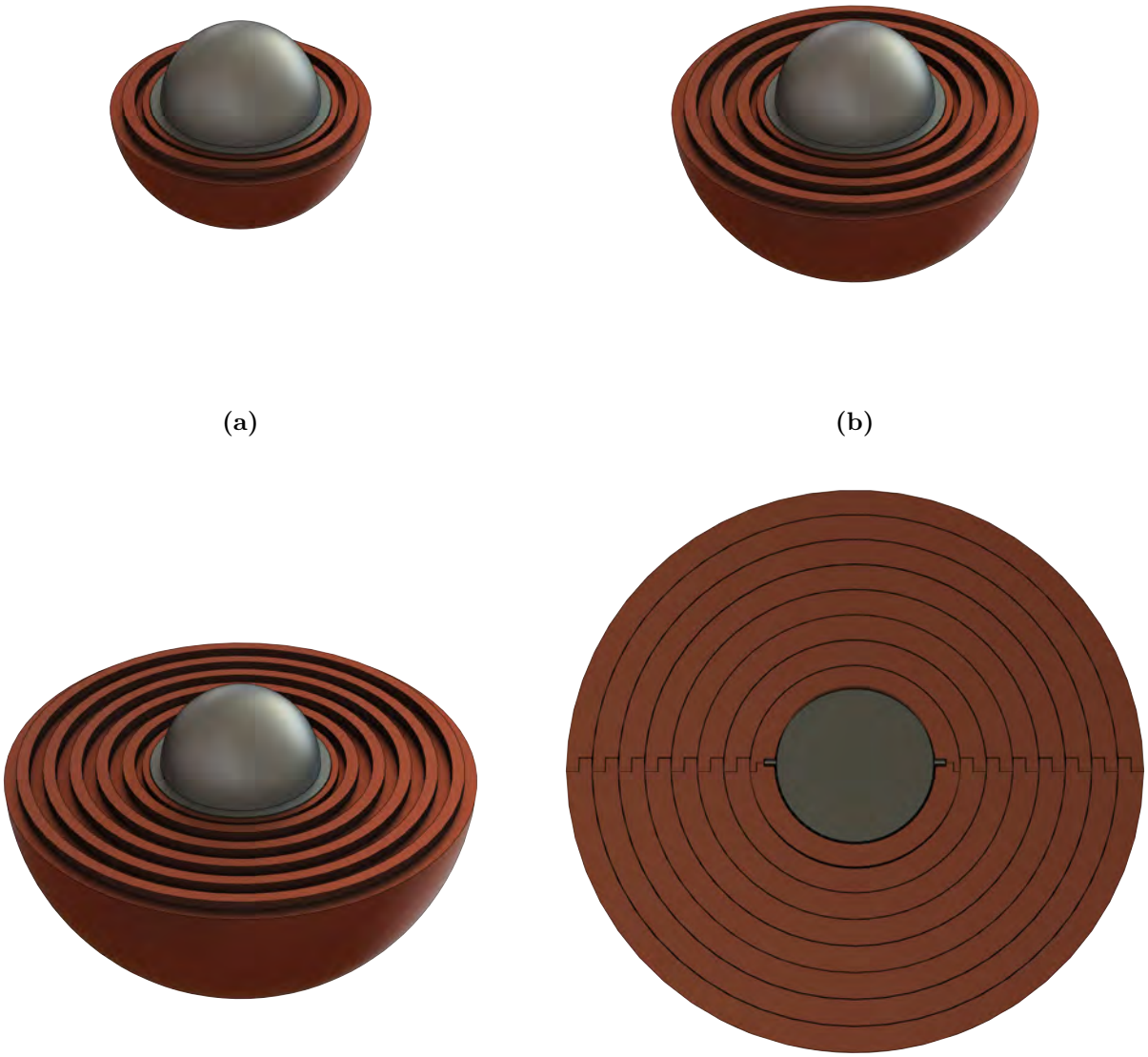

(a) **(b)**

(c) **(d)**

Figure 6.1: (Subfigs. 6.1a, 6.1b, and 6.1c) three-dimensional renderings of the BeRP Ball reflected by 2.54, 5.08, and 7.62 cm of copper. A two-dimensional engineering drawing of the 10.16-cm configuration detailing individual hemishells is shown in Subfig. 6.1d.

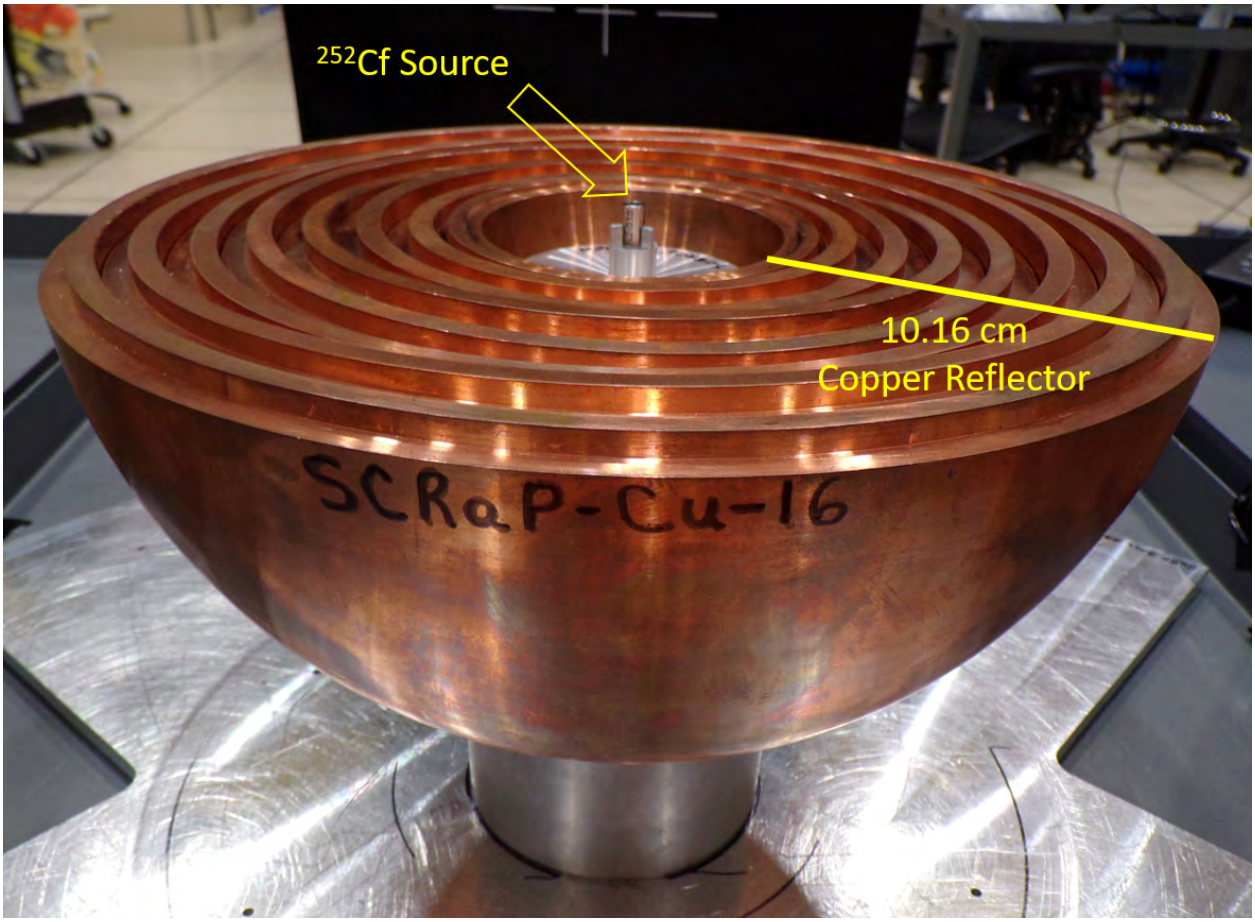

Figure 6.2: Photo of the ^{252}Cf source in 10.16 cm of copper.

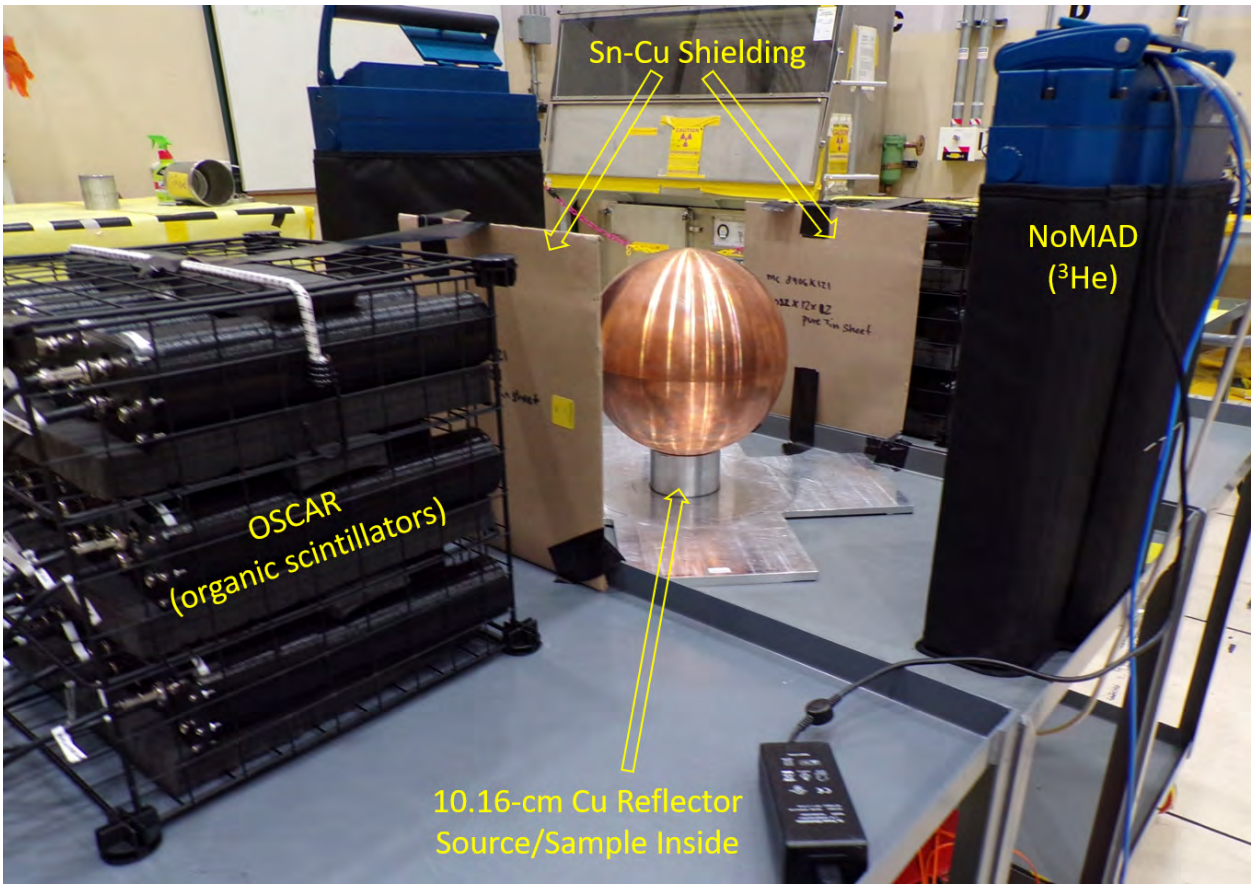

Figure 6.3: Annotated photo of the measurement setup including two organic scintillator arrays (OSCARs) and two Neutron Multiplicity ^{3}He Array Detectors (NoMADs) all 47 cm from the center of the assembly. The assembly comprises 10.16 cm of copper reflector.

6.5 Data Analysis

The data analysis is performed in two steps: the analysis of raw data to obtain the list mode data (a list of neutron detection times) and the Feynman-alpha analysis that creates and fits a Feynman histogram from the list mode data. The latter is discussed in subsec. 6.5.1 and the former in Chapter III.

6.5.1 Feynman-α Analysis

The Feynman histograms are constructed by calculating Y_2 from Eqn. (6.8) as a function of τ. The analysis of the BeRP Ball data used 200 values of τ logarithmically distributed

between 10^2 and 10^4 ns, and the analysis of the ^{252}Cf data used 200 values of τ distributed between 10^1 and 10^4. The resultant histograms are shown in Figs. 6.4 and 6.5, respectively. The histograms are fit by Eqn. (6.6) with a nonlinear least squares algorithm and weighting, with weights determined by the analytic method. The histograms were also fit with the one-exponential model in Eqn. (6.2) for comparison.

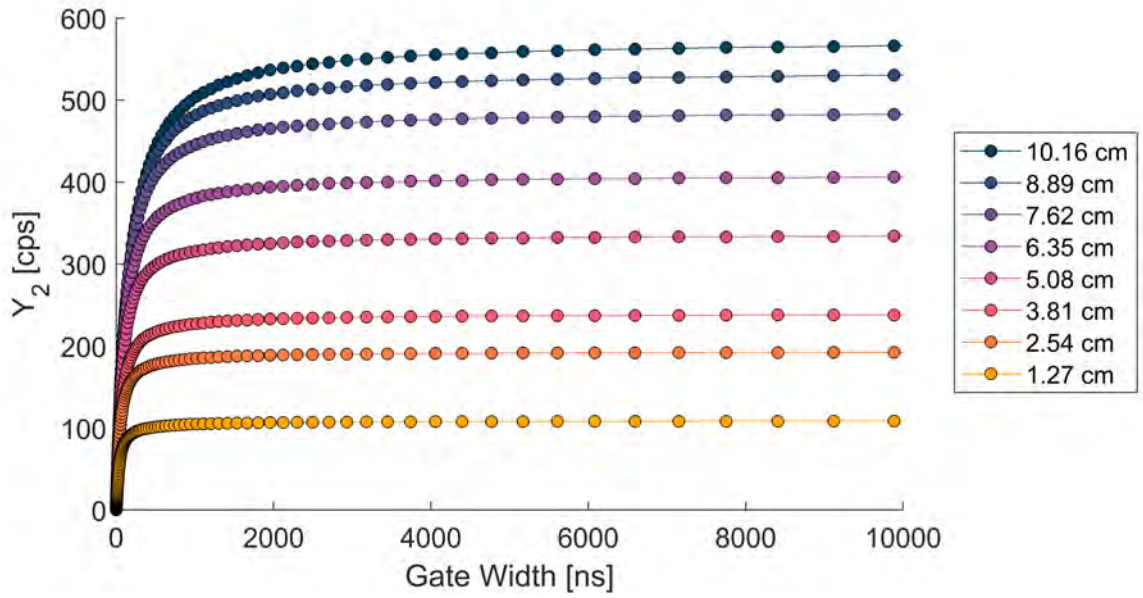

Figure 6.4: Feynman histograms for the BeRP Ball reflected by various amounts of copper. Error bars (one standard deviation) are smaller than the markers.

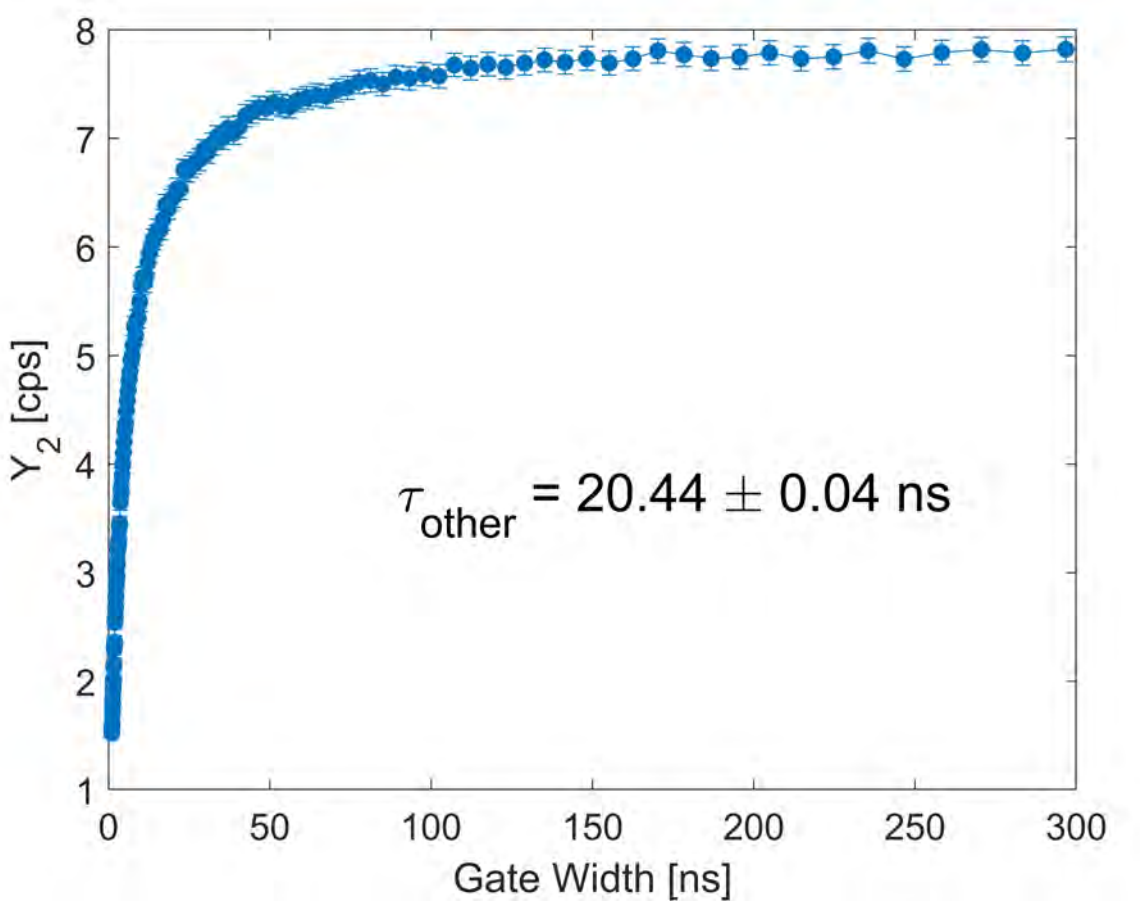

Figure 6.5: Feynman histogram and fit value for the measurement of ^{252}Cf in 10.16 cm of copper.

6.6 Results and Discussion

The two-region Feynman-alpha model is validated by comparing measured values of the prompt neutron period to simulated reference values for identical measurements given in Ref. [6]; Ref. [6] validated the two-region Rossi-alpha model. The simulated values from MCNP represent an independent determination of the prompt neutron periods, not a simulation of the detector response. Three parameters were obtained from simulation: k_{eff}, β_{eff} (the effective delayed neutron fraction), and τ_c (the mean lifetime of a neutron in the fissile core region). The KCODE subroutine of MCNP was used to calculate k_{eff} and β_{eff} while two F4 track-length tallies weighted by inverse velocity were used to calculate τ_c in the SDEF

subroutine. The prompt neutron period was then obtained from k_{eff}, β_{eff}, and τ_c.

Raw Feynman-alpha analysis produced prompt periods that were greater than the reference values by a constant time offset; the uniform mean difference was 21.37 ns and the inverse-variance-weighted mean difference was 20.13 ns. The time offset is due to lifetimes not associated with the multiplication kinetics such as detector dead time or neutron cross talk wherein one neutron registers multiple detections by scattering in multiple detectors [55, 100].

The mean lifetime due to non-multiplication kinetics, τ_{other}, is determined by measuring a ^{252}Cf source and repeating Feynman analysis; samples are typically small powders in which multiplication is negligible. The ^{252}Cf measurement in this work for the 10.16-cm copper reflector case yielded $\tau_{\text{other}} = 20.44 \pm 0.04$ ns, as annotated in Fig. 6.5. Similar measured data for the other configurations are not available, so the measured τ_{other} is verified with simulated results. The measurement was simulated using MCNPX-PoliMi and included all detection systems, tables, stands, shielding, and the floor. The simulation models detector response for 20-minute measurements of the 2.54, 5.08, 7.62, and 10.16 cm cases, and respective values are shown in Tab. 6.1. The mean non-multiplicative time constant from simulation is $\langle \tau_{\text{other}} \rangle_{\text{sim}} = 19.83 \pm 0.45$ ns, consistent with the measured value. A measured value for each configuration is generally preferred; in this work, the measured τ_{other} will be used for all configurations since there is no apparent trend shown in the simulated values.

Table 6.1: Simulated τ_{other} values for the 2.54, 5.08, 7.62, and 10.16 cm cases and a measured value for the 10.16 cm case.

Cu Thickness [cm]	Simulated τ_{other} [ns]	Measured τ_{other} [ns]
2.54	20.00 ± 0.03	–
5.08	18.44 ± 1.79	–
7.62	19.88 ± 0.11	–
10.16	21.02 ± 0.03	20.44 ± 0.04

The raw Feynman-alpha, corrected Feynman-alpha (raw values minus τ_{other}), and simulated reference values are shown in Fig. 6.6. The values are also summarized and compared to the Rossi-alpha values in Tab. 6.2. There is excellent absolute agreement between the

corrected Feynman-alpha and reference values; additionally, the Feynman-alpha values are more precise than the Rossi-alpha values (by one to two orders of magnitude) with one-standard-deviation measurement uncertainties less than 1%. The error is calculated relative to the simulated values (error = (measured−simulated)/simulated) since the simulations are used as reference in this work (whereas if the simulations were being validated instead of the measurements, the error would be calculated relative to the measured values). The corrected Feynman-alpha values are more accurate than the Rossi-alpha values below $k_{\text{eff}} \approx 0.92$, while the opposite is generally true above; the error for the more-accurate prompt neutron period estimate for each assembly is presented in blue in Tab. 6.2.

The now-validated two-region model is compared to the one-region model to determine regimes of applicability. Note that the two-region model is a generalization of the one-region model and that R in Eqn. (4.9) reduces to zero or unity when reflector is negligible [6]. Therefore, the two-region model can always be used and is not prohibitively more computationally expensive. The relative deviation between the one- and two-region models $((\alpha_1 - \alpha_2)/\alpha_2)$ is shown in Fig. 6.7. It is shown that the models deviate by more than 10% as the reflector and reflection increase, and are nearly identical when there is only a small amount of reflector.

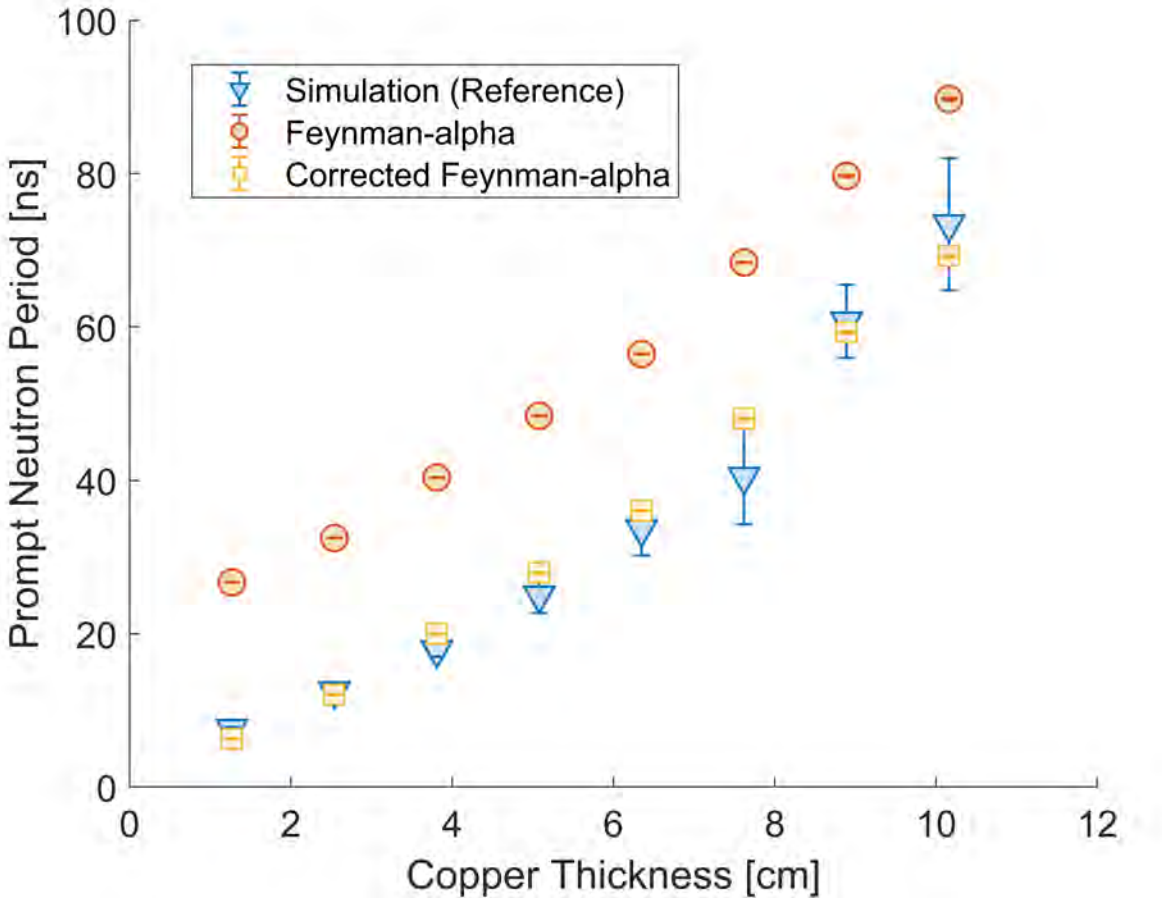

Figure 6.6: Comparison of measured and simulated prompt neutron periods, treating the simulated values as reference. The 'Feynman-alpha' data are pre-correction, whereas the 'Corrected Feynman-alpha' data are subtracted by the non-multiplication time constant determined from analysis on non-multiplying ^{252}Cf data.

Table 6.2: Prompt neutron period ($-\alpha^{-1}$) values for the Feynman-alpha, Rossi-alpha, and simulation approaches with one-standard-deviation uncertainties as a function of copper thickness (t_{Cu}). The error = (measured − simulated)/(simulated) for the measured approaches is given and the error for the more accurate measured approach is displayed in blue for each configuration. The simulated and Rossi-alpha values come from Ref. [6].

Assembly	Simulation		Feynman-alpha		Rossi-alpha	
t_{Cu} [cm]	k_{eff}	$-\alpha^{-1}$ [ns]	$-\alpha^{-1}$ [ns]	Error [%]	$-\alpha^{-1}$ [ns]	Error [%]
1.27	0.8278	7.6 ± 0.2	6.28 ± 0.04	-17%	13.4 ± 1.0	76%
2.54	0.8604	12.5 ± 0.4	12.06 ± 0.05	-3%	19.5 ± 1.0	57%
3.81	0.8831	17.9 ± 0.9	19.95 ± 0.06	11%	27.6 ± 4.0	54%
5.08	0.9005	25.0 ± 2.3	27.93 ± 0.05	12%	32.1 ± 4.9	28%
6.35	0.9137	33.7 ± 3.5	36.03 ± 0.05	7%	40.8 ± 7.4	21%
7.62	0.9239	40.5 ± 6.2	47.95 ± 0.07	18%	43.6 ± 5.1	8%
8.89	0.9322	60.7 ± 4.8	59.25 ± 0.13	-2%	68.8 ± 3.6	13%
10.16	0.9394	73.4 ± 8.6	69.27 ± 0.17	-6%	75.6 ± 4.5	3%

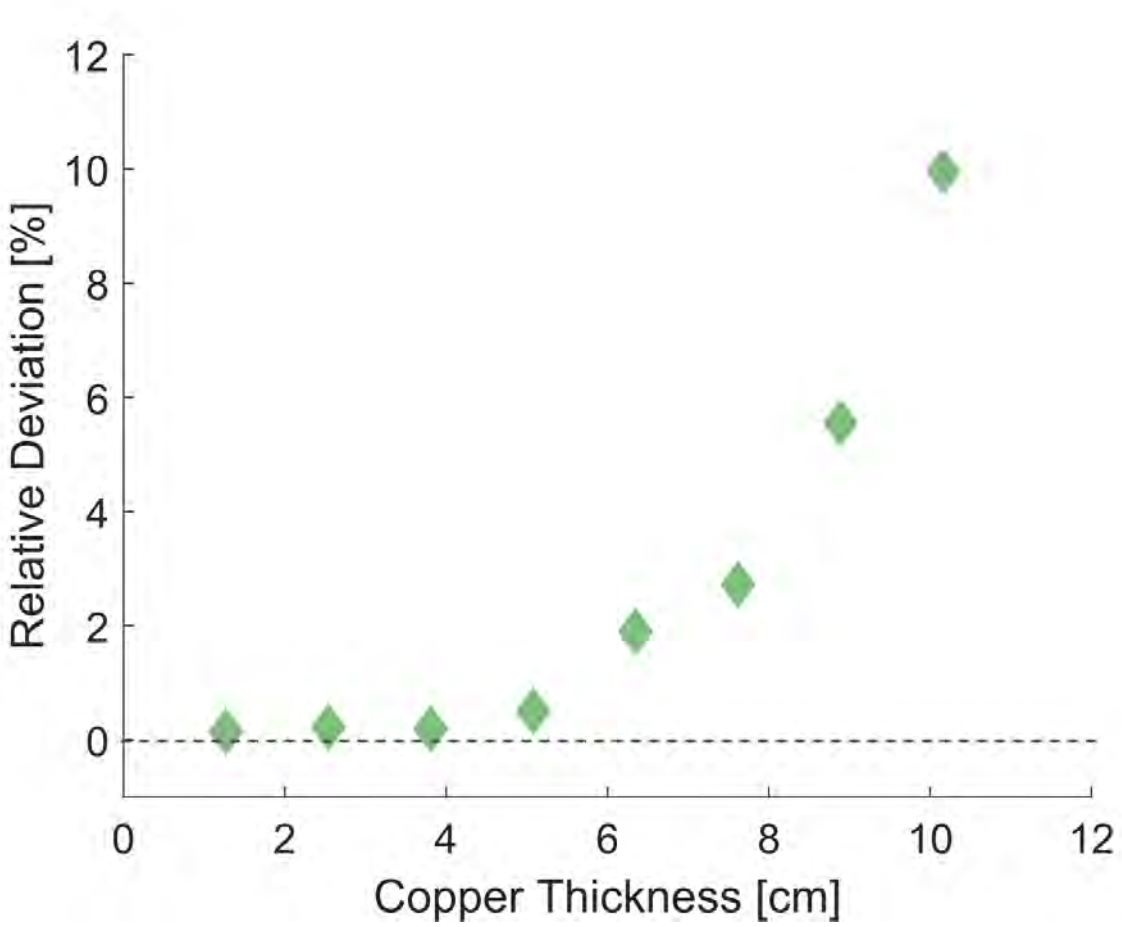

Figure 6.7: Relative deviation of the one-region model estimate of the prompt neutron period from that of the two-region model.

6.7 Summary and Conclusion

The two-region Feynman-alpha model was derived from the two-region Rossi-alpha model, rigorous propagation of measurement uncertainty was developed, and the two-region Feynman-alpha model was validated with organic scintillator measurements of copper-reflected, weapons-grade plutonium. The uncertainty propagation in this work should be used to improve fit accuracy and to properly propagate uncertainty, as demonstrated by other works [73, 92, 101]. Having validated the two-region model and demonstrated accuracy over the one-region model, the two-region model should be used over the one-region model. If the two-region model is unnecessary, it will reduce to the traditional case of the one-region model. In special circumstances, the two-region model may find two α eigenmodes if they dominate reflector-induced modes; modal effects are the subject of future work.

The copper-reflected plutonium measurements were complemented by a ^{252}Cf measurement to correct for non-multiplicative time correlations such as neutron cross talk or dead time. The method was effective since the ^{252}Cf is non-multiplying, thus this approach is recommended. One ^{252}Cf measurement was used as a representative for all cases and copper thicknesses since simulated values for the other cases were similar. Future work will further study the corrective ^{252}Cf measurement and investigate alternative cross talk and non-multiplicative corrections.

The Feynman-alpha approach offers better precision than the Rossi-alpha approach as well as improved accuracy for $k_{\text{eff}} < 0.92$, whereas the Rossi-alpha method is generally more accurate for larger multiplications. The trends are expected since the Feynman-alpha approach is an integral of the Rossi-alpha approach, though the Feynman-alpha approach is expected to struggle as k_{eff} approaches unity (whereas the Rossi-alpha approach improves as k_{eff} approaches unity). More fission chains overlap as k_{eff} increases, which can obfuscate accidentals and associated uncertainties in the Feynman-alpha method. Therefore, there is an optimization between Feynman-alpha and Rossi-alpha for regimes of preference, which is the subject of future work through the upcoming Measurement of Uranium Subcritical and

Critical (MUSiC) benchmark [86, 87].

CHAPTER VII

Conclusions and Future Work

7.1 Summary, Conclusions, and Future Work

Chapter I describes the historical foundation and motivation for the work accomplished in this dissertation and Chapter II derives the point kinetics simplification from the transport equation, the theoretical foundation for the neutron noise techniques used in this work. Chapter III presents the two types of detection systems: the current state-of-the-art ^{3}He-based Neutron Multiplicity Array Detector (NoMAD) and particle-discrimination-capable organic scintillation detectors that I introduce in the Organic Scintillator Array (OSCAR) for Rossi-alpha measurements. I demonstrate that organic scintillators augment the capabilities of ^{3}He detectors: the OSCAR has fewer accidental counts than the NoMAD and the OSCAR is sensitive to prompt neutron periods as fast as nanoseconds, whereas the NoMAD is limited to microseconds. Therefore, the OSCAR should be used for fast assemblies. Organic scintillators are generally less efficient than ^{3}He detectors. Thus, it may be preferential to use the NoMAD for slow, low-power assemblies that leak very few neutrons. The NoMADs can also be used for fast assemblies, not with the Rossi-alpha approach, but with other approaches such as those proposed in the Hage-Cifarelli formalism [93, 102]. In this work, I show that hydrogenous moderating material does not necessarily make the prompt neutron period slower; rather, it makes it shorter since neutrons spend less time in the core (the mean path to fission is shorter due to higher cross sections for moderated neutrons).

Chapter IV presents the two-region point kinetics theory that extends one-region models for Rossi-alpha measurements and then Chapter V validates the theory. The two-region model is a generalization of the one-region model and the validation shows that the two-region analysis reduces to that of the one-region model when negligible reflector is present. Therefore, the two-region model should always be used. A potential limitation of this conclusion is the presence of more than one detectable α-eigenmode (the fundamental mode is the prompt neutron decay constant) and the subject of future work. The two-region extension introduces new parameters such as f', which can be used with a simulated mean neutron lifetime in the core τ_c to estimate the number of cross-region leakages, and R, the linear interpolation parameter that weights the exponents from the two-exponential fit to estimate α. When R is zero or one, the two-region model reduces to the one-region model. It is shown that the minimum absolute difference between R and the extremes is a measure of reflection between similar assemblies.

The Feynman-alpha method is similarly generalized from one- to two-region point kinetics. In fact, the two-region Feynman-alpha analysis is derived from a double integration of the Rossi-alpha method. The Feynman-alpha method is also validated with measurements of weapons-grade plutonium.

The validation shows that the Rossi-alpha estimate of the prompt neutron period improves as k_{eff} approaches units, as expected and forecast by the assumptions taken to simplify the transport equation to point kinetics. Therefore, Feynman-alpha analysis was performed for the same assemblies and the compared. For all cases ($0.8278 \leq k_{\text{eff}} \leq 0.9394$), the Feynman-alpha method yielded better precision than the Rossi-alpha method. The trend is expected for subcritical, low-flux assemblies since the Feynman-alpha method is an integral analogy to the Rossi-alpha method, reducing histogram noise prior to fitting. The performance is expected to deteriorate more greatly for the Feynman-alpha method at higher multiplications due to overlapping fission chains and accidental counts. Similarly, the Feynman-alpha method (including correction) is more accurate than the Rossi-alpha method

for $0.8278 \leq k_{\text{eff}} \leq 0.9137$, whereas the Rossi-alpha method is generally more accurate for $0.9137 < k_{\text{eff}} \leq 0.9394$. A comparison between the two methods as a function of k_{eff} for bare assemblies is planned future work as part of the Measurement of Uranium Subcritical and Critical integral benchmark measurement campaign.

Rigorous propagation and quantification of measurement uncertainty are developed for both neutron noise techniques. A novel quasi-analytic method is developed and validated to estimate histogram uncertainty from a single measurement as compared to taking a sample standard deviation over many repeated measurements. When measurement time is limited or measurements of different assemblies are desired, the analytic method or other statistical methods (bootstrap or Bayesian) should be used in lieu of the sample method. The validated theory shows how to use histogram uncertainty to estimate a final uncertainty in the prompt neutron period, including weighting the nonlinear least squares fitting algorithm. The measured results show that weighting the fit not only properly accounts for uncertainty, but also improves accuracy.

The point kinetics models used in this work come from eliminating six (all but the time) variables from the transport equation. The truncation of the three spatial variables is *slightly* relaxed by considering more than one region. Organic scintillators do not inherently use reflector, hence neutrons do not scatter and lose energy prior to detection. Thus, such detection systems are sensitive to a portion of detected neutron energies and directional information, the three other truncated variables. Therefore, future work should consider further (differential) generalizations to the point kinetic models with variables that organic scintillators are sensitive to. A caveat is that detection systems are only sensitive to the information of detected neutrons that may be biased due to in-assembly scattering. Therefore, the f' parameter may need to be used to characterize scattering. The Rossi-alpha and Feynman-alpha methods are just two of many neutron noise techniques. Other neutron noise techniques should be compared and reevaluated with organic scintillators. Additionally, one could investigate combining several independent neutron noise techniques to increase the

number of degrees of freedom.

In the application space, organic scintillators requiring shorter measurement times than ^{3}He to achieve the same precision translates to being able to measure more assemblies and conduct comprehensive surveys, whereas current measurements/assays may select a random subset of samples and hope for accurate representation. In a fixed measurement time, organic scintillators are more precise (some times by factors as great as two or three orders of magnitude). Such drastic improvements to precision could, for example, improve nuclear data. Beyond improving the accuracy of data analysis, the new theory developed in this dissertation results in exploitable parameters (e.g., the R parameter) and tools/methods for optimizing current techniques (e.g., error and uncertainty minimization by selection of analytic-uncertainty-informed histogram parameters).

Appendices

Appendix A

Comparison of OSCAR and NoMAD Rossi-α Measurements

This appendix compares the OSCAR and NoMAD detection systems in Rossi-alpha measurements. The work in this appendix comes from my conference paper "Fast Ross-alpha Measurements of Plutonium using Organic Scintillators" a Proceeding of the American Nuclear Society's 2020 Physics of Reactors Meeting [58] and my paper titled "Rossi-alpha measurements of fast plutonium metal assemblies using organic scintillators" published in Nuclear Instruments and Methods in Physics Research Section A: Accelerators, Spectrometers, Detectors and Associated Equipment [3].

A.1 Assembly Specification and Experimental Setup

A.1.1 Assembly Specifications

In this work, the bottom layer of the Comet critical assembly – lead-moderated, copper-reflected plutonium (93 wt% ^{239}Pu) – was measured. A 3D rendering of the assembly is shown in Fig. A.1; the layout of the bottom layer of copper or plutonium boxes is shown in Fig. A.2, and a sample plutonium box is shown in Fig. A.3 [5]. The total mass of plutonium was approximately 15 kg.

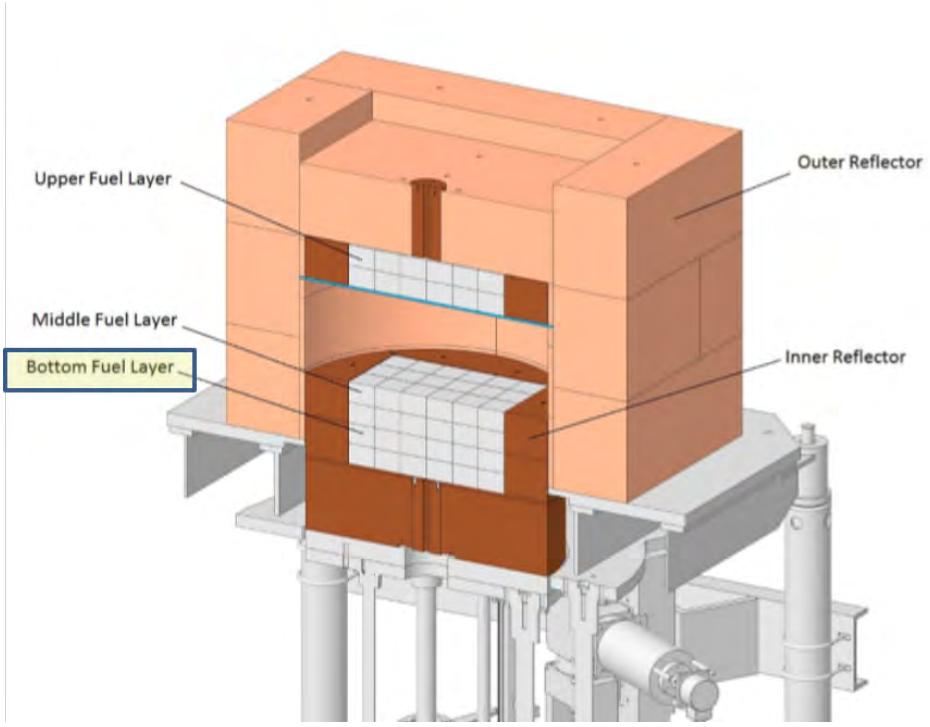

Figure A.1: 3D rendering of the Comet critical assembly [5].

Cu	Cu	6 Pu 2 Pb	6 Pu 2 Pb	Cu	Cu
Cu	6 Pu 2 Pb	6 Pu 2 Pb	6 Pu 2 Pb	6 Pu 2 Pb	Cu
6 Pu 2 Pb	6 Pu 2 Pb	6 Pu 2 Pb	6 Pu 2 Pb	6 Pu 2 Pb	6 Pu 2 Pb
6 Pu 2 Pb	6 Pu 2 Pb	6 Pu 2 Pb	6 Pu 2 Pb	6 Pu 2 Pb	6 Pu 2 Pb
Cu	6 Pu 2 Pb	6 Pu 2 Pb	6 Pu 2 Pb	6 Pu 2 Pb	Cu
Cu	Cu	6 Pu 2 Pb	6 Pu 2 Pb	Cu	Cu

Bottom Layer

Figure A.2: Bottom layer box layout [5].

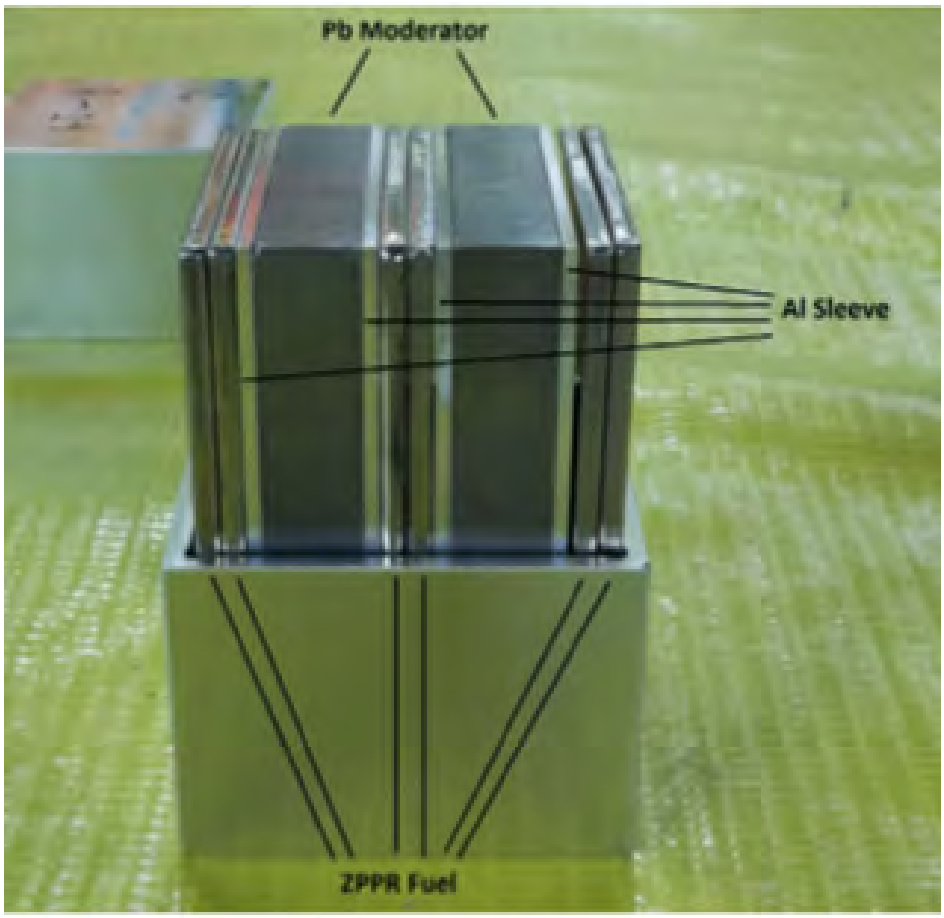

Figure A.3: Photo of a plutonium box [5].

A.1.2 Simulation of the Assembly

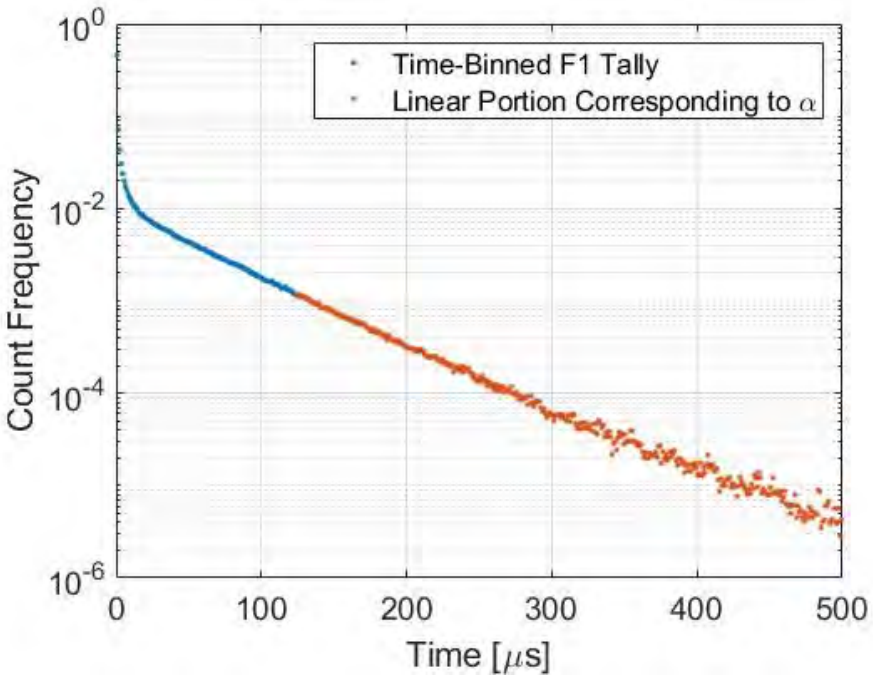

Figure A.4: Sample plot of the time-binned surface tally (F1) used to estimate the Rossi-alpha.

To estimate the prompt neutron decay constant, α, the measurement was simulated using MCNP6®. The KCODE option estimated $k_{\text{eff}} \approx 0.624$. To determine α, surface (F1) and point-detector (F5) tallies were time-binned, and the tails (linear on a semilog plot) were fit. A sample time-bin tail-fit plot is shown in Fig. A.4 and $\alpha = 52.3 \pm 2.5$ ns. The uncertainty comes from the fit uncertainty.

A.1.3 Experimental Setup and Detection System Details

In the measurement of the assembly, two organic scintillator arrays (OSCARs) and one Neutron Multiplicity ^{3}He Array Detector (NoMAD) were used. An OSCAR comprises 12 5.08 cm × 5.08 cm diameter *trans*-stilbene organic scintillators coupled to photomultiplier tubes [63, 64]. The NoMAD is similar to the MC-15 detection system [**?**], comprising 15 ^{3}He detectors embedded in a polyethylene matrix. The systems were placed 50 cm from the edge

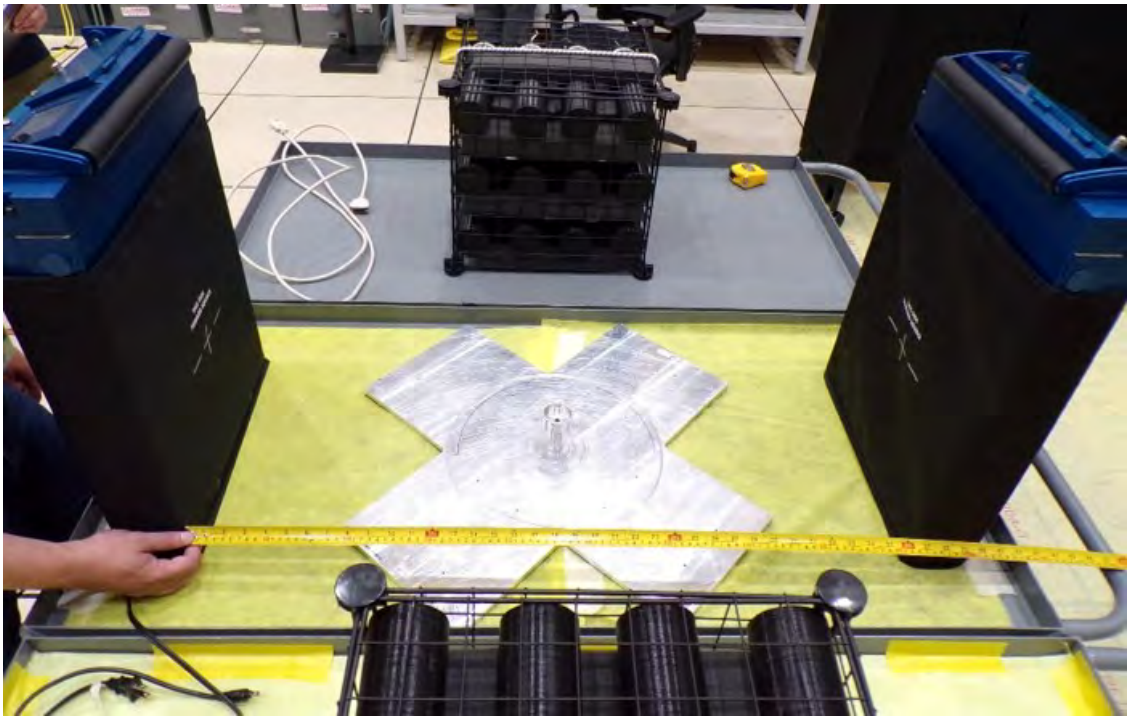

Figure A.6: Photo of detection systems.

of the assembly; a schematic is shown in Fig. A.5 and a photo of the systems side-by-side is shown in Fig. A.6. For this work, only 21 of the 24 OSCAR detectors were operational. Based on neutron detection rates, the NoMAD (in the given configuration) is 3.34 times more efficient than the OSCARs.

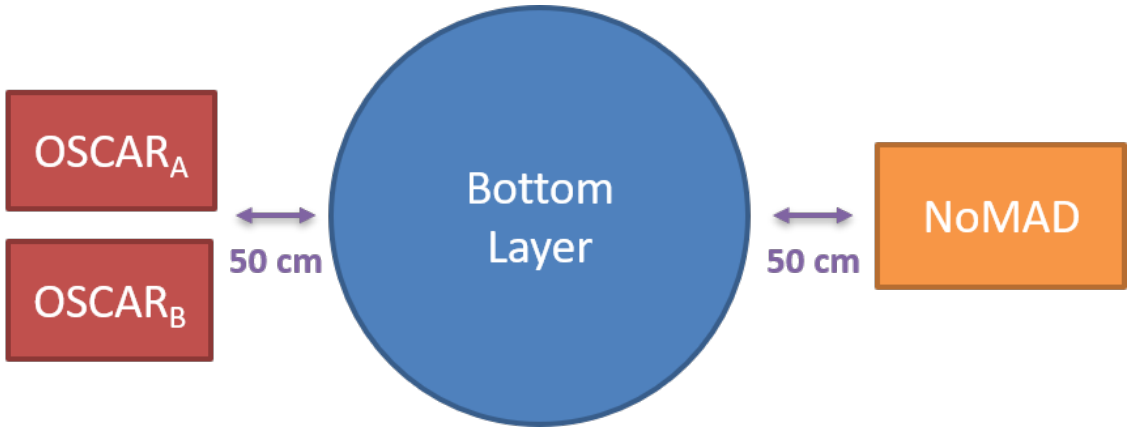

Figure A.5: Schematic of detector placement.

A.2 Results and Discussion

Unnormalized, non-constant-subtracted Rossi-alpha histograms generated from two hours of data for each detection system are shown in Fig. A.7. The OSCAR has fewer accidentals than that of the NoMAD: the constant value of the tail for the NoMAD is 95% of the maximum value, whereas the constant value of the tail for the OSCAR is only 0.7% of the maximum value. In some cases, the high proportion of the accidentals in the case of the NoMAD may obscure the second exponential. Obscuring the second exponential would reduce the fit model to a single exponential fit; however, since the parameters of interest are a linear combination of the two exponentials, α and ℓ_{ctd} cannot be determined.

Fit metrics plotted as a function of measurement time (and bin width for the NoMAD) are shown in Fig. A.8. The root mean square error (RMSE) is normalized by the asymptotic values of the respective data series such that the y-axis is a measure of convergence. It takes the OSCAR less than 30 minutes to be within 50% of its asymptotic value, while it takes the NoMAD approximates 120 minutes (note that RMSE is fairly independent of the bin width, as expected). It takes the OSCAR less than 20 minutes to achieve an R^2 value greater than 0.90, whereas the the NoMAD with 2 μs bins requires approximately 70 minutes. The NoMAD's R^2 convergence could be improved by increasing the bin widths; however, 2 μs bin widths are already large compared to the time-decay constant (52.3 $\pm$ 2.5 ns) the NoMAD is trying to observe. Reducing the bin widths to increase sensitivity to the physical phenomenon the system is trying to measure results in increases in the time is takes the NoMAD to achieve $R^2 > 0.90$; bin widths of 1 μs require 140 minutes and bin widths of 500 ns require 280 minutes (the relationship is approximately linear).

From simulation, the "true" value of α for the assembly is taken to be 52.3 $\pm$ 2.5 ns. Fitting the OSCAR data with a two exponential, α is estimated to be 47.4 $\pm$ 2.0 ns. The error is 9.37% and, qualitatively, the values are similar since the 1.09σ-confidence intervals overlap. The NoMAD estimate of α is $\approx$ 37 μs. The NoMAD has a known slowing down time of 35-40 μs and, because $\alpha \ll 35$ μs, the NoMAD is likely only sensitive to the neutron

moderation time.

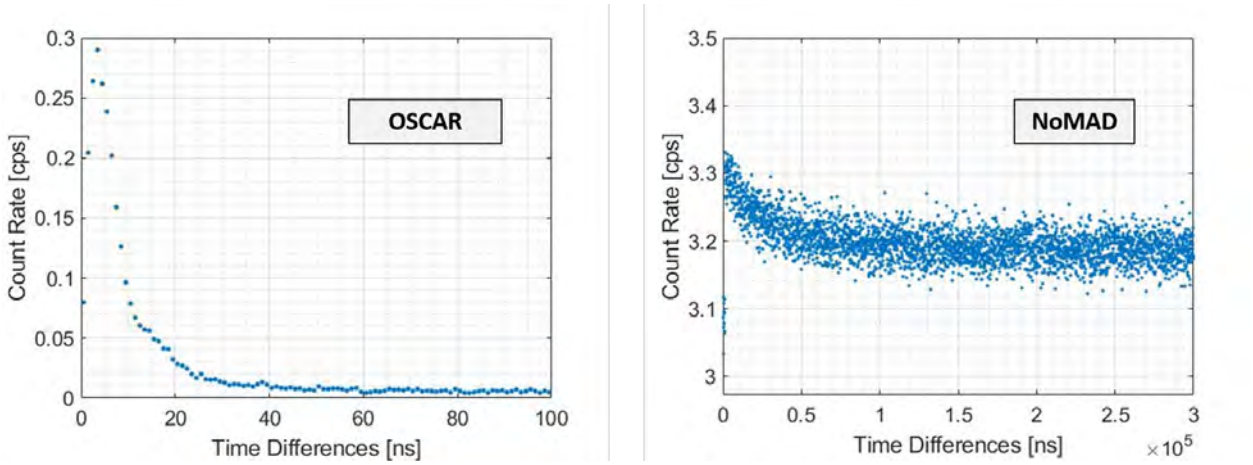

Figure A.7: Unnormalized, non-constant-subtracted Rossi-alpha histograms.

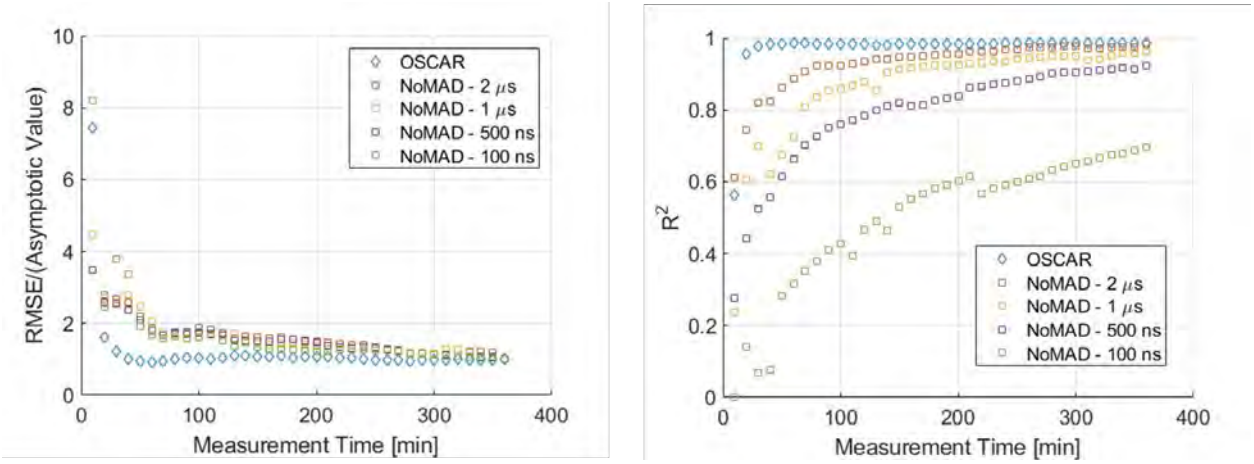

Figure A.8: Fit metrics as a function of measurement time for the NoMAD at different bin widths and the OSCAR.

A.3 Conclusions and Future Work

In this work, the organic scintillator array (OSCAR), comprising 21 total operational *trans*-stilbene detectors, and the Neutron Multiplicity ^{3}He Array Detector (NoMAD), comprising 15 ^{3}He tubes embedded in a polyethylene matrix, simultaneously measured 15 kg of plutonium (93 wt% ^{239}Pu) moderated by lead and reflected by copper with $k_{\text{eff}} = 0.624$ and $\alpha = 52.3 \pm 2.5$ ns. It was found that the OSCAR converged on its estimate of α faster

than the NoMAD, which translates to reduced procedural and operational costs in practical implementation. The convergence needs to be investigated further for assemblies where α is much larger ($\alpha \propto 10 - 100s$ of μs). Because neutrons are moderated in the polyethylene matrix of the NoMAD (and moderation is not inherent to the OSCAR), the OSCAR is an inherently faster detection system. The entire Rossi-alpha histogram (reset time) is less than 100 ns for the OSCAR (1 ns bins), whereas 100 ns is the clock tick length for the NoMAD. Therefore, for fast assemblies ($\alpha \propto 1 - 100s$ of ns), it is more suitable to use the OSCAR that estimated the true α within 1.09 standard deviations and an error of 9.37% (on the order of uncertainty in nuclear data). Larger accidental contributions are more likely to wash out time information; the NoMAD has a large accidental contribution and the OSCAR has a negligible accidental contribution. Future work involves determining when each system is more suitable to a given measurement. Furthermore, gamma-ray and mixed-particle Rossi-alpha will be investigated with the organic scintillators.

Appendix B

Simulation of the Nondestructive Assay of ^{237}Np using Active Neutron Multiplicity Counting

This appendix describes an initial investigation into a well-counter-type detection system customized for the active neutron multiplicity counting of ^{237}Np; neutron multiplicity counting is another neutron noise technique that is typically applied to safeguards applications. The work in this section comes from my work titled "Simulation of the Nondestructive Assay of ^{237} using Active Neutron Multiplicity Counting" published in Nuclear Science and Engineering.

B.1 Introduction and Motivation

The goal of nondestructive assay in safeguards applications is to precisely measure (verify) the mass of an unknown sample in a reasonable amount of time [103, 7]. The capability to effectively assay ^{237}Np, a potentially weapons-usable isotope, is currently a missing piece in the verification and safeguards toolbox. This study focuses on radiation transport simulations of both the ^{3}He-based epithermal neutron multiplicity counter (ENMC) in the active configuration, the flagship system used for the assay of ^{235}U, as well as an organic scintillator-based multiplicity counter (OSMC). Consistent with ^{3}He-based active neutron correlation counter capabilities when measuring ^{235}U, it is desirable to distinguish 10 grams of ^{237}Np in

a 20-minute measurement [103, 104].

The United States (US) Department of Energy (DOE) classifies ^{237}Np as "other nuclear material," which is a class of potentially weapons-usable material. The international community also recognizes the possibility for ^{237}Np-based nuclear weapons [105]. The bare sphere critical mass for ^{237}Np is 40-60 kg, which in metal form corresponds to a 10 cm radius sphere [106, 107]. Los Alamos National Laboratory estimates the critical mass of ^{237}Np at 57 $\pm$ 4 kg [108].

Due to the relatively small size of a critical ^{237}Np sphere and the relative stability of ^{237}Np (2.144×10^6 years), a ^{237}Np-based weapon is potentially feasible. Typical attributes that make a nuclear material unattractive for use in a nuclear weapon, such as heat generation, spontaneous fission, and self-protecting dose rate are nearly nonexistent for ^{237}Np [109]. The US DOE has recognized the possibility of ^{237}Np-based weapons and has declared it within its safeguards metrics as "equivalent to ^{235}U" and reportable in gram quantities. Furthermore, 3,000 kilograms of ^{237}Np are produced per year in the US. ^{237}Np is a byproduct of the nuclear fuel cycle and has commercial applications such as ^{238}Pu production via ^{237}Np target irradiation [110, 111]. The feasible utilization of ^{237}Np in nuclear weapons and its production makes it desirable to have an adequate ^{237}Np assay system.

B.2 Background

B.2.1 Active Interrogation of ^{237}Np

Active interrogation must be used to estimate the mass of an assay sample of ^{237}Np in hours or less. Passive assays are infeasible due to ^{237}Np having a low gamma-ray emission rate (2.6×10^7 gammas/s/g), low gamma-ray energies (97% of gammas are less than 100 keV), and a spontaneous fission rate of 2×10^{-12} fissions per decay [112]. The decay product of ^{237}Np, ^{233}Pa (half-life of 27 days), is of limited use due to all of the prominent gamma rays consisting of relatively low energy: 300.1 keV (6.6% yield), 311.9 keV (38.5% yield)

and 340.5 keV (4.4% yield). Due to the energies, ^{233}Pa gamma rays are easily shielded by dense, high-atomic mass materials (including the self-shielding from the ^{237}Np). The "infinite thickness" for 340.5 keV gamma rays in ^{237}Np metal (20.2 g/cm^3) is 1.025 cm [103]. The decay product of ^{233}Pa is ^{233}U, which has a half-life of 1.6×10^5 years, thus stopping the decay chain for practical purposes.

AmLi is a popular neutron source for active interrogation (a source producing neutrons to induce fission in a sample), which emits neutrons with an average energy of 0.59 MeV [113]; however, induced fission in ^{237}Np occurs with a threshold of approximately 0.8 MeV. Thus, instead of using AmLi, AmBe is a good choice for the interrogation of the ^{237}Np samples in the simulations. For AmBe, the mean neutron energy is approximately 5.0 MeV and the maximum energy is approximately 11.0 MeV [103].

B.2.2 Active Neutron Multiplicity Counting

The theory of active neutron multiplicity counting is summarized in this section, based on the more-comprehensive discussion by Ensslin et al. in Ref. [114]. With current capabilities, in the context of neutron multiplicity counting, it is generally not possible to determine the origin of neutrons on a case-by-case basis. For example, three neutrons detected in a given coincidence window (or gate) could be a three-neutron multiplicity, double-and-single-neutron multiplicities at the same time (which can happen in three possible ways from three coincident neutron detections), or three single-neutron multiplicities at the same time. Because there are multiple, indistinguishable, possible multiplicity realizations, all possibilities are considered by way of factorial moment counting and the multiplicity shift register binning technique [93, 74]. The multiplicity shift register binning technique treats each neutron detection as a gate trigger, opens a gate after the trigger in which factorial moment counting is performed, and opens a second, identical gate after a fixed long delay to perform factorial moment to subtract accidental/chance coincidences [74]. Using the factorial moments, the singles, doubles, and triples multiplicity rates are calculated [102].

Note that the singles, doubles, and triples multiplicity rates are not the rates of one, two, and three counts in a gate, but rather the first, second, and third factorial moments of the distribution.

The output of the initial data processing includes the neutron doubles (D) and triples (T) multiplicity rates and the doubles and triples gate fractions, f_d and f_t. The doubles/triples gate fractions are the fraction of doubles/triples that are actually counted in the gate of the multiplicity shift register. For detectors having a die-away time characterized by a single-exponential model (with decay constant τ),

$$f_d = e^{-P/\tau}\left(1 - e^{-G/\tau}\right) \quad \text{and} \tag{B.1}$$

$$f_t = {f_d}^2, \tag{B.2}$$

where P is the shift register pre-delay and G is the gate width. The gate fractions may also be calculated experimentally and usually are since the single-exponential model is inadequate for real detectors [114].

The outputs are related to the induced fission rate (F), system parameters, and nuclear data by

$$D = \left[\frac{F{\epsilon_f}^2 f_d \nu_{s2}}{2}\right] C_d \quad \text{and} \tag{B.3}$$

$$T = \left[\frac{F{\epsilon_f}^3 f_t \nu_{s3}}{6}\right] C_t, \tag{B.4}$$

where ϵ_f is the efficiency for detecting induced-fission neutrons; ν_{s2}, ν_{s3} are the second and third reduced factorial moments for interrogation source-induced fissions in ^{237}Np; and C_d, C_t are correction factors for self-multiplication of doubles and triples.

The C_d and C_t correction factors are functions of nuclear data and M, the neutron

self-multiplication, given by

$$C_d = M^2 \left[1 + \frac{(M-1)\nu_{s1}\nu_{i2}}{\nu_{s2}(\upsilon_{i1}-1)}\right], \text{ and} \tag{B.5}$$

$$C_t = M^3 \left[1 + \frac{(M-1)(3\nu_{s2}\nu_{i2} + \nu_{s1}\nu_{i3})}{\nu_{s3}(\nu_{i1}-1)} + \frac{(M-1)^2(3\nu_{s1})(\nu_{i2})^2}{\nu_{s3}(\nu_{i1}-1)^2}\right], \tag{B.6}$$

where $\nu_{i1}, \nu_{i2}, \nu_{i3}$ are the first, second, and third reduced factorial moments for subsequent generations of fission neutron-induced fissions in ^{237}Np. When D and T are nonzero, it is possible to solve for M independent of F by taking the ratio of Eqns. (B.3) and (B.4). The resultant polynomial is a cubic in M, which means there are three possible values for M. Of the calculated values, typically only one is physical. Having calculated M and F, the sample mass is calculated with

$$m = \frac{F}{CY}, \tag{B.7}$$

where C is the coupling term and Y is the total output of the interrogation source in neutrons per second. Note that the variance in estimated sample mass, ${\sigma_m}^2$, varies as (assuming no uncertainty in Y and independence between F and C)

$${\sigma_m}^2 = \left(\frac{1}{CY}\right)^2 {\sigma_F}^2 + \left(\frac{F}{Y}\frac{1}{C^2}\right)^2 {\sigma_C}^2. \tag{B.8}$$

The coupling term, C, is unique to active multiplicity counting to account for coupling between source neutrons and the sample; F for active multiplicity counting is the source neutron-induced fission rate, whereas F in passive multiplicity counting is the spontaneous fission rate. The value of C is a function of M and the values are empirically determined, typically with known-mass standards. Using the standards, D and T are measured and subsequently used to calculate M and F. Using the known values of m, F, and Y, C is calculated and paired with the respective value of M. After obtaining a collection of C and

M pairs, the data are fit with

$$C = a - \frac{b(M-1)}{1+c(M-1)}, \tag{B.9}$$

where a, b, and c are fit parameters. Originally, the trend was fit with a model ($CY = a_0 + b_0 m^{-1/3}$) such that F was proportional to sample mass and surface area ($F = a_0 m + b_0 m^{2/3}$). Later work resulted in Eqn. (B.9), which is desirable since it is independent of mass and density (shown for the case of ^{235}U) [114].

B.3 Simulation and Detection System Specifications

Two simulation series were performed in this study. MCNP6 [50] was used to simulate the ENMC, which comprises 121 ^{3}He gas proportional counters embedded in a polyethylene matrix [115, 116]. MCNPX-PoliMi ([52, 117]) was used to simulate an OSMC, which, in this design, comprises 24 trans-stilbene detectors [63, 2]. The ^{237}Np samples are square plates with a 2 cm $\times$ 2 cm cross-section; the density is 20.45 g/cm^3 and the thickness of the plates is varied to obtain the desired mass. A total of 20 masses logarithmically distributed between 10 and 1000 grams is used in the simulations for this work. Note that the relative uncertainty needed to differentiate two sequential sample masses is 12%.

B.3.1 The Epithermal Neutron Multiplicity Counter (ENMC)

The ENMC utilizes 121 ^{3}He tubes pressurized to 10 atm and embedded in polyethylene moderator. ENMC dead times are on the order of tens of nanoseconds and neutron die-away times are on the order of tens of microseconds. For active-interrogation measurements, the ENMC contains two cavities to hold interrogation sources [116]. In this work, an AmBe source (4.671×10^5 neutrons per second, based on a previous measurement at the Joint Research Centre in Italy [118]) was placed in each cavity. An annotated, two-dimensional rendering of the simulation geometry is shown in Fig. B.1, and a three-dimensional rendering

is shown in Fig. B.2. The ENMC was designed for AmLi sources that have been replaced with AmBe; this work does not attempt to optimize the source cavity for the swap. Previous published work investigating the use of higher energy neutron sources with ^{3}He well counters has had limited scope at changing the end plug geometry or composition [119, 120]. Previous work has shown that simple changes such as moving the interrogation source further from the sample (and the ^{3}He tubes) results in an overall increase in doubles count rate uncertainty [119]. The reduction in accidental doubles counts is less than the reduction in induced fissions in the sample.

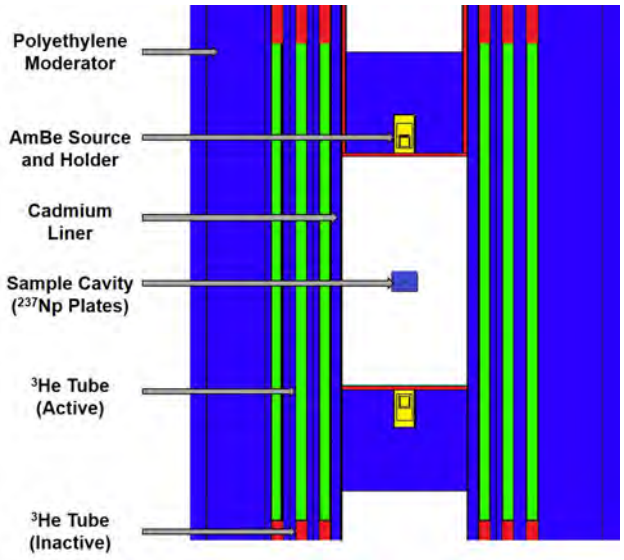

Figure B.1: Two-dimensional annotated rendering of the ENMC.

Figure B.2: Three-dimensional partial rendering of the ENMC; the moderating polyethylene is not shown.

B.3.2 An Organic Scintillator-based Multiplicity Counter (OSMC)

The OSMC used in this work is based on the fast-neutron multiplicity counter used by Di Fulvio et al. to actively assay uranium samples, which had a system die-away time of approximately 40 ns and virtually no dead time [121]. Instead of using 8 trans-stilbene and 8 EJ-309 organic scintillators, this work simulates 24 5.08 cm long $\times$ 5.08 cm diameter stilbene detectors. It is desirable to have one detector type for uniformity and the trans-stilbene detectors were chosen for superior pulse-shape discrimination capabilities in comparison to the EJ-309 detectors [64]. Similar to the ENMC simulations, the samples of ^{237}Np were interrogated with two AmBe sources emitting 4.671×10^5 neutrons per second and collimated by 7.11 cm of borated-polyethylene encased in 1.00 mm of bismuth (inspired by Ref. [122]). The AmBe were simulated as point sources positioned at far edges of the borated polyethylene portion of the collimator. A two-dimensional rendering of the geometry is shown in Fig. B.3.

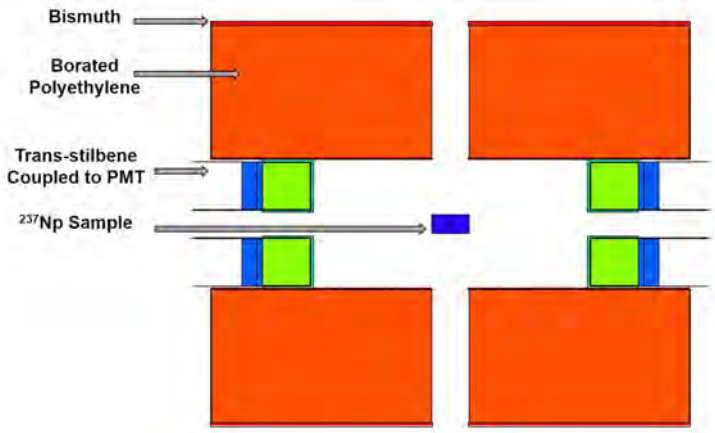

Figure B.3: Two-dimensional rendering of the OSMC. The thickness of the bismuth is not to scale for illustrative purposes.

B.4 Data Analysis

B.4.1 Data Analysis for the ENMC

The singles, doubles, and triples multiplicity rates are obtained with an F8 tally using the CAP parameter. The pre-delay is 1.5 μs and the gate width is 24 μs. No long delay is included because MCNP6 does not use this input in its calculations. The output of the simulations includes the multiplicity rates and uncertainty based on Monte Carlo counting statistics. Using Ref. [123], the expected uncertainty from a physical measurement is calculated, accounting for factors including the long delay and background contribution. The input parameters include the multiplicity rates, measurement time, gate width, pre-delay, and die-away time (which is 21.8 μs [116]).

B.4.2 Data Analysis for the OSMC

The output of the MCNPX-PoliMi simulations is a collision file detailing the interactions that occurred in the detector cells. The MPPost post-processing code is then used to determine if a detection is registered above a given threshold (75 keVee, which corresponds to approximately 600 keV neutron energy deposition on a proton) and the output is a list of

neutron detection times [124, 2]. In this work, the multiplicity shift register binning technique is used with a 100 ns gate width and a long delay of 500 ns. There is no pre-delay and it is assumed that $f_t = {f_d}^2 = 1$ due to the fast response of organic scintillators. Using analytic uncertainty equations, the output of the initial data analysis is the multiplicity rates with uncertainty and the gate fractions [95, 94].

Once the doubles and triples rates are extracted, Eqns. (B.3) and (B.4) are simultaneously solved to obtain M and F. While M has three possible solutions, only one solution is physical for the data simulated in this work. Finally, mass (m) would be calculated using Eqn. (B.7) and the coupling term, C, would be obtained from a system-specific fit, $C = C(M)$. Since the mass is known (specified in the simulation) and the coupling term is not, this work calculates C instead. The fit is calculated using nonlinear least squares fitting with the model defined by Eqn. (B.9). The nuclear data constants and detection system parameters used for the OSMC calculations are tabulated in Tables B.1 and B.2. Note that the values in Table B.1 are expected to change significantly as nuclear data for ^{237}Np improves and are included for illustrative purposes only.

Table B.1: ^{237}Np nuclear data constants used in the OSMC calculations.

ν_{s1}	ν_{s2}	ν_{s3}	ν_{i1}	ν_{i2}	ν_{i3}
3.2631	7.5170	10.2409	2.9601	5.8517	5.8783

Table B.2: Detection system constants for the OSMC.

ε_f	f_d	f_t
0.0577	1	1

B.5 Results and Discussion

B.5.1 Results for the ENMC

The ENMC doubles and triples multiplicity rates with estimated (Ref. [123]) error bars are shown in Figs. B.4a and B.4b, respectively, for a 20-minute measurement.

As seen in Fig. B.4b, the uncertainty in the triples rate is large for the ENMC given a 20-minute measurement; at best, the relative standard deviation is 59.3% ($\approx 1\times10^6 \pm 6\times10^5$ triples counts per second for the 1 kg sample). With such high uncertainties, active neutron multiplicity counting is infeasible with the ENMC using AmBe interrogation sources. Using the estimated measurement uncertainty equations from Croft et al. in Ref. [123], the ENMC requires approximately 30 minutes to resolve the triples rates between the two largest masses (785 and 1,000 g), 1 day and 18 hours to resolve 10.0 and 20.7 g, and approximately 6 days to resolve the two smallest masses (10.0 and 12.7 g). One primary cause of the large uncertainties is the high singles count rate of approximately 2.8×10^5 counts per second. If three of these singles counts occur within the gate width (24 μs), the set will be counted as an accidental triples count. The active configuration of the ENMC was designed to minimize three singles in the same gate width for AmLi interrogation sources. However, the higher energy AmBe neutrons are often not absorbed before reaching the ^{3}He tubes, which results in approximately 30% of the interrogation neutrons being detected. Based on Fig. B.4a, doubles rate-based calibration is feasible for bulk sources; however, large measurement times are required to resolve sample masses less than 100 g. A measurement time of 1.5 hours (calculated the same way as for the triples rates) is required to resolve the doubles rates between 10.0 and 12.7 g. It should be noted that as sample mass approaches zero, the doubles counts do not approach zero in Fig. B.4a. The nonzero behavior is due to (n,2n) reactions with beryllium in the AmBe sources. Induced fission with ^{241}Am in the AmBe sources does occur, but this reaction rate is approximately 0.1% of that of (n,2n) in the beryllium. The discussion regarding the nonzero contributions to the doubles counts is supported by the fact that the triples counts approach zero in Fig. B.4b as the sample mass approaches zero; (n,2n) reactions do not contribute significantly to the triples counts.

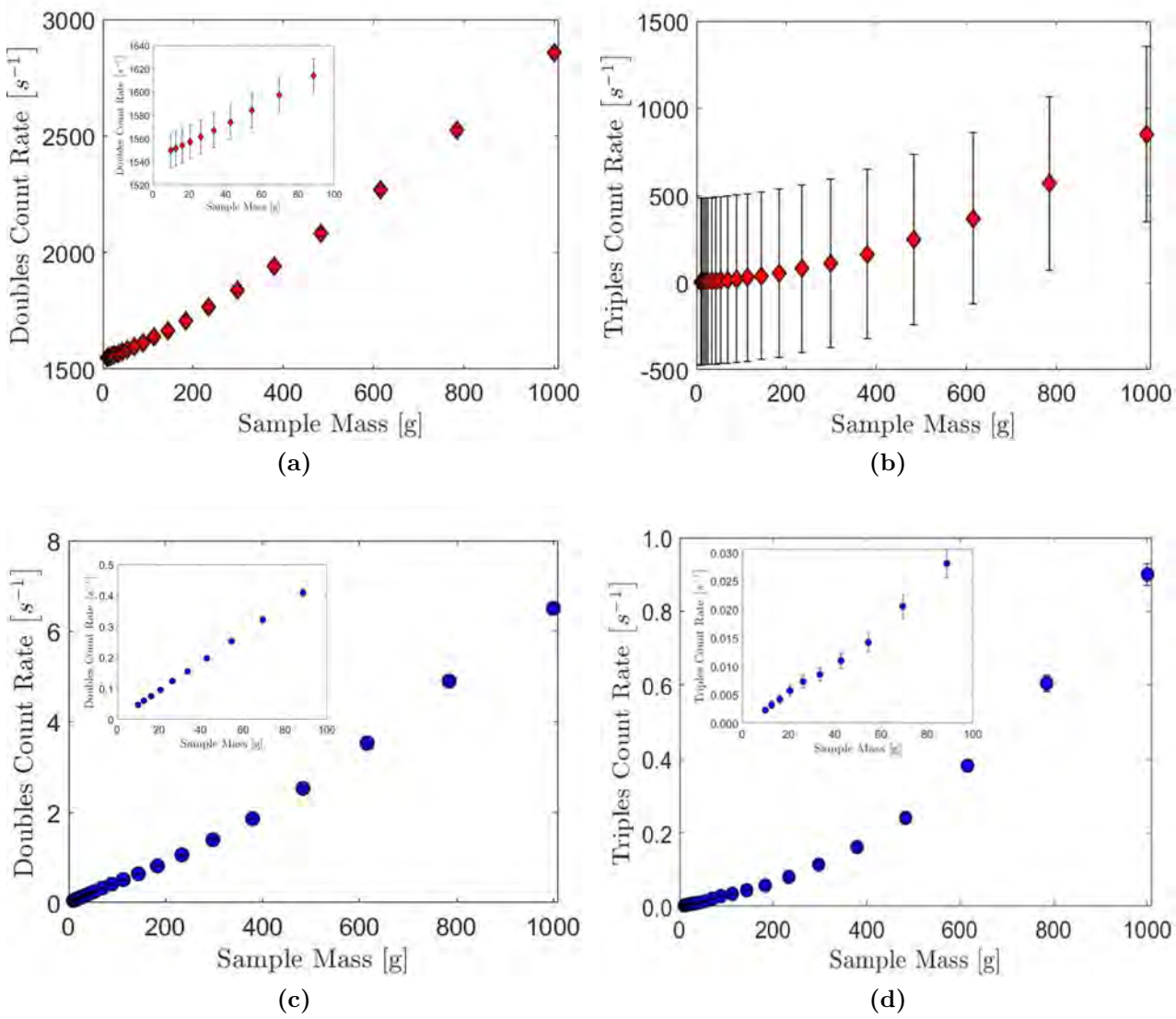

Figure B.4: Neutron doubles and triples multiplicity rate results for the ENMC and OSMC. The doubles and triples multiplicity rates for the ENMC are shown in Figs. B.4a and B.4b, respectively. The doubles and triples multiplicity rates for the OSMC are shown in Figs. B.4c and B.4d, respectively. All insets show the smaller masses, and all error bars are one standard deviation.

B.5.2 Results for the OSMC

The OSMC doubles and triples multiplicity rates with calculated error bars are shown in Figs. B.4c and B.4d, respectively, for a 20-minute measurement.

Similar to the ENMC, the OSMC is capable of doubles rate-based calibration assays. For

a fixed measurement time, the OSMC is able to achieve greater precision in the estimate of D than the ENMC; the error bars are smaller than the markers with the largest being 10% for the 10.0 g sample. The OSMC also achieves greater precision than the ENMC for the estimates of T; as seen in Fig. B.4d, the OSMC is capable of resolving the triples rates between the 10.0 and 12.7 g samples in 20 minutes.

The precisions in D and T demonstrate active neutron multiplicity counting is feasible with the OSMC. To calculate the sample mass, the goal of assays for safeguards applications, the missing component is the coupling term, C. Since the mass is known from the simulation input files, Eqn. (B.7) is used to calculate C, then the (C,M) pairs are fit with Eqn. (B.9). The fit and data are shown in Fig. B.5; the fit parameters are $a = -3.8\times10^{-6}$, $b = 7.6\times10^{-4}$, and $c = -1.9 \times 10^{2}$. The R^2 value for the fit is 0.98 and the RMSE is 4.9×10^{-9}. Note that the fit is specific to a given system and would require measurements with physical standards (or simulations using nuclear data from benchmark experiments) in practice. Errors in the points shown in Fig. B.5 could be due to errors in the nuclear data. The purpose of calculating the fit in this work is solely for demonstration of concept and to show that the fit for ^{237}Np has some similarity to the commonly accepted shape for ^{235}U [114].

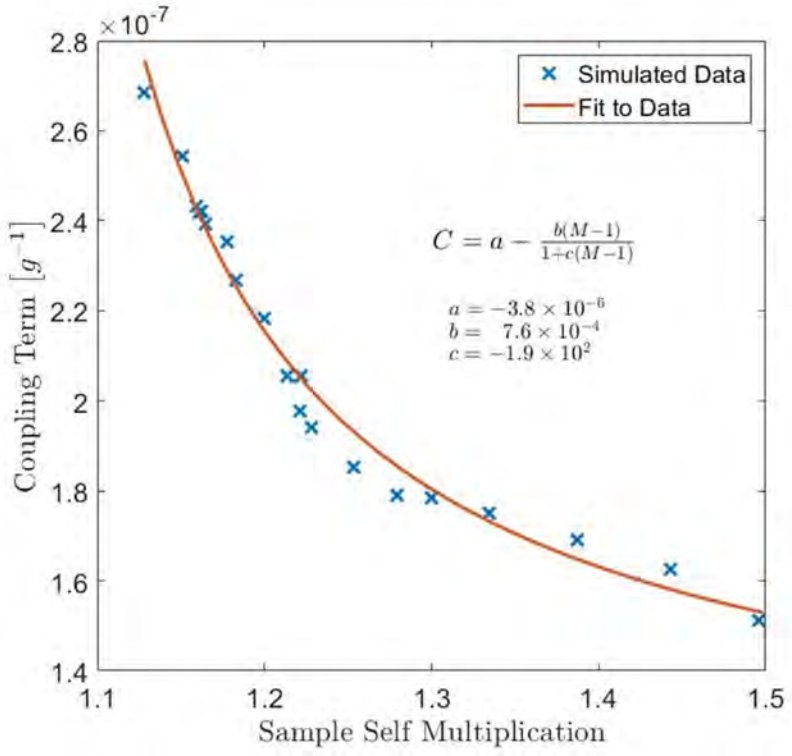

Figure B.5: Coupling term, C, as a function of sample self-multiplication, M, fit with Eqn. (B.9).

B.6 Summary and Conclusions

This work investigates the feasibility of the active nondestructive assay of ^{237}Np using active neutron multiplicity counting. Two measurement systems are compared using Monte Carlo simulations: the flagship ^{3}He-based multiplicity counter – the epithermal neutron multiplicity counter (ENMC) – and an organic scintillator-based multiplicity counter (OSMC). It is shown that, for a fixed measurement time, the OSMC achieves greater precision than the ENMC. The superior precision of the OSMC is expected since the gate width of the OSMC is smaller than that of the ENMC (meaning the OSMC generally has more observation windows or sub-measurements for a fixed measurement time and lower accidentals rate compared to the ENMC). In a 20-minute measurement (per sample), the OSMC resolves the ^{237}Np metal samples (20 masses logarithmically distributed between 10 and 1000 g). To

achieve the same discrimination capabilities, the ENMC requires approximately 6 days of measurement time per sample, where the limiting factor is the precision of the triples multiplicity rate. Taken together, OSMC multiplicity-counting assays are more than 400 times faster than those of the ENMC.

Doubles multiplicity rate-based calibration is another assay modality, which does not rely on the triples rate. In this modality, the OSMC is still faster than the ENMC by a factor of at least 4.5. When both assay modalities are available, doubles calibration is less robust than multiplicity counting since calibration-based assays require a-priori knowledge of the sample. While active neutron multiplicity counting uses the empirically-obtained coupling term, it has been shown that the coupling term is independent of the form factor, sample geometry, mass, and density for uranium samples [114]. Future work includes determining if the coupling term is similarly independent for neptunium samples.

The OSMC offers additional capabilities when compared to the ENMC. One of the capabilities is improved timing characteristics due to the lack of moderating material between the ^{237}Np-fission neutrons and the detectors (which can directly detect fast neutrons) in the OSMC. Another potential capability is independent estimates of the sample self-multiplication by way of neutron anisotropy measurements [56]. Independent estimates of self-multiplication allow more degrees of freedom. Currently, two measured quantities (the neutron double and triple rates) are used to calculate two sample parameters (the neutron self-multiplication and fission rate), while measurement parameters (e.g. efficiency) and nuclear data are assumed/determined from simulation. If the multiplication is determined with different analysis, one of the assumed quantities may be calculated instead of assumed/determined a priori.

B.6.1 Future Work

The simulations and data analysis rely on nuclear data. Future work includes improving the estimates on nuclear data parameters. Furthermore, Fig. B.5 requires validation with

measured standards in multiple form factors (e.g. metal and oxide powder). Los Alamos National Laboratory has begun measurements to improve the nuclear data for ^{237}Np in the Neptunium Subcritical Observation (NeSO), an integral benchmark measurement [125, 126].

Future work also includes decomposing the components of the coupling term, C. One contribution to C present in the OSMC, but not the ENMC is neutron cross talk. In the ENMC, neutrons are detected via capture reactions and are thus removed from the system after detection. In the OSMC, neutrons are detected via scattering reactions and thus remain in the system after a detection. Therefore, a single neutron may deposit energy above threshold in multiple detectors, resulting in multiple detections; this phenomenon is known as neutron cross talk. Corrections for neutron cross talk for passive neutron multiplicity counting were shown by Shin et al. in Ref. [55], and similar corrections could be future work for active neutron multiplicity counting.

Appendix C

Measured Nondestructive Assay of ^{237}Np Using Organic Scintillators and Active Neutron Multiplicity Counting

This appendix is future work to the preceding appendix and presents preliminary measurement comparisons between ^{3}He and organic scintillator systems in the assay of ^{237}Np by active neutron multiplicity counting. The work in this appendix comes from my conference paper "Measured Nondestructive Assay of ^{237}Np Using Organic Scintillators and Active Neutron Multiplicity Counting" a Proceeding of the Institute of Nuclear Materials Management Annual Meeting.

C.1 Introduction and Motivation

The purpose of sample assay for nuclear safeguards is to verify operator-declared masses of nuclear material in noninhibitive measurement times [103, 7]. Nondestructive assay traditionally focuses on special nuclear material; however, ^{237}Np is also a proliferation concern. The United States Department of Energy classifies ^{237}Np as other nuclear material and subjects the isotope to the same safeguards as uranium. It is desirable to investigate detection systems capable of adequately assaying ^{237}Np because 3000 kg are annually produced, the capacity to assay the material is a missing piece of the nuclear nonproliferation and safeguards

toolbox, and typical characteristics that make an isotope unattractive for use in a nuclear weapon (e.g., heat generation and high spontaneous fission rate) are nearly nonexistent for ^{237}Np [127, 105]. Previous simulation work compared currently-deployed ^{3}He systems to an organic-scintillator-based prototype and concluded that the latter system is capable of assaying ^{237}Np, whereas the state-of-the-art ^{3}He systems were incapable in tenable measurement times [127]. The purpose of this work is to confirm the results of the simulation study with measured results.

C.2 Measurement Specifications

The measurement was performed at the National Criticality Experiments Research Center within the Device Assembly Facility. The radiation test object (RTO) in this work is a 6-kg sphere of ^{237}Np, the largest known, single sample of the isotope. The RTO has impurities that are not uniformly distributed throughout the sample due to mass-separation during the cooling process when the sphere was cast. The sprue attached to the sphere was removed and chemical analysis was performed, yielding the biased isotopic composition shown in Tab C.1; note that the weight percentages do not sum to 100% due to uncertainty, although 100% is contained within a 95% confidence interval [128]. The ^{237}Np sphere is reflected by 7.874 cm of nickel; the nickel comprises several nesting hemishells that assemble into a spherical reflector [125, 126]. The ^{237}Np sphere and bottom half of the nickel hemishells are shown in Fig. C.1.

Figure C.1: Photograph of the 6-kg ^{237}Np sphere nested in the bottom half of the nickel hemishells.

Table C.1: Isotopic composition of the 6-kg neptunium sphere.

Isotopes	Weight Percent
^{237}Np	98.8000
^{233}U	0.0035
^{234}U	0.0006
^{235}U	0.0276
^{236}U	0.0002
^{238}U	0.0031
^{238}Pu	0.0016
^{239}Pu	0.0314
^{240}Pu	0.0023
^{241}Pu	0.0001
^{242}Pu	0.0003
^{241}Am	0.0007
^{243}Am	0.1822

Two types of measurement systems are used in this work: the Neutron Multiplicity ^{3}He Array Detector (NoMAD) and a prototype of the Organic Scintillator Array (OSCAR) shown in Figs. C.2 and C.3. The NoMAD detector comprises 15 ^{3}He-gas proportional counters

embedded in a polyethylene matrix having a minimum clock-tick length of 100 ns, a dead time of 1.5 ± 0.3 μs, and a neutron slowing-down-time of 35-40 μs (detailed in benchmark-quality in Ref. [1]). The OSCAR prototype comprises 12, 5.08 cm $\times$ 5.08 cm diameter *trans*-stilbene crystals coupled to photomultiplier tubes [63, 64, 2], suspended in powder-coated iron wire meshes and held in place with porous polyurethane foam [3]. The detectors are powered with high voltage and pulses are digitized with a CAEN v1730 waveform digitizer (16 channels, 500-MHz sampling rate, 14-bit resolution, 2-V dynamic range). Constant fraction discrimination is used to obtain a time-resolution of 1.34$\pm$0.04 ns, the system has negligible dead time, and each detector is calibrated by adjusting the applied voltage while measuring a ^{137}Cs source such that 1.6 V-ns pulse integrals correspond to 0.478 MeVee light output. Two NoMADs and two OSCARs are used in this work; the center-front-faces of each system were 47 cm from the center of the RTO and arranged as shown in Fig. C.4. Note that Fig. C.4 shows tin-copper graded shielding in front of the OSCARs. The shielding was used for measurements of plutonium on the same day and were not removed for the measurement of neptunium. The shields are designed to preferentially shield 60 keV photons from ^{241}Am and have negligible effect on neutron detection and thus the results of this measurement.

Figure C.4 indicates that an AmBe source is used to interrogate the ^{237}Np sphere. Interrogation is needed because the rate of spontaneous fission in ^{237}Np is low. Typically, AmLi sources are used to interrogate ^{235}U samples; however, neutron from AmLi have a mean energy of 0.59 MeV that is lower than the ^{237}Np-induced-fission threshold of 0.8 MeV. Thus AmBe, which has a mean neutron energy of 5.0 MeV and a maximum of approximately 11.0 MeV, is used instead. The OSCARs measured the RTO assembly for 18 minutes, and the NoMADs measured the RTO assembly for 20 minutes (the last 18 minutes of the NoMAD measurements coincide with the time of OSCAR measurements) [103, 127, 113].

Figure C.2: Photograph of the Neutron Multiplicity ^{3}He Array Detector (NoMAD).

Figure C.3: Photograph of the Organic Scintillator Array (OSCAR) prototype.

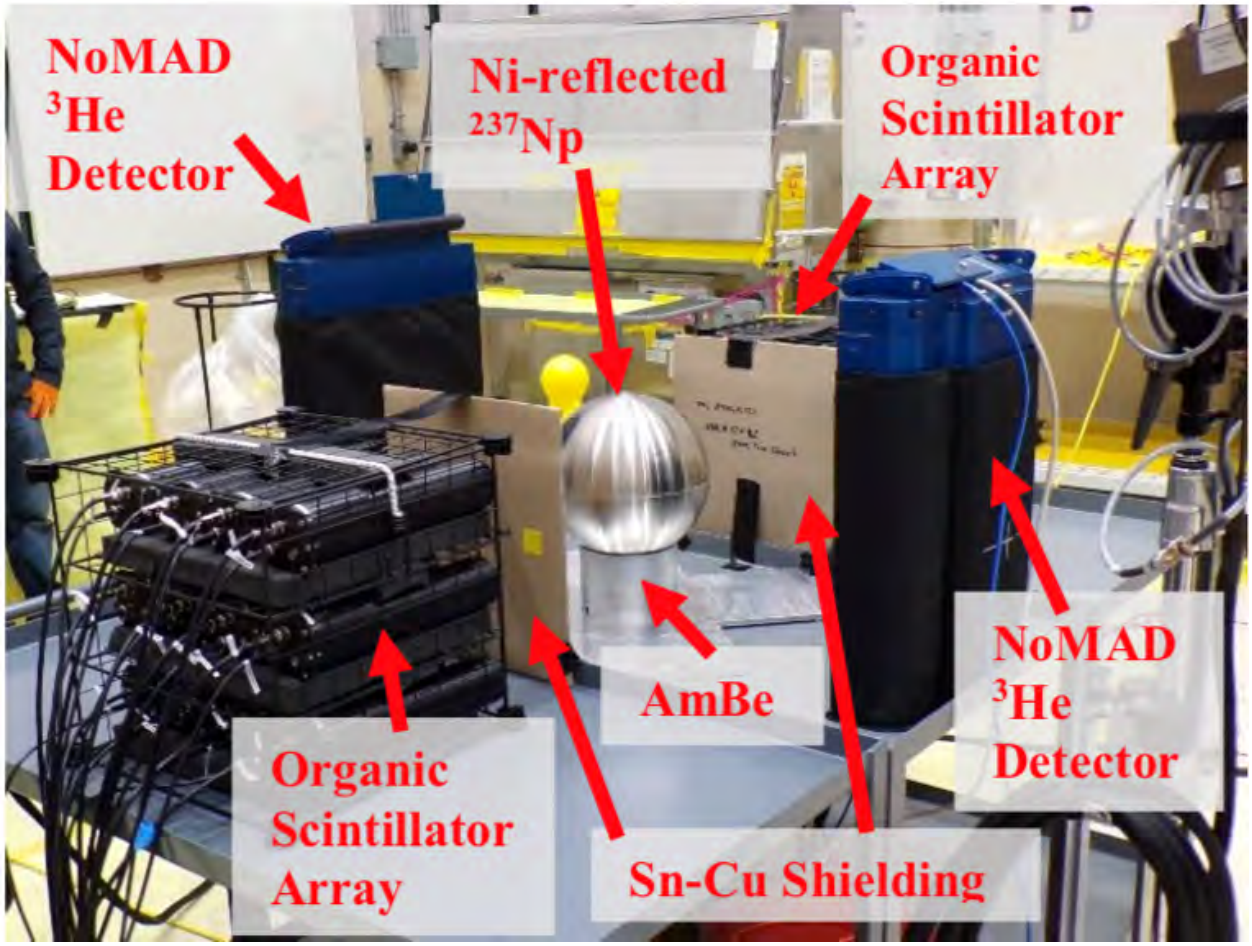

Figure C.4: Annotated photo of the measurement setup of the nickel-reflected, 6-kg ^{237}Np sphere interrogated by AmBe and measured by two NoMAD, ^{3}He detection systems and two OSCAR, organic-scintillator detection systems.

C.3 Data Analysis

List-mode data (sorted lists of neutron detection times) are analyzed with factorial moment counting and random trigger intervals; successive intervals of time are inspected for neutron multiplets, which are converted to the neutron double-multiplicity count rate [93, 102, 104]. The OSCAR uses 100-ns intervals and the NoMAD uses 1-μs intervals based on Fig. 17 in Ref. [129]. In practice, the doubles-multiplicity rate is used with a calibration curve to determine sample mass [114]. Statistical uncertainty is propagated analytically [94]. One of the NoMAD outputs is the list-mode data. After initial data pre-processing, the out-

put of the OSCARs is list-mode data including the total pulse integral and the integral of the pulse tail (24 ns after the pulse peak until the end of the pulse). The integrals are needed to discriminate neutron and photon pulses (since the OSCARs are sensitive to both types of radiation) based on a charge integration technique called pulse shape discrimination (PSD) [71]. The PSD plot for this work is shown in Fig. C.5. The output of the PSD algorithm is list-mode data for neutrons, only. The list-mode data were combined between measurement systems of the same type.

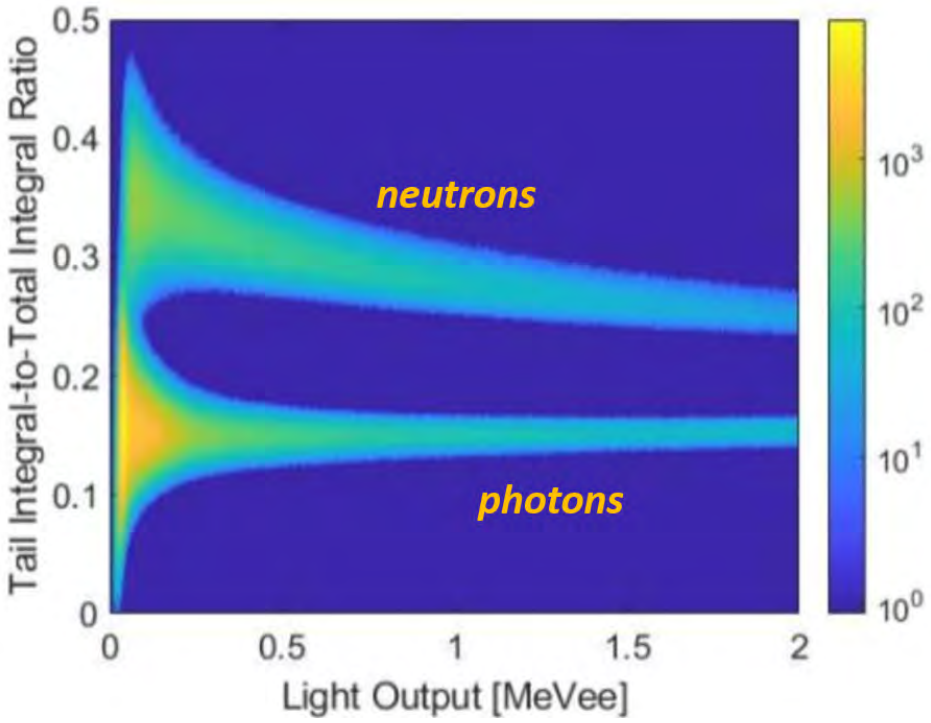

Figure C.5: Pulse shape discrimination plot based on a charge integration technique.

C.4 Results and Discussion

The relative uncertainty was calculated based on the double-multiplicity rate and associated uncertainty for each type of measurement system as a function of measurement time. The results are shown in Fig. C.6. It is observed that the uncertainty decreases as

(measurement time)$^{-1/2}$; the organic scintillator data is fit by

$$(\text{Relative Uncertainty})_{\text{OSCAR}} = 2.131(\text{measurement time})^{-0.5}, \tag{C.1}$$

whereas the ^{3}He data is fit by

$$(\text{Relative Uncertainty})_{\text{NoMAD}} = 53.58(\text{measurement time})^{-0.5}. \tag{C.2}$$

The unit for relative uncertainty is percent and the unit for measurement time is minute in Eqns (C.1) and (C.2). Interpolating for the OSCAR and extrapolating for the NoMAD, the OSCAR requires 4.54 minutes to attain 1% relative uncertainty while the NoMAD requires approximately 2 days to achieve the same. Extrapolating for both systems, the OSCAR requires 2.72 seconds to attain 10% relative uncertainty while the NoMAD requires approximately 28.7 minutes to achieve the same. Solving Eqns (C.1) and (C.2) shows that the NoMAD requires a measurement time 632 times longer than the OSCAR.

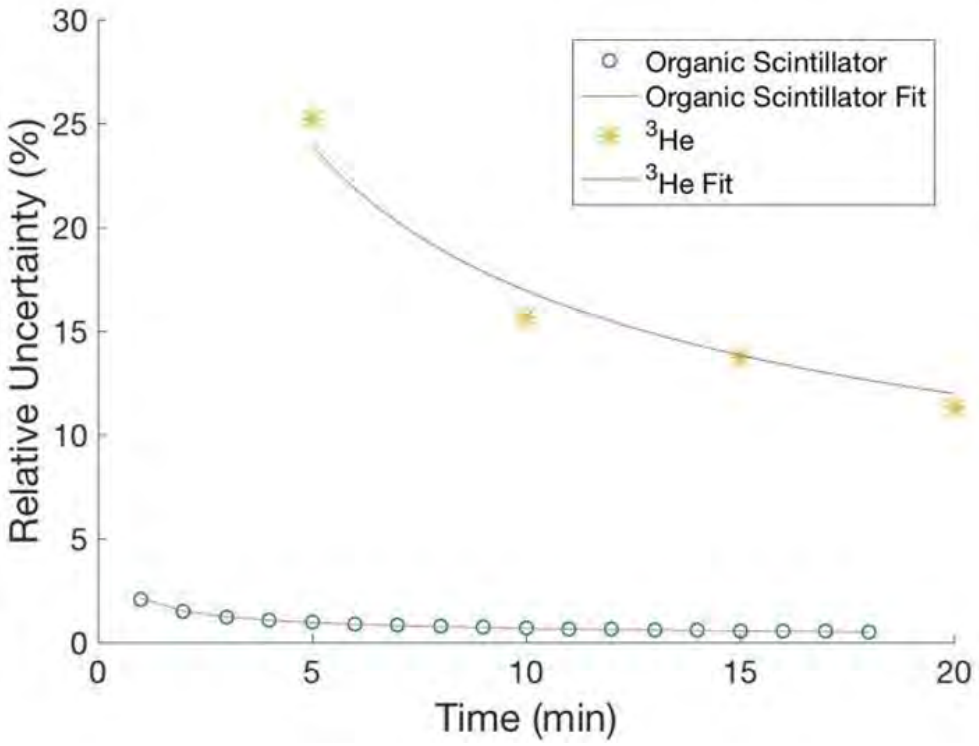

Figure C.6: Relative uncertainty as a function of measurement time for the NoMAD, ^{3}He system and the OSCAR, organic scintillator system.

Note that the uncertainty shown is for statistical uncertainty, only. Although the NoMAD has greater neutron detection efficiency (13.7 times more based on total neutron counts) than the OSCAR, the total number of inspection intervals/gates is less by four orders of magnitude because the same measurement time is divided by a much larger interval. The shorter time intervals of the OSCAR are due to the negligible dead time and because time-correlated neutrons are not temporally smeared in moderating material such as the polyethylene in the NoMAD.

A potential source of nonstatistical uncertainty in the OSCAR system is particle misclassification (e.g., classifying a photon as neutron) and neutron crosstalk (a single neutron rendering multiple detections, though this phenomena has been analytically addressed in Ref. [55]). A source of uncertainty for both detection systems is the chemical makeup of the RTO. Due to the nonuniform distribution of impurities, it is believed that Tab. C.1 is incom-

prehensive and notably omits curium [126]. Curium has a specific spontaneous fission rate, therein emitting neutron multiplets that are misattributed to the neptunium. Los Alamos National Laboratory has plans to perform further chemical analysis.

The beryllium in the AmBe interrogation source has a cross section for (n,2n) interactions, which was observed in previous work [127]. This correlated signal from AmBe could dominate the desired signal from neptunium from smaller samples and uncertainty in this double rate could define a nonzero, asymptotic uncertainty. In the former case, higher-order multiplicity rates (such as the triples rate) could be used; however, longer measurement times would be required to attain the same precision as the doubles rate.

C.5 Conclusions

The ^{3}He-based NoMAD and organic-scintillator-based OSCAR detection systems, which are similar in form factor, are compared in their capacity to assay a 6-kg sphere of ^{237}Np by way of multiplicity counting. The systems are principally compared on precision and the time it takes to achieve the same relative uncertainty in the double-multiplicity count rate; the NoMAD is 632 times slower than the OSCAR. Besides relative comparisons, the OSCAR can achieve excellent precision in under five minutes and moderate precision in under three seconds, making the prototype highly reasonable for field deployment. The reduced measurement times will, for example, enable inspectors to inspect more samples in lieu of randomly selecting a hopefully representative subset. Reduced measurement times will also reduce procedural and operational costs. Thus, it is recommended that organic-scintillator-based systems be considered as upgrades to currently deployed ^{3}He systems.

The OSCAR prototype has not been optimized for efficiency, yet the rapid-assay capability lends the system to applications beyond verification of operator-declared masses. For example, the OSCAR could be reconfigured to affix to a pipe and assay moving material as it passes, depending on the mass flow rate. Future work includes simulated studies of pipe-monitoring applications, efficiency optimizations, and testing in field-like conditions.

BIBLIOGRAPHY

BIBLIOGRAPHY

[1] J. HUTCHINSON, R. BAHRAN, T. CUTLER, J. ARTHUR, and M. NELSON, "Subcritical Copper-Reflected alpha-phase Plutonium (SCRaP) Measurements and Simulations," *M&C 2017 - International Conference on Mathematics & Computational Methods Applied to Nuclear Science & Engineering* (2017).

[2] T. H. SHIN, P. L. FENG, J. S. CARLSON, S. D. CLARKE, and S. A. POZZI, "Measured neutron light-output response for trans-stilbene and small-molecule organic glass scintillators," *Nuclear Instruments and Methods in Physics Research Section A: Accelerators, Spectrometers, Detectors and Associated Equipment* (2019).

[3] M. Y. HUA, C. A. BRAVO, A. T. MACDONALD, J. D. HUTCHINSON, G. E. MCKENZIE, B. C. KIEDROWSKI, S. D. CLARKE, and S. A. POZZI, "Rossi-alpha measurements of fast plutonium metal assemblies using organic scintillators," *Nuclear Instruments and Methods in Physics Research Section A: Accelerators, Spectrometers, Detectors and Associated Equipment*, **959**, 163507 (2020).

[4] G. E. HANSEN, "The Rossi alpha method," *Los Alamos National Laboratory, Technical Report*, , *LA-UR-85-4176* (8 1985).

[5] J. GODA, T. CUTLER, T. GROVE, J. HUTCHINSON, G. MCKENZIE, A. MCSPADEN, M. NELSON, and R. SANCHEZ, "Comparison of Methods for Determining Multiplication in Subcritical Configurations of a Plutonium System," *Proceedings of the PHYSOR Conference* (2018).

[6] M. Y. HUA, F. B. DARBY, J. D. HUTCHINSON, G. E. MCKENZIE, S. D. CLARKE, and S. A. POZZI, "Validation of the two-region Rossi-alpha model for reflected assemblies," *Nuclear Instruments and Methods in Physics Research Section A: Accelerators, Spectrometers, Detectors and Associated Equipment*, **981**, 164535 (2020).

[7] "Nuclear Safeguards, Security, and Nonproliferation," in J. E. DOYLE, editor, "Nuclear Safeguards, Security, and Nonproliferation," Butterworth-Heinemann, Boston, 2nd ed. (2019).

[8] H. KISSINGER, *Nuclear Weapons and Foreign Policy*, Books that live, W. W. Norton (1969).

[9] F. CHEN, *An Indispensable Truth: How Fusion Power Can Save the Planet*, Springer New York (2011).

[10] J. CHADWICK, "The existence of a neutron," *Proceedings of the Royal Society A: Mathematical, Physical, and Engineering Sciences*, **136**, *830*, 410 – 421 (1932).

[11] E. FERMI, E. AMALDI, O. AGOSTINO, F. RASETTI, and E. SEGRE, "Artificial radioactivity produced by neutron bombardment," *Proceedings of the Royal Society A: Mathematical, Physical, and Engineering Sciences*, **146**, *857* (1934).

[12] I. NODDACK, "Uber das Element 93," *Angewandte Chemie*, **47**, *653* (1934).

[13] O. HAHN and F. STRASSMANN, "Ubergang von Sterinen in aromatische Verbindungen. III. Mitteilung: Aromatisierung des Δ1, 2; 4, 5-Cholestadienons-3," *Naturwissenschaften*, **26**, *756* (1938).

[14] O. HAHN and F. STRASSMANN, "Uber den Nachweis und das Verhalten der bei der Bestrahlung des Urans mittels Neutronen entstehenden Erdalkalimetalle," *Die Naturwissenschaften*, **27**, *1* (1939).

[15] L. MEITNER and O. R. FRISCH, "Products of the Fission of the Uranium Nucleus," *Nature*, **143** (1939).

[16] E. FERMI, "Development of the First Chain Reacting Pile," *Proceedings of the American Philosophical Society*, **22** (1946).

[17] T. MCLAUGHLIN, S. MONAHAN, N. PRUVOST, V. FROLOV, B. RYAZANOV, and V. SVIRIDOV, "A review of Criticality Accidents," *Los Alamos National Laboratory Report*, **LA-13638**, *2000 Revision* (2000).

[18] R. UHRIG and U. A. E. COMMISSION, *Random noise techniques in nuclear reactor systems*, Ronald Press (1970).

[19] "Neutron Fluctuations," in I. PÁZSIT and L. PÁL, editors, "Neutron Fluctuations," Elsevier, Amsterdam, p. vi (2008).

[20] J. ORNDOFF, "Prompt Neutron Periods of Metal Critical Assemblies," *Nuclear Science and Engineering*, **2**, *4*, 450–460 (7 1957).

[21] R. FEYNMAN, F. DEHOFFMANN, and R. SERBER, "Dispersion of the neutron emission in U-235 fission," **3**, 64–69 (08 1956).

[22] R. FEYNMAN, F. DEHOFFMANN, and R. SERBER, "Statistical Fluctuations in the Water Boiler and the Dispersion of Neutrons Emitted per Fission," *LA-101, Los Alamos National Laboratory* (1944).

[23] R. FEYNMAN, F. DEHOFFMAN, and R. SERBER, "Intensity Fluctuations of a Neutron Chain Reactor," *LADC-256, Los Alamos National Laboratory* (1944).

[24] R. FEYNMAN, F. D. HOFFMANN, and R. SERBER, "Dispersion of the neutron emission in U-235 fission," *Journal of Nuclear Energy (1954)*, **3**, *1*, 64 – IN10 (1956).

[25] J. T. MIHALCZO, "The Use of Californium-252 as a Randomly Pulsed Neutron Source for Prompt-Neutron Decay Measurements," *Nuclear Science and Engineering*, **53**, *4*, 393–414 (1974).

[26] J. MIHALCZO, "Prompt alpha and reactivity measurements on fast metal assemblies," *Progress in Nuclear Energy*, **1**, *1*, 1 – 26 (1977).

[27] G. J. ARNONE, G. S. BRUNSON, and K. L. COOP, "A pulse arrival-time recording module for analyzing neutron multiplicities," in "IEEE Conference on Nuclear Science Symposium and Medical Imaging," (1992), pp. 369–371 vol.1.

[28] R. KURAMOTO, A. DOS SANTOS, R. JEREZ, R. DINIZ, U. BITELLI, T. MADI FILHO, and C. LUIS VENEZIANI, "Rossi-α Experiment in the IPEN/MB-01 Research Reactor: Validation of Two-Region Model and Absolute Measurement of β_{eff} and Λ," **2006** (01 2006).

[29] J. HUTCHINSON, G. MCKENZIE, J. ARTHUR, M. NELSON, and W. MONAGE, "Prompt Neutron Decay Constant Fitting Using the Rossi-alpha and Feynman Variance-to-Mean Methods," *Transactions of the American Nuclear Society*, **117**, 986–989 (2017).

[30] D. CHERNIKOVA, W. ZIGUAN, I. PÁZSIT, and L. PÁL, "A general analytical solution for the variance-to-mean Feynman-alpha formulas for a two-group two-point, a two-group one-point and a one-group two-point cases," *European Physical Journal Plus*, **129**, *11*, 1–27 (2014).

[31] M. MONTERIAL, P. MARLEAU, and S. POZZI, "Characterizing subcritical assemblies with time of flight fixed by energy estimation distributions," *Nuclear Instruments and Methods in Physics Research Section A: Accelerators, Spectrometers, Detectors and Associated Equipment*, **888**, 240 – 249 (2018).

[32] R. AVERY, "Coupled Fast-Thermal Power Breeder," *Nuclear Science and Engineering*, **3**, *2*, 129–144 (1958).

[33] C. E. COHN, "Reflected-Reactor Kinetics," *Nuclear Science and Engineering*, **13**, *1*, 12–17 (1962).

[34] G. MCKENZIE, *Limits on Subcritical Reactivity Determination using Rossi-α and Related Methods*, Ph.D. thesis, University of Illinois (2018).

[35] T. ENDO and A. YAMAMOTO, "Comparison of theoretical formulae and bootstrap method for statistical error estimation of Feynman-α method," *Annals of Nuclear Energy*, **124**, 606 – 615 (2019).

[36] C. WAGEMANS, *The Nuclear Fission Process* (09 1991).

[37] S. MARIN, V. A. PROTOPOPESCU, R. VOGT, M. J. MARCATH, S. OKAR, M. Y. HUA, P. TALOU, P. F. SCHUSTER, S. D. CLARKE, and S. A. POZZI, "Event-by-event neutron–photon multiplicity correlations in 252Cf(sf)," *Nuclear Instruments*

and Methods in Physics Research Section A: Accelerators, Spectrometers, Detectors and Associated Equipment, **968**, 163907 (2020).

[38] I. PERCEL, *A quantum measurement model of reaction-transport systems*, Ph.D. thesis, University of Illinois (2018).

[39] K. HOFFMAN and R. KUNZE, *Linear Algebra*, Featured Titles for Linear Algebra (Advanced) Series, Prentice-Hall (1971).

[40] G. BELL and S. GLASSTONE, *Nuclear Reactor Theory*, Van Nostrand Reinhold Company (1970).

[41] E. E. LEWIS and W. F. MILLER, "Computational methods of neutron transport," .

[42] G. KEEPIN, *Physics of nuclear kinetics*, Addison-Wesley series in nuclear science and engineering, Addison-Wesley Pub. Co. (1965).

[43] K. OTT and R. NEUHOLD, *Introductory Nuclear Reactor Dynamics*, American Nuclear Society (1985).

[44] C. P. BAKER, "Time scale measurements by the Rossi method," , *LA-617*.

[45] P. THOMAS, "21 - Nuclear reactors," in P. THOMAS, editor, "Simulation of Industrial Processes for Control Engineers," Butterworth-Heinemann, Oxford, pp. 268 – 281 (1999).

[46] W. J. PATERSON and J. W. WEALE, "Pulsed Source Methods in Fast Reactor Physics," *Journal of British Nuclear Energy Society*, **3**, *4* (1964).

[47] J. W. WEALE and ET AL., "Measurements of the Prompt Neutron Decay Constant of the VERA Reactor Using the Prompt Source Method," *IAEA Proceedings of the Symposium on Pulsed Neutron Research*, **2**, *STI/PUB/104* (1965).

[48] G. S. BRUNSON, "On the Possible Connection Between the Central Worth Discrepancy and the Dollar Discrepancy," *Nuclear Instruments and Methods*, **125**, *139* (1975).

[49] G. D. SPRIGGS, R. D. BUSCH, and J. G. WILLIAMS, "Two-region kinetic model for reflected reactors," *Annals of Nuclear Energy*, **24**, *3*, 205 – 250 (1997).

[50] C. J. WERNER, J. S. BULL, C. J. SOLOMON, F. B. BROWN, G. W. MCKINNEY, M. E. RISING, D. A. DIXON, R. L. MARTZ, H. G. HUGHES, L. J. COX, A. J. ZUKAITIS, J. C. ARMSTRONG, R. A. FORSTER, and L. CASSWELL, "MCNP Version 6.2 Release Notes," .

[51] T. GOORLEY, M. JAMES, T. BOOTH, F. BROWN, J. BULL, L. J. COX, J. DURKEE, J. ELSON, M. FENSIN, R. A. FORSTER, J. HENDRICKS, H. G. HUGHES, R. JOHNS, B. KIEDROWSKI, R. MARTZ, S. MASHNIK, G. MCKINNEY, D. PELOWITZ, R. PRAEL, J. SWEEZY, L. WATERS, T. WILCOX, and T. ZUKAITIS, "Initial MCNP6 Release Overview," *Nuclear Technology*, **180**, *3*, 298–315 (2012).

[52] S. A. POZZI, E. PADOVANI, and M. MARSEGUERRA, "MCNP-PoliMi: a Monte-Carlo code for correlation measurements," *Nuclear Instruments and Methods in Physics Research Section A: Accelerators, Spectrometers, Detectors and Associated Equipment*, **513**, *3*, 550 – 558 (2003).

[53] R. MOSTELLER, "Validation suites for MCNP," *Los Alamos National Laboratory Report*, **LA-IR-02-0878** (2002).

[54] W. M. STEINBERGER, M. L. RUCH, N. GIHA, A. D. FULVIO, P. MARLEAU, S. D. CLARKE, and S. A. POZZI, "Imaging Special Nuclear Material using a Handheld Dual Particle Imager," *Scientific Reports*, **10** (2020).

[55] T. H. SHIN, M. Y. HUA, M. J. MARCATH, D. L. CHICHESTER, I. PÁZSIT, A. D. FULVIO, S. D. CLARKE, and S. A. POZZI, "Neutron Multiplicity Counting Moments for Fissile Mass Estimation in Scatter-Based Neutron Detection Systems," *Nuclear Science and Engineering*, **188**, *3*, 246–269 (2017).

[56] T. H. SHIN, C. A. BRAVO, J. MARLOW, W. GEIST, S. D. CLARKE, and S. A. POZZI, "Neutron-neutron angular and energy-angle correlations of plutonium samples with varying α-ratio," *Nuclear Instruments and Methods in Physics Research Section A: Accelerators, Spectrometers, Detectors and Associated Equipment*, p. 162297 (2019).

[57] S. D. CLARKE, M. C. HAMEL, A. DI FULVIO, and S. A. POZZI, "Neutron and gamma-ray energy reconstruction for characterization of special nuclear material," *Nuclear Engineering and Technology*, **49**, *6*, 1354 – 1357 (2017).

[58] M. HUA, C. BRAVO, A. MACDONALD, J. HUTCHINSON, G. MCKENZIE, T. GROVE, J. GODA, A. MCSPADEN, S. CLARKE, and S. POZZI, "Fast Rossi-alpha Measurements of Plutonium using Organic Scintillators," *Transactions of the PHYSOR 2020 Meeting* (2020).

[59] W. STEINBERGER, M. RUCH, A. DI-FULVIO, S. CLARKE, and S. POZZI, "Timing performance of organic scintillators coupled to silicon photomultipliers," *Nuclear Instruments and Methods in Physics Research Section A: Accelerators, Spectrometers, Detectors and Associated Equipment*, **922**, 185 – 192 (2019).

[60] G. KNOLL, *Radiation Detection and Measurement*, Wiley (2000).

[61] J. BIRKS, *The Theory and Practice of Scintillation Counting*, Pergamon (1964).

[62] F. BROOKS, "Development of organic scintillators," *Nuclear Instruments and Methods*, **162**, *1*, 477 – 505 (1979).

[63] N. ZAITSEVA, A. GLENN, L. CARMAN, H. P. MARTINEZ, R. HATARIK, H. KLAPPER, and S. PAYNE, "Scintillation properties of solution-grown trans-stilbene single crystals," *Nuclear Instruments and Methods in Physics Research Section A: Accelerators, Spectrometers, Detectors and Associated Equipment*, **789**, 8 – 15 (2015).

[64] M. BOURNE, S. CLARKE, N. ADAMOWICZ, S. POZZI, N. ZAITSEVA, and L. CARMAN, "Neutron detection in a high-gamma field using solution-grown stilbene," *Nuclear Instruments and Methods in Physics Research Section A: Accelerators, Spectrometers, Detectors and Associated Equipment*, **806**, 348 – 355 (2016).

[65] M. A. NORSWORTHY, A. POITRASSON-RIVIÈRE, M. L. RUCH, S. D. CLARKE, and S. A. POZZI, "Evaluation of neutron light output response functions in EJ-309 organic scintillators," *Nuclear Instruments and Methods in Physics Research Section A: Accelerators, Spectrometers, Detectors and Associated Equipment*, **842**, 20 – 27 (2017).

[66] M. NELSON, B. ROONEY, D. DINWIDDIE, and G. BRUNSON, "Analysis of digital timing methods with BaF2 scintillators," *Nuclear Instruments and Methods in Physics Research, Section A: Accelerators, Spectrometers, Detectors and Associated Equipment*, **505**, *1-2*, 324–327 (2003), cited By 41.

[67] C. FU, A. DI FULVIO, S. CLARKE, D. WENTZLOFF, S. POZZI, and H. KIM, "Artificial neural network algorithms for pulse shape discrimination and recovery of piled-up pulses in organic scintillators," *Annals of Nuclear Energy*, **120**, 410 – 421 (2018).

[68] A. J. JINIA, T. E. MAURER, K. E. LAFERTY, S. D. CLARKE, H. S. KIM, D. D. WENTZLOFF, and S. A. POZZI, "Development an Artificial Neural Network for Special Nuclear Material Detection in a Mixed Photon-Neutron Environment," *Proceedings of the IEEE NSS MIC Meeting* (2020).

[69] F. BROOKS, "A scintillation counter with neutron and gamma-ray discriminators," *Nuclear Instruments and Methods*, **4**, *3*, 151 – 163 (1959).

[70] L. F. MILLER, J. PRESTON, S. POZZI, M. FLASKA, and J. NEAL, "Digital pulse shape discrimination," *Radiation Protection Dosimetry*, **126**, *1-4*, 253–255 (06 2007).

[71] J. POLACK, M. FLASKA, A. ENQVIST, C. SOSA, C. LAWRENCE, and S. POZZI, "An algorithm for charge-integration, pulse-shape discrimination and estimation of neutron/photon misclassification in organic scintillators," *Nuclear Instruments and Methods in Physics Research Section A: Accelerators, Spectrometers, Detectors and Associated Equipment*, **795**, 253 – 267 (2015).

[72] M. Y. HUA, J. D. HUTCHINSON, G. E. MCKENZIE, T. H. SHIN, S. D. CLARKE, and S. A. POZZI, "Derivation of the Two-Exponential Probability Density Function for Rossi-Alpha Measurements of Reflected Assemblies and Validation for the Special Case of Shielded Measurements," *Nuclear Science and Engineering*, **194**, *1*, 56–68 (2020).

[73] M. Y. HUA, J. D. HUTCHINSON, G. E. MCKENZIE, B. C. KIEDROWSKI, M. W. LIEMOHN, S. D. CLARKE, and S. A. POZZI, "Measurement uncertainty of rossi-alpha neutron experiments," *Annals of Nuclear Energy*, **147**, 107672 (2020).

[74] S. CROFT, A. FAVALLI, D. HAUCK, D. HENZLOVA, and P. SANTI, "Feynman variance-to-mean in the context of passive neutron coincidence counting," *Nuclear Instruments and Methods in Physics Research Section A: Accelerators, Spectrometers, Detectors and Associated Equipment*, **686**, 136–144 (09 2012).

[75] T. SHIN, J. HUTCHINSON, R. BAHRAN, and S. POZZI, "A Note on the Nomenclature in Neutron Multiplicity Mathematics," *Nuclear Science and Engineering*, pp. 1–17 (02 2019).

[76] R. A. KARAM, "Measurements of Rossi-Alpha in Reflected Ractors," *In: Transactions of the American Nuclear Society*, **7**, 283 (1964).

[77] M. Y. HUA, J. D. HUTCHINSON, G. E. MCKENZIE, and M. A. NELSON, "2-Exponential PDF and Analytic Uncertainty Approximations for Rossi-alpha Histograms," *Transactions of the American Nuclear Society*, **119**, 801–804 (11 2018).

[78] D. ALBRITTON, A. SCHMELTEKOPF, and R. ZARE, "An Introduction to the Least-Squares Fitting of Spectroscopic Data," p. 1 (01 1976).

[79] A. PAPOULIS, *Probability, random variables, and stochastic processes*, McGraw-Hill, New York (1984).

[80] J. MATTINGLY, "Polyethylene-reflected plutonium metal sphere: subcritical neutron and gamma measurements." (11 2009).

[81] E. MILLER, B. DENNIS, S. CLARKE, S. POZZI, and J. MATTINGLY, "Simulation of polyethylene-moderated plutonium neutron multiplicity measurements," *Nuclear Instruments and Methods in Physics Research Section A: Accelerators, Spectrometers, Detectors and Associated Equipment*, **652**, *1*, 540 – 543 (2011), symposium on Radiation Measurements and Applications (SORMA) XII 2010.

[82] B. RICHARD and J. HUTCHINSON, "Nickel Reflected Plutonium Metal Sphere Subcritical Measurements," *In: International Handbook of Evaluated Criticality Safety Benchmark Experiments*, **[DVD]/Nuclear Energy Agency. - Paris : OECD Nuclear Energy Agency** (2016), (NEA;7328).

[83] B. RICHARD and J. HUTCHINSON, "Tungsten-Reflected Plutonium-Metal-Sphere Subcritical Measurements," *In: International Handbook of Evaluated Criticality Safety Benchmark Experiments*, **[DVD]/Nuclear Energy Agency. - Paris : OECD Nuclear Energy Agency** (2016), (NEA;7328).

[84] R. ROTHE, "Extrapolated experimental critical parameters of unreflected and steel-reflected massive enriched uranium metal spherical and hemispherical assemblies," , *INEEL/EXT–97-01401*.

[85] J. BESS and J. HUTCHINSON, "Benchmark Analysis of Subcritical Noise Measurements on a Nickel-Reflected Plutonium Metal Sphere," (01 2009).

[86] A. T. MCSPADEN, T. E. CUTLER, J. D. HUTCHINSON, and G. E. MCKENZIE, "Finalization of the IER 488 (MUSiC) Experiment Design," *Nuclear Criticality Safety Program (NCSP) Technical Program Review* (3 2019).

[87] R. A. WELDON, T. E. CUTLER, J. D. HUTCHINSON, W. L. MYERS, G. E. MCKENZIE, A. T. MCSPADEN, and R. G. SANCHEZ, "Application of the Rossi-alpha method to simulations of HEU and organic scintillators," *Transactions of the American Nuclear Society* (11 2020).

[88] M. Y. HUA, J. D. HUTCHINSON, G. E. MCKENZIE, S. D. CLARKE, and S. A. POZZI, "On the Feynman-alpha method for reflected fissile assemblies," *Annals of Nuclear Energy*, **XXX**, XXXXXX (Submitted Nov 2020).

[89] J.-L. MUÑOZ-COBO, C. BERGLÖF, J. PEÑA, D. VILLAMARÍN, and V. BOURNOS, "Feynman-α and Rossi-α formulas with spatial and modal effects," *Annals of Nuclear Energy*, **38**, *2*, 590 – 600 (2011).

[90] R. SOULE, W. ASSAL, P. CHAUSSONNET, C. DESTOUCHES, C. DOMERGUE, C. JAMMES, J.-M. LAURENS, J.-F. LEBRAT, F. MELLIER, G. PERRET, G. RIMPAULT, H. SERVIÈRE, G. IMEL, G. M. THOMAS, D. VILLAMARIN, E. GONZALEZ-ROMERO, M. PLASCHY, R. CHAWLA, J. L. KLOOSTER, Y. RUGAMA, A. BILLEBAUD, R. BRISSOT, D. HEUER, M. KERVENO, C. L. BRUN, E. LIATARD, J.-M. LOISEAUX, O. MÉPLAN, E. MERLE, F. PERDU, J. VOLLAIRE, and P. BAETEN, "Neutronic Studies in Support of Accelerator-Driven Systems: The MUSE Experiments in the MASURCA Facility," *Nuclear Science and Engineering*, **148**, *1*, 124–152 (2004).

[91] S. DEGWEKER and R. RUDRA, "On the relation between Rossi alpha and Feynman alpha methods," *Annals of Nuclear Energy*, **94**, 433 – 439 (2016).

[92] M. Y. HUA, C. A. BRAVO, R. M. MARCHIE, J. D. HUTCHINSON, G. E. MCKENZIE, and S. A. POZZI, "Rossi-alpha Uncertainty Quantification by Analytic, Bootstrap, and Sample Methods to Inform Fitting Best Practices," *Transactions of the ANS Winter Meeting* (2020).

[93] W. HAGE and D. CIFARELLI, "On the factorial moments of the neutron multiplicity distribution of fission cascades," *Nuclear Instruments and Methods in Physics Research Section A: Accelerators, Spectrometers, Detectors and Associated Equipment*, **236**, *1*, 165 – 177 (1985).

[94] J. HUTCHINSON, M. NELSON, T. GROVE, J. ARTHUR, G. MCKENZIE, R. BAHRAN, and T. CUTLER, "Validation of statistical uncertainties in subcritical benchmark measurements: Part I – Theory and simulations," *Annals of Nuclear Energy*, **125**, 50 – 62 (2019).

[95] M. PRASAD, N. SNYDERMAN, and J. VERBEKE, "Analytical error bars and RSD for neutron multiplicity counting," *Nuclear Instruments and Methods in Physics Research Section A: Accelerators, Spectrometers, Detectors and Associated Equipment*, **903**, 25 – 31 (2018).

[96] S. WALSTON, J. BURCH, M. COWAN, G. GUETHLEIN, G. KEEFER, P. KERR, D. MCAVOY, L. NAKAE, M. PRASAD, D. PUGH, G. SLAVIK, and N. SNYDERMAN, "Benchmark Measurements of the BeRP Ball in Various Reflectors," .

[97] S. M. MCCONCHIE and J. T. MIHALCZO, "Prompt neutron decay constant from Feynman variance fitting," , *April* (2014).

[98] D. CHERNIKOVA, K. AXELL, S. AVDIC, I. PÁZSIT, A. NORDLUND, and S. ALLARD, "The neutron-gamma Feynman variance to mean approach: Gamma detection and total neutron-gamma detection (theory and practice)," *Nuclear Instruments and Methods in Physics Research, Section A: Accelerators, Spectrometers, Detectors and Associated Equipment*, **782**, 47–55 (2015).

[99] R. A. SOLTZ, A. DANAGOULIAN, E. P. HARTOUNI, M. S. JOHNSON, S. A. SHEETS, A. GLENN, S. E. KORBLY, and R. J. LEDOUX, "Fissile material detection using neutron time-correlations from photofission," *AIP Advances*, **9**, *2*, 1–15 (2019).

[100] J. VERBEKE, A. GLENN, G. KEEFER, and R. WURTZ, "Method for measuring multiple scattering corrections between liquid scintillators," *Nuclear Instruments and Methods in Physics Research Section A: Accelerators, Spectrometers, Detectors and Associated Equipment*, **825**, 69 – 77 (2016).

[101] M. Y. HUA, J. D. HUTCHINSON, G. E. MCKENZIE, and M. A. NELSON, "2-Exponential PDF and Analytic Uncertainty Approximations for Rossi-alpha Histograms," *Transactions of the ANS Winter Meeting* (2018).

[102] D. CIFARELLI and W. HAGE, "Models for a three-parameter analysis of neutron signal correlation measurements for fissile material assay," *Nuclear Instruments and Methods in Physics Research Section A: Accelerators, Spectrometers, Detectors and Associated Equipment*, **251**, *3*, 550 – 563 (1986).

[103] D. REILLY, N. ENSSLIN, and H. SMITH, *Passive Nondestructive Assay of Nuclear Materials*, National Technical Information Service (1991).

[104] D. G. LANGNER, J. E. STEWART, M. M. PICKRELL, M. S. KRICK, N. ENSSLIN, and W. C. HARKER, "Application Guide to Neutron Multiplicity Counting," .

[105] B. GODDARD, A. SOLODOV, and V. FEDCHENKO, "IAEA "significant quantity" values: time for a closer look?" *The Nonproliferation Review*, **23**, *5-6*, 677–689 (2016).

[106] DOE, "Manual for Control and Accountability of Nuclear Materials," , *DOE M 474.1-1B* (2003).

[107] DOE, "Draft Environmental Impact Statement for the Proposed Consolidation of Nuclear Operations Related to Production of Radioisotope Power Systems," , *DOE/EIS-0373D* (2005).

[108] R. SANCHEZ, D. LOAIZA, R. KIMPLAND, D. HAYES, C. CAPPIELLO, and M. CHADWICK, "Criticality of a 237Np Sphere," *Nuclear Science and Engineering*, **158**, *1*, 1–14 (2008).

[109] C. G. BATHKE, B. B. EBBINGHAUS, B. A. COLLINS, B. W. SLEAFORD, K. R. HASE, M. ROBEL, R. K. WALLACE, K. S. BRADLEY, J. R. IRELAND, G. D. JARVINEN, M. W. JOHNSON, A. W. PRICHARD, and B. W. SMITH, "The Attractiveness of Materials in Advanced Nuclear Fuel Cycles for Various Proliferation and Theft Scenarios," *Nuclear Technology*, **179**, *1*, 5–30 (2012).

[110] W. SCHULZ and G. BENEDICT, "^{237}Np: PRODUCTION AND RECOVERY. AEC Critical Review Series." .

[111] ENEA, "Actinide and Fission Product Partitioning and Transmutation," *6th Information Exchange Meeting*.

[112] M. BASUNIA, "Nuclear Data Sheets for A = 237," *Nuclear Data Sheets*, **107**, *8*, 2323 – 2422 (2006).

[113] R. WEINMANN-SMITH, D. BEDDINGFIELD, A. ENQVIST, and M. SWINHOE, "Variations in AmLi source spectra and their estimation utilizing the 5 Ring Multiplicity Counter," *Nuclear Instruments and Methods in Physics Research Section A: Accelerators, Spectrometers, Detectors and Associated Equipment*, **856**, 17 – 25 (2017).

[114] N. ENSSLIN, W. H. GEIST, M. S. KRICK, and M. M. PICKRELL, *Passive Nondestructive Assay of Nuclear Materials Addendum, Chapter 7: Active Neutron Multiplicity Counting* (2007).

[115] W. H. GEIST, J. E. STEWART, H. O. MENLOVE, N. ENSSLIN, and C. SHONROCK, "Development of an Active Epithermal Neutron Multiplicity Counter (ENMC)," *Proceedings of the 41st Annual INMM Meeting*.

[116] J. E. STEWART, H. O. MENLOVE, D. R. MAYO, W. H. GEIST, L. A. CARRILLO, and G. D. HERRERA, "The Epithermal Neutron Multiplicity Counter Design and Performance Manual: More Rapid Plutonium and Uranium Inventory Verifications by Factors of 5-20," .

[117] S. CLARKE, E. MILLER, M. FLASKA, S. POZZI, R. OBERER, and L. CHIANG, "Verification and validation of the MCNPX-PoliMi code for simulations of neutron multiplicity counting systems," *Nuclear Instruments and Methods in Physics Research Section A: Accelerators, Spectrometers, Detectors and Associated Equipment*, **700**, 135 – 139 (2013).

[118] B. GODDARD, *Quantitative NDA Measurements of Advanced Reprocessing Product Materials Containing U, Np, Pu, and Am*, Ph.D. thesis, Texas A&M University (2013).

[119] H. O. MENLOVE and C. D. RAEL, "The Optimization and Calibration of the AWCC Using 252Cf Interrogation and the Comparison with an AmLi Neutron Source," .

[120] B. GODDARD, W. CHARLTON, and P. PEERANI, "Quantitative NDA Measurements of Multiactinide Oxide Fuels," *Nuclear Technology*, **186**, *3*, 403–414 (2014).

[121] A. D. FULVIO, T. SHIN, A. BASLEY, C. SWENSON, C. SOSA, S. CLARKE, J. SANDERS, S. WATSON, D. CHICHESTER, and S. POZZI, "Fast-neutron multiplicity counter for active measurements of uranium oxide certified material," *Nuclear Instruments and Methods in Physics Research Section A: Accelerators, Spectrometers, Detectors and Associated Equipment*, **907**, 248 – 257 (2018), Advances in Instrumentation and Experimental Methods (Special Issue in Honour of Kai Siegbahn).

[122] J. FANTIDIS, "Comparison of different geometric configurations and materials for neutron radiography purposes based on a 241Am/Be neutron source," *Journal of Taibah University for Science*, **11**, *6*, 1214 – 1220 (2017).

[123] S. CROFT, M. T. SWINHOE, and V. HENZL, "A priori precision estimation for neutron Triples counting," in "2011 2nd International Conference on Advancements in Nuclear Instrumentation, Measurement Methods and their Applications," (June 2011), pp. 1–7.

[124] E. C. MILLER, S. D. CLARKE, M. FLASKA, S. PRASAD, S. A. POZZI, and E. PADOVANI, "MCNPX-PoliMi Post-Processing Algorithm for Detector Response Simulations," .

[125] R. BAHRAN, T. CUTLER, and J. HUTCHINSON, "Neptunium Subcritical Observation (NeSO) Integral Benchmark Experiment Design," *Transactions of the American Nuclear Society Winter Meeting* (2017).

[126] A. MCSPADEN, T. CUTLER, R. BAHRAN, and J. HUTCHINSON, "Neptunium Sphere Subcritical Observation (NeSO) Final Experiment Design Update," *Transactions of the American Nuclear Society Winter Meeting* (2018).

[127] M. Y. HUA, B. GODDARD, C. LLOYD, E. C. LEPPINK, S. A. ABRAHAM, J. D. NOEY, S. D. CLARKE, and S. A. POZZI, "Simulation of the Nondestructive Assay of 237Np Using Active Neutron Multiplicity Counting," *Nuclear Science and Engineering*, **0**, *0*, 1–9 (2019).

[128] D. LOAIZA, R. SANCHEZ, D. HAYES, and C. CAPPIELLO, "Results and Analysis of the Spherical 237Np Critical Experiment Surrounded by Highly Enriched Uranium Hemispherical Shells," *Nuclear Science and Engineering*, **152**, *1*, 65–75 (2006).

[129] J. HUTCHINSON, R. BAHRAN, T. CUTLER, M. NELSON, T. GROVE, J. ARTHUR, G. MCKENZIE, W. MONANGE, and E. DUMONTEIL, "Validation of statistical uncertainties in subcritical benchmark measurements: Part II – Measured data," *Annals of Nuclear Energy*, **125**, 342 – 359 (2019).